

Seismic acquisition and analysis in a changing Arctic



Helene Meling Stemland

Thesis for the degree of Philosophiae Doctor (PhD)
University of Bergen, Norway
2020

UNIVERSITY OF BERGEN



Seismic acquisition and analysis in a changing Arctic

Helene Meling Stemland



Thesis for the degree of Philosophiae Doctor (PhD)
at the University of Bergen

Date of defense: 03.12.2020

© Copyright Helene Meling Stemland

The material in this publication is covered by the provisions of the Copyright Act.

Year: 2020

Title: Seismic acquisition and analysis in a changing Arctic

Name: Helene Meling Stemland

Print: Skipnes Kommunikasjon / University of Bergen

Preface

This dissertation for the degree of Philosophiae Doctor (PhD) has been submitted to the Department of Earth Science at the University of Bergen. The project was supported by ARCEX partners and the Research Council of Norway (grant number 228107). Additional funds for traveling were provided by NFiP, the CASE 2 consortium, and Equinor through Akademiaavtalen.

The candidate enrolled at the Department of Earth Science at the University of Bergen in October 2017, was admitted to the PhD program in March 2018, and submitted the thesis in July 2020. The work presented in this thesis was carried out in the Geophysics group (formerly Basin and Reservoir studies group) at the University of Bergen from October 2017 to July 2020, and during a research stay in the Rock Physics group (SRB Project) at Stanford University from April 2018 to December 2018. The research was supervised by Professor Tor Arne Johansen (University of Bergen), and co-supervised by Senior Engineer Bent Ole Ruud (University of Bergen) and Professor Leiv-J. Gelius (University of Oslo). During the research stay at Stanford University, Professor Gary Mavko hosted the candidate.

Acknowledgments

This PhD project would not have been the same without the support of a number of people. First of all, I would like to thank my supervisors for their support throughout these years. Thank you, Tor Arne, for encouraging me to start this PhD project, and for the many interesting discussions that sparked new research ideas. I also greatly appreciate that you have allowed me to go on so many trips, including the research stay at Stanford, scientific conferences in Norway and abroad, and numerous field trips to Svalbard. Thank you, Bent Ole, for being an invaluable resource when it comes to any technical or computational issue, and for always responding rapidly to any questions I may have had.

Thank you to Gary Mavko for including me in your research group at Stanford. The months at Stanford were a great experience where I learnt a lot about both geophysics and life in general. In this regard, I would also like to thank ARCEX and NFiP for financial support during the research stay.

Thank you to friends and colleagues at UiB, Stanford, ARCEX, and UNIS for interesting scientific discussions, fun lunch breaks, exciting field trips, and other social events. I also have to mention my fellow students from the Bachelor's and Master's programs in Geophysics at UiB. When I first arrived in Bergen nine years ago, I never imagined that I would end up staying here for this long and get some of my closest friends here.

Finally, I would like to thank my family for supporting me, and Håkon for always being there and believing in me, even during stressful times.

Helene Meling Stemland

Helene Meling Stemland

Bergen, 7th of July 2020

Abstract

In the Arctic, temperatures are regularly low enough that water exists in its frozen state, either in the form of ice, snow, or frozen ground. The effective elastic properties of a material depend on the elastic properties of the individual constituents and their geometrical distribution. Since solid ice is stiffer and more rigid than liquid water, effective elastic properties (bulk and shear modulus) increase with increasing degree of freezing; however, the properties strongly depend on the pore ice morphology, so the relationship is not linear. Seismic waves propagate with velocities that depend on the effective elastic properties of the medium they travel in. Hence, seismic waves travel faster in frozen materials than in similar unfrozen materials, and the velocity depth profile in near-surface Arctic rocks is often irregular. Due to this, seismic records from Arctic environments often show dominating and highly dispersive surface waves.

The Arctic surface is today warming at the most rapid pace on earth, but knowledge about the following consequences on the physical properties of the subsurface is scarce. How surface temperature is transmitted to depth and how this affects the mechanical properties of the subsurface is uncertain, in particular for areas with saline pore water. Since the stability of near-surface sediments is largely governed by their mechanical properties, understanding how these properties vary in a temporally changing Arctic is vital.

The overall objective of this study is to investigate how to safely acquire seismic data for mapping and monitoring of the near-surface sediments in a changing Arctic climate. To address this, we use seismic data acquired on Svalbard in the Norwegian Arctic. We first investigate whether seismic data can be acquired without affecting the vulnerable Arctic animal life (Paper 1), and then investigate how both long- and short-term surface temperature variations affect effective elastic properties (Paper 2) and the seismic wavefield (Paper 3 and Paper 4).

We find that seismic experiments of the size considered here are not physically injurious on the hearing of seals, largely due to the dominating low frequencies (<700 Hz) and the rapid decrease in sound level away from the source. Further, we find that effective

elastic properties and seismic P- and S-wave velocities of saline unconsolidated permafrost are highly sensitive to variation in ice saturation caused by varying surface temperatures. By using data from synthetic and real active and passive seismic experiments, we demonstrate various time-lapse effects caused by changing surface temperatures. In particular, the surface wave dispersion shows time-lapse effects of both the fundamental and higher-order modes of Rayleigh waves. We also show that rapidly changing surface temperatures correlate with strong transient events in passive seismic data, identified as frost quakes/cryoseisms. Hence, this study demonstrates that seismic may be useful in monitoring thawing effects in the near-surface sediments in the terrestrial Arctic due to climate perturbations. The thesis motivates for further studies on how to use seismic data in monitoring of permafrost degradation.

List of Publications

Paper 1: **Stemland, H. M.**, Johansen, T. A., Ruud, B. O., & Aniceto, A. S. (2019). Measured sound levels in ice-covered shallow water caused by seismic shooting on top of and below floating ice, reviewed for possible impacts on true seals. *First Break*, 37(1), 35-42. (Published).

Paper 2: **Stemland, H. M.**, Johansen, T. A., Ruud, B. O., & Mavko, G. (2020). Elastic properties as indicators of heat flux into cold near-surface Arctic sediments. *Geophysics*. (Accepted for publication).

Paper 3: **Stemland, H. M.**, Johansen, T. A., & Ruud, B. O. (2020). Potential Use of Time-Lapse Surface Seismics for Monitoring Thawing of the Terrestrial Arctic. *Applied Sciences*, 10(5), 1875. (Published).

Paper 4: Romeyn, R., Hanssen, A., Ruud, B. O., **Stemland, H. M.**, & Johansen, T. A. (2020). Passive seismic recording of cryoseisms in Adventdalen, Svalbard. *The Cryosphere*. (In review).

H. M. Stemland was the main author of Paper 1-3, and contributed to Paper 4 with seismic data acquisition, initial seismic data analysis, and review and editing of the manuscript.

Paper 1 is reprinted with permission from EAGE. All rights reserved. Paper 2 is reprinted with permission from SEG. All rights reserved. Paper 3 and Paper 4 are covered by the terms and conditions of Open Access license CC BY 4.0.

Contents

PREFACE	3
ACKNOWLEDGMENTS	5
ABSTRACT	7
LIST OF PUBLICATIONS	9
1. INTRODUCTION	13
1.1. The Arctic	14
<i>1.1.1. The cryosphere</i>	<i>14</i>
<i>1.1.2. Arctic climate change</i>	<i>17</i>
<i>1.1.3. Geophysical mapping and monitoring of the Arctic</i>	<i>19</i>
1.2. Elastic rock properties and the seismic method	20
<i>1.2.1. Effective elastic properties and rock physics modeling</i>	<i>21</i>
<i>1.2.2. Seismic waves</i>	<i>22</i>
<i>1.2.3. Seismic data analysis</i>	<i>24</i>
1.3. Seismic in the Arctic	26
<i>1.3.1. Impact of ice on elastic properties</i>	<i>26</i>
<i>1.3.2. The Arctic seismic wavefield</i>	<i>27</i>
<i>1.3.3. Arctic seismic data acquisition</i>	<i>29</i>
2. MAIN SCIENTIFIC CONTRIBUTIONS	33
Paper 1	35
Paper 2	45
Paper 3	113
Paper 4	133
3. SYNTHESIS	167
3.1 Main findings	167
3.2 Outlook	169
REFERENCES USED IN THE INTRODUCTION AND SYNTHESIS	175

1. Introduction

The overall objective of this study is to investigate how to safely acquire seismic data for mapping and monitoring of the near-surface sediments in a changing Arctic. In this context, the phrase “*a changing Arctic*” encompasses the temporal temperature changes that the Arctic region undergoes on various time scales, and the following consequences on the physical properties of the subsurface. It includes both day-to-day and season-to-season variations in surface temperature, and the long-term alterations in Arctic climatic conditions. We define two central sub-objectives to address this topic:

- To review the possible impacts of seismic experiments on Arctic animal life.
- To investigate how variations in Arctic surface temperature are reflected in seismic data, and further, if and how seismic data can be used to monitor changes in the degree of freezing in permafrost.

Studies of the Arctic are limited due to its remote location and the logistical issues related to doing research here. However, the area is becoming increasingly relevant to study as the environmental and economic importance of the region becomes evident:

- Environmentally because the Arctic climate is changing at the most rapid pace on earth (IPCC, 2014; Overland et al., 2014), while the actual consequences of a warming Arctic on the physical properties of the subsurface are uncertain.
- Economically because large reserves of hydrocarbons are likely located in the Arctic subsurface (Gautier et al., 2009).

In the papers that are part of this thesis, we make use of seismic data acquired on Svalbard in the Norwegian Arctic from 2013-2019. This includes data acquired both on sea ice in the inner parts of Van Mijen fjorden, and on frozen unconsolidated ground in Adventdalen. Following the classification of Kottke et al. (2006), Svalbard is traditionally considered a polar-tundra climate, meaning an area with low temperatures and minimal precipitation. Today, Svalbard experiences increasing temperatures and precipitation, and is therefore an interesting field site for studying Arctic climate change (NCCS, 2019). Svalbard is also interesting geologically because it is an uplifted part of the Barents Sea, and thus outcrops found here are analogous to potential hydrocarbon

reservoirs (Worsley, 2008). Compared with other parts of the high-Arctic, Svalbard is easily accessible due to infrastructure related to the coal mining industry.

This thesis is made up of an introductory chapter that describes some of the important concepts relevant for this study (Chapter 1), followed by the four research papers that make up the main part of this study (Chapter 2), and finally a chapter that summarizes the main findings, puts them into a common context, and discusses some potential future research directions (Chapter 3).

1.1. The Arctic

The Arctic is the northernmost region of the earth, located north of 66° 34' N. It comprises the vast Arctic Ocean and extensive land areas. Parts of the Arctic Ocean are covered by sea ice, and the terrestrial near-surface sediments are largely frozen (Christiansen et al., 2010). Its far northern location means that the Arctic is generally cold and with harsh weather conditions, but with large seasonal variations in temperature and sunlight. Despite the rough environment, about four million people are currently living in the Arctic (Heleniak and Bogoyavlenski, 2014). Since the stability of buildings and infrastructure built on frozen ground depends on the mechanical properties of the near-surface sediments, understanding how these properties change with time is crucial for engineering purposes (Hjort et al., 2018).

There is also a desire to map the deeper Arctic subsurface to understand where hydrocarbon resources are located. In 2008, the USGS estimated that approximately 13 percent of the world's undiscovered oil and 30 percent of the world's undiscovered natural gas are located in the Arctic (Gautier et al., 2009), and already today, about one third of the EU's natural gas imports are coming from Siberia (Sharples, 2016). Although renewable energy resources are becoming more common, the need for fossil fuels will probably be present for many years (IEA, 2019). Hence, there are clearly reasons to investigate both the shallow and deeper Arctic subsurface.

1.1.1. The cryosphere

A collective term for all components of the frozen earth is the **cryosphere**. Media in this part of the earth system have a frozen water constituent, which on land may be found in

the form of snow, continental ice sheets, glaciers, or permafrost, and in water may be found in the form of sea, river, or lake ice (French, 2017). Figure 1 from IPCC (2013) shows the distribution of various cryospheric media in the polar regions.

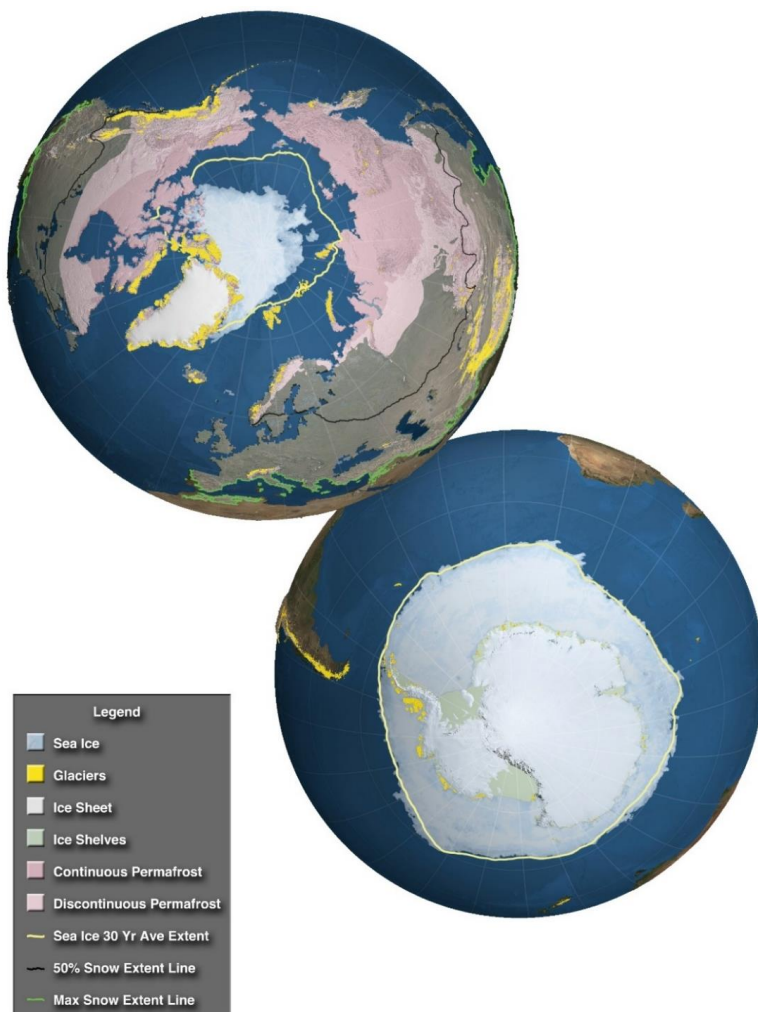


Figure 1: Distribution of cryospheric materials in the polar regions. The figure is Figure 4.1 from IPCC (2013), who report that “the source of the data for sea ice, permafrost, snow and ice sheet are data sets held at the National Snow and Ice Data Center (NSIDC), University of Colorado, on behalf of the North American Atlas, Instituto Nacional de Estadística, Geografía e Informática (Mexico), Natural Resources Canada, U.S. Geological Survey, Government of Canada, Canada Centre for Remote Sensing and The Atlas of Canada. Glacier locations were derived from the multiple data sets compiled in the Randolph Glacier Inventory (Arendt et al., 2012)”. Copyright IPCC 2013.

The temperature where liquid water starts to freeze is referred to as the freezing point, while the temperature where ice starts to melt is referred to as the thawing point (Potter et al., 1978). Since the physical properties of solid ice and liquid water are fundamentally different (e.g., density, strength, and viscosity), these temperatures are important thresholds when it comes to understanding the stability of the cryosphere. However, a medium is not necessarily fully frozen or fully unfrozen as an effect of saline pore water or surface effects, and the fraction of water that is frozen is referred to as the **ice saturation** (Potter et al., 1978; Dou et al., 2016; French et al., 2017). In this study, we consider some parts of the cryosphere in more detail.

In Paper 1, we consider seismic data acquired on sea ice over shallow water. **Sea ice** is floating ice that can vary in thickness from a few centimeters to several meters. It can build up over several years or form and melt annually, where fjord ice around Svalbard belongs to the latter category. The physical properties of sea ice depend on its age, salinity, and amount of brine trapped within the ice (Schwerdtfeger, 1963). In Papers 2, 3, and 4, we consider seismic data acquired on frozen ground, often referred to as permafrost. **Permafrost** is defined by French (2017) as “*perennially cryotic ground*”, meaning ground that remains at or below 0°C for at least two years. Permafrost typically consists of sediment grains, air, ice, and water, and its physical properties depend on the origin, burial history, and temperature of the sediments (French et al., 2017). It can be either consolidated or unconsolidated, where we focus on the latter type in this study. The purely thermal definition of permafrost implies that it can have a large range of physical properties depending on the degree of freezing of the pore water. The permafrost in Svalbard is laterally continuous and underlies around 90% of the land surface not covered by glaciers (Christiansen et al., 2010). The uppermost soil layer often thaws during summer and thus facilitates plant growth, before it freezes again in the winter. This annual cycle of thawing and freezing leads to trapped carbon within the permafrost (Schuur et al., 2015). Due to this, permafrost is estimated to contain twice as much carbon as is currently found in the atmosphere, and release of this carbon may have large consequences (Comyn-Platt et al., 2018).

1.1.2. Arctic climate change

In their most recent assessment report (AR5), The Intergovernmental Panel on Climate change (IPCC, 2014) present four scenarios of how the earth's climate may change in the 21st century. The various scenarios are referred to as **Representative Concentration Pathways (RCP)**, and are named based on the expected radiative forcing values in the year 2100 relative to pre-industrial levels. The radiative forcing is the difference between incoming and outgoing radiation, and thus, a positive value is a direct indicator that the earth is absorbing more energy than what it emits back to space. Due to the expected increase in atmospheric concentrations of greenhouse gases (carbon dioxide (CO₂), methane (CH₄), and nitrous oxide (N₂O)), land use, and air pollutants, all four scenarios project positive radiative forcing values in the year 2100. The corresponding mean global surface temperature increases by the end of the 21st century relative to the end of the 20th century are likely up to 1.7°C under RCP2.6, 2.6°C under RCP4.5, 3.1°C under RCP6.0, and 4.8°C under RCP8.5 (IPCC, 2014). The scenarios are just a few of numerous possible outcomes, but represent a likely range of climate projections.

Figure 2 is from AR5, and shows how average surface temperature and precipitation are expected to change for the most moderate scenario (RCP2.6) and for the most pessimistic scenario (RCP8.5). It shows that there are likely going to be large regional differences, and that Arctic temperatures and precipitation will increase more than the global mean (IPCC, 2014). The Arctic is currently warming at twice the global rate (IPCC, 2013), and this **Arctic amplification** is caused by positive feedbacks, meaning that changes in the radiative forcing value have consequences that induce further warming. Examples of such self-reinforcing processes are reduction in albedo due to melting of sea ice (Sereze and Francis, 2006), and release of CO₂ and CH₄ due to thawing of the carbon pools currently trapped in frozen ground (Schuur et al., 2015).

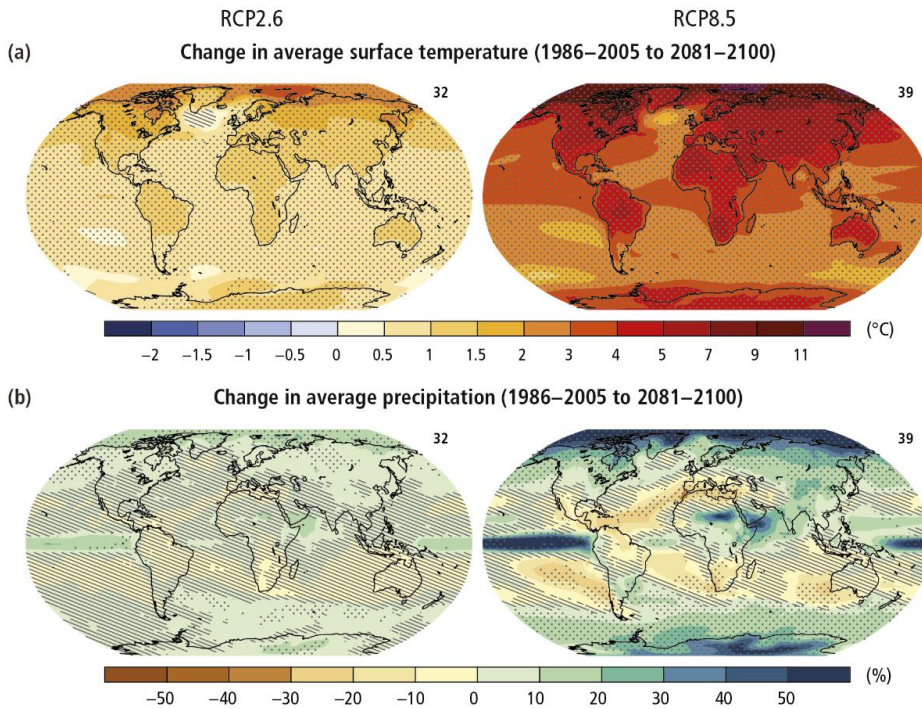


Figure 2: a) Change in average surface temperature and b) change in average precipitation based on multi-model mean projections for the end of the 21st century relative to the end of the 20th century under RCP2.6 (left) and RCP8.5 (right). Figure SPM.7 from IPCC (2014), copyright IPCC 2014.

Since all elements of the cryosphere have a frozen constituent that can change phase following natural temperature variations, the cryosphere is particularly vulnerable to climate change (Raynolds et al., 2014; Streletskiy et al., 2014). Hjort et al. (2018) estimate that by the year 2050 about three quarters of the current Arctic population will be affected by damage to infrastructure due to permafrost thaw, including damage to buildings, roads, runways and pipelines. The vegetation will likely change from a majority of tundra plants to far more flammable shrubs, associated with a higher wildfire risk (Tchebakova et al., 2009). Several studies and news reports show that already today, the Arctic is significantly affected by climate change. On Svalbard, several devastating avalanches and landslides have occurred in recent years due to unstable slopes caused by fluctuating temperatures and precipitation (NCCS, 2019; Fraser, 2019). Also in Canada, the frequency of landslides are dramatically increasing (Lewkowicz and Way, 2019), and in Greenland, the main airport Kangerlussuaq is likely going to close in just

a few years due to subsidence of its runways (Humpert, 2019). In Siberia, huge craters are forming (Murton et al., 2017; Hogenboom, 2017), and extensive forest fires all over the Arctic tundra have in recent years released great amounts of carbon to the atmosphere (Potter, 2018; Cormier, 2019; The Moscow Times, 2020).

Increased surface temperatures are affecting the stability of the Arctic near-surface sediments, but estimating the timing and actual magnitude of the consequences of a warming surface remains a challenge since the subsurface is complex (Zhang et al., 2008). Heat transfer within a medium depends on its thermal and physical properties, and can occur through conduction (heat transfer without the movement of mass), convection (heat transfer due to movement of mass), radiation, or through release or uptake of latent heat during phase change (Zhang et al., 2008). **Heat flux modeling** uses the physical and thermal properties as input to estimate how subsurface temperature varies temporally and spatially in the medium. However, it does not provide any information about how the physical properties of the subsurface are affected by the temperature variation, which are needed to assess the stability of the ground (Streletskiy et al., 2014). For this purpose, geophysical methods may be powerful tools.

1.1.3. Geophysical mapping and monitoring of the Arctic

Geophysical methods are useful for mapping and monitoring the physical properties of the subsurface. **Mapping** means to detect the spatial distribution of physical properties, and **monitoring** means to detect the temporal variation of these properties (Kneisel et al., 2008). It is advantageous to use surface geophysical methods because they are non-intrusive, which is especially important in the vulnerable Arctic (Trupp et al., 2009). While boreholes are useful for obtaining detailed knowledge about the subsurface physical properties at a specific site, a single well does not tell us anything about lateral variation in the area. Geophysical methods are on the other side often efficient in means of being able to cover large areas quickly (Kneisel et al., 2008).

The three groups of physical properties that have traditionally been the basis of geophysical Arctic near-surface investigations are electrical resistivity, dielectric permittivity, and seismic velocities (Kneisel et al., 2008). These properties are sensitive to degree of freezing in the subsurface; for example, electrical resistivity is much higher

for ice than for water, the dielectric constant is much higher for water than for ice, and seismic velocities increase as a medium freezes (Hauck and Kneisel, 2008). Previous studies have shown that geo-electrical, electromagnetic, and seismic methods are all somewhat useful for mapping and monitoring permafrost (see the review by Kneisel et al., 2008). However, both geo-electrical and electromagnetic methods struggle with accurately estimating ice saturation when the ground is only partly frozen at subzero temperatures (e.g. Ross et al., 2007; Briggs et al., 2016; Wu et al., 2017). In these cases, a large amount of unfrozen and highly conductive water may be present at subzero temperatures, making the correlation between resistivity and temperature complicated (Wu et al., 2017). Additionally, both geo-electrical and electromagnetic methods typically have limited penetration depth, and are thus only applicable for mapping the very uppermost sediments (Briggs et al., 2016). Seismic experiments can be tailored to illuminate the depth of interest, and can therefore be used to map both shallow and deep sediments (Kearey et al., 2002). Reflection and refraction seismic are commonly used in hydrocarbon exploration, and Hilbich (2010) shows that refraction seismic works well in alpine permafrost regions as well. However, seismic velocities need to increase consistently with depth to facilitate detection of refracted energy at the surface, which is often not the case in Arctic permafrost areas where salinity and ground-ice content vary with depth (Dou and Ajo-Franklin, 2014). The potential of using seismic surface wave methods to map these areas is a less studied topic, but is interesting because previous studies show the potential of using this method for characterizing near-surface sediments (see the overviews by Socco and Strobbia, 2004; Socco et al., 2010). The remaining part of this chapter introduces the principles of the seismic method and the special considerations that are required when seismic is used in Arctic environments.

1.2. Elastic rock properties and the seismic method

Elastic properties are mechanical properties describing the relation between applied stress on a material, and the resulting deformation of the material, called strain. The **bulk modulus K** describes the resistance of the material to change volume when being exposed to normal stress (incompressibility), and the **shear modulus μ** describes the resistance of the material to change shape when being exposed to shear stress (rigidity)

(Mavko et al., 2009). By using some kind of seismic method (active or passive), we can record seismic waves that propagate through the ground with velocities that depend on the elastic properties of the media that they travel in. The generated seismic wave consists of several frequency components, and the seismic source can be tailored to create a source signal that carries energy at specific frequencies: low frequencies can generally penetrate deeper into the earth than higher frequencies, but with a lower vertical and lateral resolution due to the longer wavelength (Kearey et al., 2002). Some of the relevant terminology and concepts are described in the following sections.

1.2.1. Effective elastic properties and rock physics modeling

The elastic moduli of a single material can be found through laboratory experiments (see Mavko et al. (2009) for an overview of experimentally derived elastic moduli). However, most media are composed of multiple constituents, both solids and liquids. When a seismic wave travels through a composite medium, the wave cannot distinguish features smaller than its wavelength. Thus, the wave travels with velocities that depend on the overall elastic properties of the composite, referred to as the **effective elastic properties**. These depend on the elastic properties, volume fraction, and geometrical distribution of the individual constituents of the medium (Mavko et al., 2009). The effective elastic properties and the related effective seismic properties are collectively referred to as the effective rock physics properties.

Rock physics describes the relationship between physical rock properties and effective elastic properties, and **rock physics modeling** is the approach used for linking these properties (Mavko et al., 2009). This may either be done through computing effective elastic properties from known physical properties (forward rock physics modeling), or by estimating physical properties from geophysical observations (inverse rock physics modeling) (Johansen et al., 2013; Bredesen et al., 2015). Many different rock physics models have been developed for different purposes. The simplest models are based on bounds that provide upper and lower limits for effective elastic moduli of a medium, but that do not take into account the structure of the rock (Reuss, 1929; Voigt, 1928; Hashin and Shtrikman, 1963). These are useful as a first approximation, but we often prefer more complex models that take into account both physical and structural properties. A

well-known rock physics model is the Hertz-Mindlin contact theory (Mindlin, 1949), which is valid for an idealized unconsolidated dry spherical grain packing. This model takes into account confining pressure and compaction, but not fluid content. To account for fluid effects, fluid substitution approaches must be implemented (Gassmann, 1951; Biot, 1956). For consolidated rocks, the Hertz-Mindlin model cannot be used because it requires a limited number of contact points between the grains. In this case, so-called inclusion models are commonly used (e.g., Berryman, 1980a, 1980b), which assume that all constituents of the medium are inclusions in a background-medium with initially unknown properties, and use the scattering to iteratively estimate the effective elastic properties of the medium. The details of the rock physics models used in this study are outlined in the appendices of Papers 2 and 3.

1.2.2. Seismic waves

Seismic waves are divided into body waves and surface waves. **Body waves** are either P- or S-waves and can travel deep into the subsurface. P-waves travel with a particle motion parallel to the propagation direction and can travel in both solids and liquids, while S-waves travel with a particle motion normal to the propagation direction and cannot travel in water due to the absence of shear strength in a liquid (Kearey et al., 2002). The P-wave travels as an acoustic wave in air, and is then referred to as the air wave. **Surface waves** are seismic waves traveling along surfaces between media with different physical properties, and they are rapidly attenuated with increasing distance from the surface (Kearey et al., 2002). Several types of surface waves exist at various interfaces (e.g., solid-fluid or solid-vacuum), and they are characterized by different particle motions. Examples are Rayleigh waves, Lamb waves, Love waves, Scholte waves, and Stoneley waves. In this study, we focus particularly on the Rayleigh wave, which travels with a retrograde particle motion in a solid medium along the surface between the solid and air (Landau et al., 2012).

The velocity of the envelope of a seismic wave with a finite bandwidth is called the **group velocity**, while the velocity of a specific frequency component of the wave is called the **phase velocity** (Mavko et al., 2009). In this study, we only consider elastically isotropic media (i.e., elastic properties are independent of direction), and the effective

elastic properties are related to seismic P- and S-wave velocities V_p and V_s in a homogenous medium through the equations

$$V_p = \sqrt{\left(K + \frac{4}{3}\mu\right) / \rho},$$

and

$$V_s = \sqrt{\mu / \rho},$$

where the effective density ρ is a weighted average of the densities of all constituents, and K and μ are the bulk and shear modulus, respectively. From the equations, it is evident that the P-wave will always travel faster than the S-wave in the same medium because it depends on both shear and bulk modulus ($\{K, \mu\} \geq 0$). For a Rayleigh wave traveling along the surface of a homogenous medium (halfspace), the seismic velocity c_R is related to the effective elastic properties through the equation (Landau et al., 2012)

$$\zeta^3 - 8\zeta^2 + 8\zeta(3 - 2\eta) - 16(1 - \eta) = 0,$$

where

$$\zeta = c_R^2 / V_s^2 \text{ and } \eta = V_s^2 / V_p^2.$$

Bergmann (1948) gives an approximate solution to this equation, valid for positive Poisson's ratios ν :

$$c_R / V_s = (0.87 + 1.12\nu) / (1 + \nu),$$

demonstrating that changes in the shear modulus will have a particularly large impact on the Rayleigh wave velocity (see also Malischewsky (2005)).

In nature, the subsurface is not homogenous, but the elastic properties rather vary with depth. This can be due to variation in mineralogy, porosity, fluid content, and pressure. For body waves, this results in reflection or refraction of energy at boundaries between media with different elastic properties; it is for example the large difference in elastic

properties between solids and liquids that makes seismic so effective for hydrocarbon exploration (Kearey et al., 2002). For surface waves, this can instead make the wave **dispersive**, meaning frequency-dependent phase velocity, i.e., group velocity \neq phase velocity (Mavko et al., 2009). Dispersion is also associated with other frequency-dependent rock properties, such as attenuation. Waves can be dispersive due to intrinsic dissipation (intrinsic dispersion), and/or due to layering of the medium that they travel in (geometric dispersion or apparent dispersion) (Liu et al., 1976), where the former is usually small compared to the latter. Rayleigh waves in elastic near-surface sediments with a varying velocity depth gradient are geometrically dispersive because high frequency amplitudes decrease more rapidly with depth than lower frequencies. Hence, as illustrated in Figure 3, sediments at both shallow and greater depths affect low frequencies, while only shallow sediments affect high frequencies. Thus, waves of different wavelength travel with different phase velocities, and the dispersion characteristics of surface waves carry information about the variation in elastic properties with depth (Socco et al., 2010).

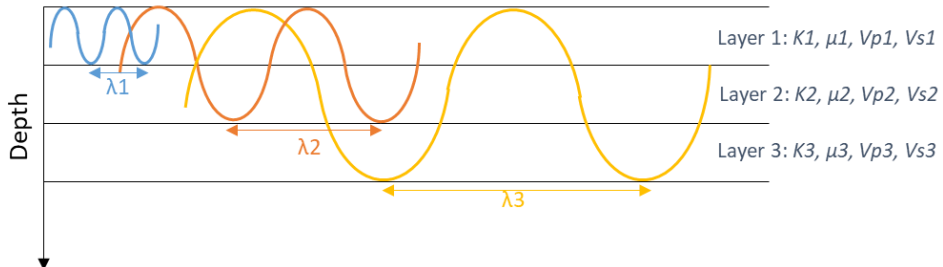


Figure 3: Low frequencies (long wavelengths λ_3) travel deeper than high frequencies (short wavelengths λ_1). If elastic properties vary with depth, the various frequency components travel with different phase velocities. If elastic properties increase with depth, the wave is normally dispersive, and if they decrease with depth, the wave is inversely dispersive.

1.2.3. Seismic data analysis

From the previous sections, it is clear that the seismic wave properties of both body and surface waves depend on the elastic properties of the media that they travel in, and thus indirectly carry information about these properties. However, careful **seismic analysis** is necessary to extract this information (Yilmaz, 2001). Seismic data can be analyzed

for seismic amplitudes, travel times, frequency content, and attenuation. The seismic amplitudes are proportional to either the pressure recorded at a hydrophone, or the particle velocity of a geophone (Kearey et al., 2002). From experience and knowledge about seismic properties of the various wave types, we can recognize specific events in seismic gathers, for example direct or refracted body waves as linear events, reflected body waves as hyperbolic events, or dispersive surface waves as fan-shaped events.

Depending on our purpose for studying the seismic data, we often want to enhance some wave events and suppress others. This can be achieved through **seismic processing**. The seismic processing scheme needs to be designed depending on how the seismic data were acquired, and what we are interested in studying in the data. As an example, the Rayleigh wave is usually considered to be noise in reflection seismic imaging, but may be useful for near-surface engineering purposes. Some typical processing steps are muting of unwanted events, deconvolution to remove the effect of the source signal, filtering to remove ambient or coherent noise and multiples, amplitude recovery to compensate for amplitude loss with depth, and stacking to enhance the signal-to-noise ratio. Further, it is useful to transform the recorded signal to the frequency domain using Fourier transformation, which allows us to study how energy is distributed with frequency (Yilmaz et al., 2001).

Another tool for analyzing seismic data is **seismic modeling**. The objective of seismic modeling is to simulate a seismic experiment, and it is therefore useful for linking effective rock physics properties with seismic observables. The aim can be to produce synthetic seismic data from known effective rock physics properties (forward modeling), or to obtain effective rock physics properties from seismic data (inverse modeling) (Krebes, 2004). **Seismic inversion** is carried out as an iterative process of minimizing the error between observed seismic data and synthetic seismic data generated through forward modeling of a given subsurface model (Cooke and Cant, 2010; Socco et al., 2010). The subsurface model that produces the minimum error between observed and modeled seismic data is assumed to be the correct model. We can compute the misfit in the time domain or in the frequency domain, and many different

methods for carrying out the inversion are possible, taking into account either certain parameters or the entire seismic wavefield, see Cooke and Cant (2010) for an overview.

1.3. Seismic in the Arctic

Even though the potential of using seismic for mapping the subsurface is well established, several special aspects need to be considered when seismic is used in the Arctic:

- Scientific challenges include how to account for temperature-dependent elastic properties, how to analyze data with dominant surface waves, and how to analyze data acquired in an area with irregular velocity gradients.
- Logistical challenges include how to acquire seismic data in harsh weather conditions in a safe way, and how to make sure we do not harm the vulnerable Arctic fauna and flora.

In the following sections, some of these aspects are described in more detail.

1.3.1. Impact of ice on elastic properties

When sediments freeze or thaw, the volume fractions of water and ice change, and therefore the effective elastic properties are affected. Since the elastic bulk and shear modulus of solid ice are higher than those of liquid water, the corresponding effective elastic properties and seismic velocities increase with increasing ice saturation (Zimmerman and King, 1986). This has been documented in several laboratory experiments (Timur, 1968; Dou et al., 2016).

In addition to ice saturation, the effective rock physics properties strongly depend on the geometrical distribution of ice in the pore space (Dou et al., 2017). Dvorkin et al. (1994, 1999) and Dvorkin and Nur (1996) describe how effective elastic properties vary with ice saturation for various microstructural distributions of pore ice in sediments. Figure 4 shows four possible scenarios for how ice can form at a pore scale: a) ice forms at the grain contacts where it cements the grains together. Therefore, even a small increase in ice saturation increases the effective stiffness and rigidity of the medium drastically. b) Ice forms in the pore-space without initially being in contact with the grains. Therefore,

increasing ice saturation does not significantly affect effective stiffness and rigidity until the ice saturation is high enough that the ice comes in contact with the grains. c) Ice forms part of the load-bearing frame. In this case, effective stiffness and rigidity slowly increase at low ice saturations, before rapidly increasing at high ice saturations. d) Ice coats and cements the sediment grains. Therefore, effective stiffness and rigidity rapidly increase even at low ice saturations, but slightly less than for the purely cementing model because some of the ice also forms away from the grain contacts.

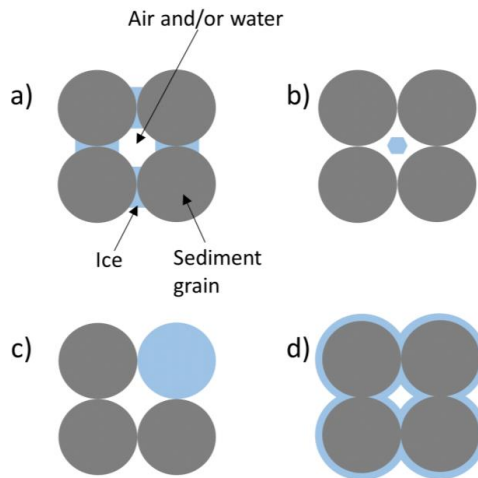


Figure 4: Various models of pore-scale distributions of ice: a) Cementing pore ice, b) Pore-filling ice, c) Frame-strengthening ice, d) Coating cementing ice.

Laboratory and field data show that observed seismic velocities do not fit with seismic velocities computed using either one of these models (Dou et al., 2016; Matsushima et al., 2016; Wu et al., 2017), which suggests that pore ice morphology in partly frozen sediments is complex. Thus, determining how pore ice morphology affects seismic data is one of the main challenges related to using seismic in the Arctic.

1.3.2. The Arctic seismic wavefield

Since cryospheric media generally have higher effective elastic properties than their sub-Arctic counterparts do, the uppermost layer in Arctic environments is typically stiffer than the layers below. This leads to seismic records that deviate from those we obtain in locations where the uppermost layer is softer than those below (Johansen et al., 2011).

Velocity reversals in the ground due to varying ice content or ice saturation with depth prevent recording of energy that is reflected or refracted from boundaries in the subsurface. Additionally, the stiff upper layer facilitates certain wave types, which is evident from seismic data acquired in Arctic environments that tend to show strong surface waves (Rendleman and Levin, 1990; Johansen et al., 2003; Tsuji et al., 2012; Johansen and Ruud, 2020). This includes Rayleigh waves in seismic data acquired on frozen ground and on glaciers, and Scholte waves in seismic data acquired on frozen ground and on glaciers, and flexural ice waves (asymmetrical Lamb waves) in seismic data acquired on floating ice over shallow water. In Figure 5, we show examples of seismic data acquired on floating sea ice and on frozen ground on Svalbard. The high-amplitude and dispersive surface waves make it a challenge to interpret seismic data for reflections and refractions from deeper sediments. However, their presence also makes it interesting to analyze the surface waves to see what they can tell us.

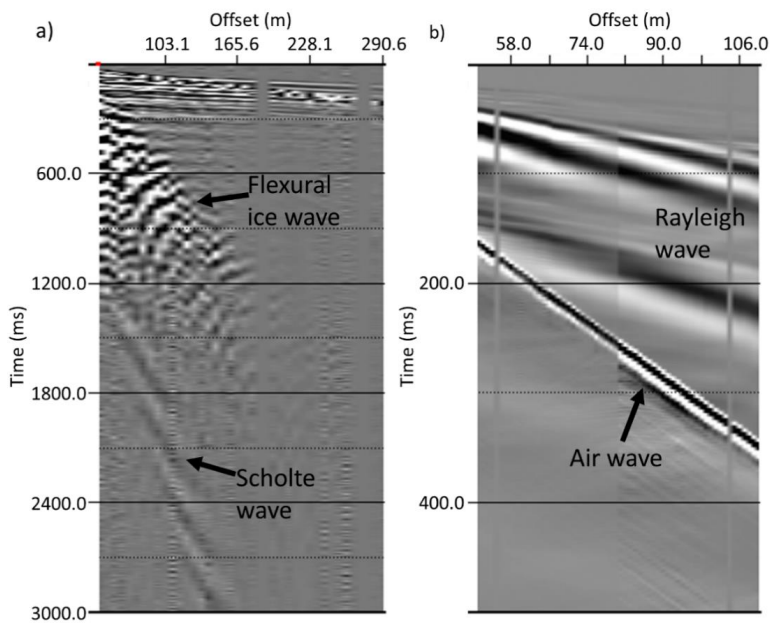


Figure 5: Seismic data acquired in Arctic environments tend to show strong surface waves. a) Seismic data acquired with an air gun at 1.5 m depth in water and vertical component geophone strings on floating sea ice (data used in Paper 1). b) Seismic data acquired with detonating cord on frozen ground and vertical component single geophones and geophone strings (data used in Paper 2). Note the different time scales in the two figures.

1.3.3. Arctic seismic data acquisition

Logistically, seismic experiments are difficult to carry out in the Arctic due to its remote location and harsh weather conditions (Trupp et al., 2009). Some of the equipment used at lower latitudes does not work in the Arctic, for example, marine streamers cannot be used on sea ice-covered ocean (Johansen et al., 2011). Additionally, battery life of seismic equipment is often short in very cold environments, and HSE concerns may stop or delay seismic operations. Hence, seismic experiments in the Arctic need to be meticulously planned, but also allow for rapid change of plans.

It is also important that the seismic data are acquired without affecting the Arctic animal life, which includes marine mammals, polar bears, foxes, reindeer, and migratory birds. Since seismic P-waves travel as acoustic waves in air and water, concerns have been raised about possible impacts of seismic on the hearing of animal life, in particular marine mammals (e.g., Gausland, 2000; Malakoff, 2002; Lavelle, 2010). Just like humans, marine mammals have a hearing that depends on both the intensity, frequency, and duration of the sounds they are exposed to (Gordon et al., 2003). **Sound pressure level (SPL)** is a decibel measure of how loud a sound is heard as, and is related to the wave pressure (0-to-peak) p_e through the equation (Southall et al., 2007)

$$SPL = 20 \log(p_e / p_0),$$

where p_0 is the reference pressure (1 μ Pa in water, 20 μ Pa in air). By instead using the sound exposure level (SEL), we can additionally take into account the number and duration of sounds.

Thresholds for sound levels that may lead to temporary and permanent hearing threshold shifts in marine mammals (TTS and PTS, respectively) have been determined by NMFS (2016). Additionally, the frequency-dependent hearing sensitivity of marine mammals means that they do not hear all frequencies equally well. Physical experiments have been used to determine **weighting functions** that can be used to assess how well they hear a sound based on the frequency content (Southall et al., 2007; Southall et al., 2019). Figure 6 shows estimated weighting functions for a variety of marine mammals, demonstrating that sound levels at frequencies the animals have a low sensitivity for are weighted down

up to 50 dB relative to sounds at the frequency the animals hear best. Since both pressure and frequency content of the seismic waves can be somewhat controlled through the choice of seismic source, the impact on the hearing of animals is relevant to consider when planning seismic experiments.

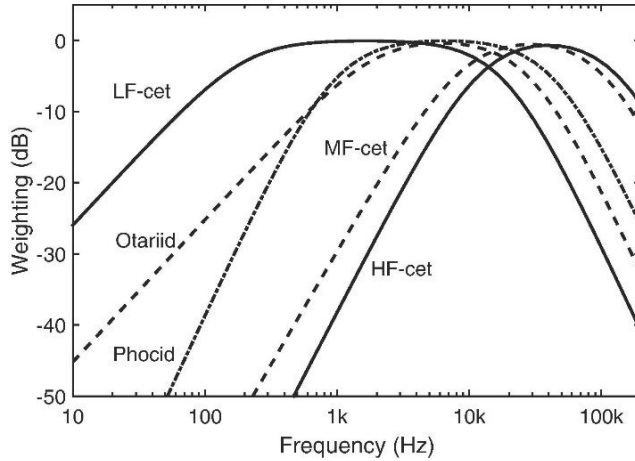


Figure 6: *Weighting curves for different functional hearing groups of cetaceans and seals: baleen whales (LF-cet), larger odontocetes and most dolphins (MF-cet), high-frequency specialists, including porpoises (HF-cet), true seals (Phocid), and sea lions and fur seals (Otariid). Figure from Tougaard and Beedhold (2019), published under Open Access License CC BY-NC-ND by Elsevier Ltd. Seismic experiments usually aim to generate low frequencies (<100 Hz), which most marine mammals have a low hearing sensitivity for.*

2. Main scientific contributions

In this chapter, the four papers that make up the main part of this doctoral thesis are reprinted. Papers 1 and 3 are reprinted in the journals' format, and therefore have deviating page numbers from the rest of this thesis. Further, since the papers are published or submitted to different scientific journals, the reference styles vary.

Paper 2

Accepted for publication in *Geophysics*.

Paper 2: **Stemland, H. M.**, Johansen, T. A., Ruud, B. O. & Mavko, G. (2020). Elastic properties as indicators of heat flux into cold near-surface Arctic sediments. *Geophysics*.

Final accepted version reprinted with permission from SEG.

Copyright: Society of Exploration Geophysicists 2020.

doi: <https://doi.org/10.1190/geo2019-0662.1>



III

ELASTIC PROPERTIES AS INDICATORS OF HEAT FLUX INTO COLD
NEAR-SURFACE ARCTIC SEDIMENTS

Helene Meling Stemland^{1,3}, helene.stemland@uib.no

Tor Arne Johansen^{1,2,3}, TorArne.Johansen@uib.no

Bent Ole Ruud^{1,3}, Bent.Ruud@uib.no

Gary Mavko⁴, mavko@stanford.edu

¹ University of Bergen, Department of Earth Science, PO Box 7803, 5020 Bergen, Norway.

² The University Centre in Svalbard (UNIS), PO Box 156, 9171 Longyearbyen, Norway.

³ ARCEX, UiT The Arctic University of Norway, PO Box 6050 Langnes, 9037 Tromsø, Norway.

⁴ Stanford University, Geophysics Department, 397 Panama Mall Mitchell Building, Stanford, CA 94305-2215.

Running head: Elastic properties of Arctic sediments

Original paper date of submission: **8 October 2019.**

ABSTRACT

Temperatures in the terrestrial Arctic are today increasing at the highest rate on Earth, and heat flux into the cold sediments may result in extensive thawing. Thawing sediments lose their mechanical strength, and warming therefore has significant geomorphic consequences. We have combined heat flux, rock physics, and seismic modeling to estimate the change in elastic properties related to various published future climate scenarios in the Arctic, and thus investigate the feasibility of exposing thawing rates from seismic data. The heat-flux model was validated using temperature data continuously recorded at the surface and within a well in Adventdalen, Svalbard. We estimated the evolving temperatures in an upper vertical section of the well using the heat-flux model, and compared with actual measured well temperatures. The modeled and measured data were consistent, even though our simplified model ignores heat transport due to fluid flow and the effects of clay. The heat flux modeling resulted in subsurface isotherms that were input to rock physics modeling based on two-end-member mixing of fully frozen and unfrozen composites to delineate possible climate effects on the seismic properties of the sediments. The results show that elastic and seismic properties of (partly) frozen unconsolidated near-surface saline sediments strongly depend on heat flux into the subsurface, and vary both seasonally and between different climate scenarios. Seismic data obtained by full waveform modeling and real experiments in Adventdalen show that time-lapse analysis of Rayleigh waves may be an efficient tool for monitoring heat flux into the terrestrial Arctic.

INTRODUCTION

The terrestrial Arctic is mainly covered by continuous or discontinuous permafrost, defined as perennially cryotic ground. This purely thermal definition implies that permafrost is not necessarily frozen, as salinity, absence of moisture, or surface effects can prevent freezing to temperatures well below 0°C (French, 2017). Permafrost is believed to hold twice as much carbon as is currently present in the atmosphere, and also acts as a seal for other climate gases trapped beneath, including gas hydrates. Thus, a potential thawing of frozen permafrost caused by warmer climate may lead to emissions of strong greenhouse gases like carbon dioxide and methane, imposing further warming (IPCC, 2014; Schuur et al., 2015; Comyn-Platt et al., 2018). Hence, understanding the impact of thawing on the climate models used for projecting future climate change is crucial, and can be enhanced by the use of geophysical methods for mapping and monitoring frozen ground areas.

The fifth assessment report (AR5) from the Intergovernmental Panel on Climate Change (IPCC, 2014) suggests global mean temperature increases of 0.3 – 4.8°C from the end of the 20th century to the end of the 21st century. In AR5, the IPCC (2014) also state that it is very likely that temperatures in the Arctic will increase more than the global mean due to so-called Arctic amplification, with the highest impact onshore. According to Schoolmeester et al. (2019), Svalbard in the Norwegian Arctic will experience among the most dramatic temperature increases in the Arctic. Seneviratne et al. (2016) estimate regional temperature changes in Svalbard up to five times larger than the minimum annual global change. However, Overland et al. (2014) highlight that there will be large seasonal differences, with the largest increase occurring during the winter. Following the predicted changes in Arctic climate, the IPCC (2014) estimate that the area with permafrost in the upper 3.5 m will decrease by 37 – 81% by the year 2100, but consider the exact physical thawing rates a main source of uncertainty.

Electrical resistivity, dielectric permittivity, and seismic velocities are useful geophysical properties to distinguish between unfrozen and frozen ground (Kneisel et al., 2008), and techniques sensitive to these properties have been tested for mapping Arctic near-surface sediments (Briggs et al., 2016; Wu et al., 2017; Keating et al., 2018). These methods all detect changes in the thermal state of permafrost, but show various degree of success in accurately estimating ice content in the sediment, specifically when the ground is only partly frozen. For example, the correlation between resistivity and temperature is complicated when unfrozen water is present at subzero temperatures (Wu et al., 2017), limiting the use of geoelectrical and electromagnetic methods. Limited penetration depth is also a problem for many geophysical techniques, but seismic experiments can be tailored to investigate various depths (Kneisel et al., 2008). However, conventional reflection and refraction seismic methods are inadequate if the velocity gradient is irregular like in the case of varying degree of freezing with depth (Dou and Ajo-Franklin, 2014). Only a few studies have been devoted to the application of seismic surface waves for investigating or monitoring terrestrial Arctic environments (Tsuji et al., 2012; Dou and Ajo-Franklin, 2014).

A number of laboratory experiments show that elastic and seismic parameters of partially or fully water-saturated unconsolidated sediments increase substantially when pore fluid freezes, since frozen ground is stiffer and less deformable than unfrozen ground (Zimmerman and King, 1986; Dou et al., 2016; Matsushima et al., 2016; Wu et al., 2017). Hence, thawing of currently frozen ground can have large geomorphic consequences, particularly in areas with high ground-ice content (Nelson et al., 2001; Hjort et al., 2018). In turn, large volume of ice thawing may lead to subsidence, with significant risks for building and infrastructure damage due to loss of shear strength. In this regard, the strong dependence of freezing conditions on elastic properties enables detection of thawing using seismic methods. However, to what degree the elastic properties of near-surface sediments will change following

future climate change as projected by the IPCC (2014) and how this will appear in seismic data is uncertain. A robust correlation between surface temperature and elastic properties has to be conducted as a first step to integrate seismic data, permafrost degradation, and global climate models.

The objectives of this paper are to combine heat flux, rock physics, and seismic modeling to estimate the changes in elastic properties associated with various published future climate change scenarios for the Arctic, and thus investigate the feasibility of using seismic data to expose thawing in unconsolidated sediments. We first evaluate the role of various parameters such as salinity, pore fluid saturation, and moisture content on heat transport in unconsolidated sediments. By perturbing some of the above parameters, considering a simple horizontally layered saline sediment model defined from well data onshore Svalbard, we model heat flux into the sediments using recent top ground temperature history data, but also inferring top ground temperature increases as discussed in AR5 (IPCC, 2014). We then review a procedure for how to model the seismic properties of freezing or thawing sediments, and apply this workflow to finally estimate the perturbing elastic properties and surface-wave characteristics based on the previous heat-flux modeling results.

HEAT TRANSPORT IN COLD SEDIMENTS

Transport of heat occurs through convection and conduction, and depending on the material, either of these two processes may be dominant. In addition, latent heat is absorbed or released to alter the material's molecular structure when a material changes phase. Conduction is commonly assumed as the dominant heat transfer mechanism in permafrost (Romanovsky and Osterkamp, 2000), although some studies suggest that convection can contribute to a significant amount of thawing during the spring (Kane et al., 2001; Veuille et al., 2015). Weismüller et al. (2011) model heat transport in permafrost at a site on Svalbard, and compare with field data. They found that convective transport by liquid water and water vapor only carried minor amounts of the total heat flux throughout the year. Therefore, we here assume that including only conduction is justified because we do not attempt to compute exact thawing rates at a specific day or time of the year, but rather estimate the general degree of thawing. Hence, our estimates of thawing are to some extent more conservative during periods of extensive thawing, when the contribution of convective mechanisms is slightly more significant. This assumption reduces the computational complexity of the problem, as for convection a fully coupled soil water model is required (Zhang et al., 2008). Figure 1 illustrates some important concepts related to heat transport in permafrost. The amount of surface heat transmitted to depth depends on the temperature at the ground surface and the near-surface thermal properties.

Modeling heat flux into cold sediments

By limiting our study to the case of conduction only, we start with the 1D enthalpy equation (Govaerts et al., 2016)

$$C \frac{\partial T}{\partial t} + \nabla \cdot (-\kappa \nabla T) = Q. \quad (1)$$

Here, C ($\text{Jkg}^{-1}\text{K}^{-1}$) is volumetric specific heat capacity (hereafter referred to as heat capacity), T ($^{\circ}\text{C}$) is temperature at depth z (m), t is time, κ ($\text{Wm}^{-1}\text{K}^{-1}$) is thermal conductivity, and Q (Wm^{-2}) is external heat flux (e.g., geothermal heat flux). To find the relevant properties of a material made up of several constituents, we follow a similar approach as Govaerts et al. (2016), Mottaghy and Rath (2006), and Kitover et al. (2013). This implies replacing C and κ with their so-called equivalent properties C_{eq} and κ_{eq} , based on a weighting of the thermal properties of the various constituents. Latent heat L (J/kg) is included in the equivalent heat capacity to avoid a separate treatment of this effect, following Zhang et al. (2008) and Weismüller et al. (2011). The equivalent properties include a smoothed Heaviside function, defined by Φ , changing from zero to one for fully frozen to fully unfrozen material over a temperature interval dt that depends on the salinity, due to water changing phase in this temperature interval. We here modify the expression for equivalent heat capacity C_{eq} from Govaerts et al. (2016) to include a volume fraction of air in the pore space. For a medium consisting of matrix, air, fluid, and ice ($n=\{m, a, f, i\}$, respectively), we have

$$C_{eq} = \theta_m \rho_m c_m + \theta_a \rho_a c_a + \theta_f \rho_f \left(c_f + \frac{\partial \Phi}{\partial T} L \right) + \theta_i \rho_i \left(c_i + \frac{\partial \Phi}{\partial T} L \right). \quad (2)$$

Here, c_n , ρ_n , and θ_n are heat capacity, density, and volume fraction of the various constituents; see Table 1 for typical values. The total porosity is thus $\theta = \theta_a + \theta_f + \theta_i$, and by defining $\theta_f = (\theta - \theta_a) \Phi$, and $\theta_i = \theta - \theta_a - \theta_f$, phase change is included in equation 2. Density is assumed constant with temperature. Note the difference between the two expressions ice saturation and saturation; the former meaning the ratio of ice to total water and ice content, and the latter meaning the ratio of total water and ice content to total pore space.

Govaerts et al. (2016) use a square root mean to compute equivalent thermal conductivity κ_{eq} , but based on discussions in Zhang et al. (2008) and Weismüller et al. (2011),

we choose to use De Vries (1963) parameterization instead, which from Weismüller et al. (2011) reads

$$\kappa_{eq} = \frac{f_m \theta_m \kappa_m + f_a \theta_a \kappa_a + f_f \theta_f \kappa_f + f_i \theta_i \kappa_i}{\theta_m f_m + \theta_a f_a + \theta_f f_f + \theta_i f_i}, \quad (3)$$

where κ_n are the thermal conductivities of the various constituents with subscripts as defined above. The shape factors f_n of the various constituents assuming a continuous soil matrix with independent spherical particles are estimated by Weismüller et al. (2011) as

$$f_n = [1 + \frac{1}{3} (\frac{\kappa_n}{\kappa_0} - 1)]^{-1}, \quad (4)$$

where κ_0 denotes the thermal conductivity of the background medium (here $\kappa_0 = \kappa_m$).

The pore water salinity conditions the fraction of ice at a given temperature. Figure 2 shows that increasing the salinity leads to freezing point (i.e., starting temperature for ice formation) depression and gradual phase change down to the eutectic point (-21.3°C), which is caused by progressive salination of the residual pore water during temperature decrease (Potter et al., 1978; Dou et al., 2016). For simplification of the heat-flux modeling procedure, we here use the smoothed Heaviside function to represent the phase change.

We conducted a sensitivity analysis (Appendix A) of the various parameters in the model and found that salinity, saturation, and moisture content have the following effects on latent heat release/absorption, heat capacity, and thermal conductivity. First, increasing the salinity spreads out latent heat release/absorption over a larger temperature interval, and increases heat capacity and reduces thermal conductivity at a lower temperature. Second, increasing the saturation increases both the heat capacity (most in the unfrozen state) and the thermal conductivity (most in the frozen state). Third, increasing volumetric ice content causes higher latent heat release/absorption, while it reduces the heat capacity in the frozen state, and

increases it in the unfrozen state. Further, it reduces thermal conductivity severely in the unfrozen state, and slightly in the frozen state.

Test of heat flux model

To test the validity of the heat flux model implied by equations 1–3, we use borehole and temperature data acquired in a well in the high-Arctic fjord-valley Adventdalen on Svalbard (Figure 3). Details of the study area and data acquisition can be found in TSP Norway (2013), Gilbert et al. (2018), and Bratlie (2018). We consider a simplified model of the upper 20.0 m of sediments in the well, with physical properties derived from well log data. The sediments are unconsolidated, and the sediment layering including composition, porosity, and pore fluid properties are given in Table 2. Our first numerical experiment models the temperature development within this sequence of sediments, enforced by the varying top ground temperature data monitored in the well during a one-year cycle in 2012/2013.

According to Gilbert et al. (2018), lateral lithological variations are gentle in this area, justifying the use of data from only one well to construct the model. We furthermore simplify the lithological composition of the sediments by neglecting the presence of clay, since its complicating effect on heat transport is not considered in our model. In the study area, the upper sediments are eolian which freeze and absorb heat in a different way than the marine sediments below, and we therefore assume that salinity varies with depth. As a lower boundary condition, we use the data of Christiansen et al. (2010) and Biskaborn et al. (2019) to constrain a constant temperature of -5.5°C at 20.0 m depth and below.

For modeling heat flux, equation 1 was formulated in a finite-element scheme as provided by COMSOL (Pryor, 2009), where the equivalent heat capacities and thermal conductivities are determined from equations 2 and 3, and therefore vary with time and depth as the temperature distribution evolves with time. The modeling was initiated from the

measured borehole temperatures on the 10th of August 2012. Figure 4 shows modeled and measured temperatures in well AS-B-2 for every third month of the considered year. The model predictions are overall consistent with observations except during early winter (December), indicating that the model predicts a slightly more rapid change in subsurface temperatures than observed. This can be due to neglecting the effects of clay when modeling the equivalent parameters for heat transport, or inaccurate model parameters such as thermal properties, saturation, or moisture content. Furthermore, any effect of convection caused by circulating water is not considered, including refreezing of unfrozen water displaced by capillary forces. However, the model predictions seem to be in the range of observations, and our heat-flux model can thus be used to link effects of surface temperature variation to thawing and freezing of near-surface sediments in Arctic regions.

Possible thawing effects of a warmer climate

Our next modeling experiments emphasize the combined effects of varying pore fluid conditions and surface temperatures. In AR5, the IPCC (2014) present four scenarios of possible future temperature projections based on various initiated mitigation efforts, referred to as representative concentration pathways (RCP's). In the following, we simulate the thawing effects due to three top ground temperature scenarios associated with these RCP's in the year 2100. This includes the situation of today (T1, Figure 5a), and the predicted monthly average temperature increases of 2 – 8°C (T2) and 5 –14°C (T3), corresponding to RCP4.5 (“mitigation scenario”) and RCP8.5 (“business-as-usual scenario”), respectively. These projections are based on the experiments of Overland et al. (2014), and by assuming that top ground temperature increase will be similar to air temperature increase. Although future temperature fluctuations are most probably to change in both amplitude and frequency, we consider typical annual cycles of the temperature for T2 and T3 by adding the monthly average temperature to the data describing T1, as displayed in Figure 5b.

Further, various models for the salinity of the pore water (S1 and S2), saturation ($w1 - w5$), and ground moisture content ($m1 - m4$) are imposed, while the sediment properties are given in Table 2. We include the latter scenario because Gilbert et al. (2018) identify a pure ice layer at this depth through the study of several cores from Adventdalen; thus, knowledge about the impact of ground ice on heat flux is relevant. Table 3 defines the values of the various model parameters. In Figure 6, we present the modeled thawing depth (i.e., depth where ice formation starts) for the various scenarios.

Figure 6a shows that T1, T2, and T3 all lead to thawing of near-surface sediments, though to different extents. For T1 and T2, the thawing depth stays relatively constant from year to year, and the summer thawing is reversed during winter, while the most dramatic thawing is for T3, where thawing depth increases for every year. Figure 6b shows that heat conducts to greater depths for non-saline sediments S2 than for saline sediments S1. Less energy is required to increase the temperature of non-saline than saline permafrost at subzero temperatures, because phase change is involved in the latter, but not in the former. Further, as indicated by the sensitivity analysis (Appendix A), equivalent heat capacity starts to increase and thermal conductivity starts to decrease at a lower temperature for saline permafrost than for non-saline permafrost. Thus, changing the salinity affects both the heat transport into the ground and the freezing point of the pore water, and hence, the thawing depth. Figure 6c reveals more thawing for lower saturations, which is consistent with the sensitivity analysis that showed that latent heat, heat capacity, and thermal conductivity all increase for increasing saturation. Thus, lower saturation leads to increased thawing depth because air leads heat to depth easier than water or ice, and because less material is involved in the phase change process at lower saturations. Finally, Figure 6d indicates that less thawing occurs for permafrost with higher ground ice content, which is consistent with studies by Harris et al. (2009) and Etzelmüller et

al. (2011). This is because a larger volume of ice takes a longer time to melt due to the higher latent heat uptake required to complete the process.

CALCULATING THE ELASTIC RESPONSE OF FREEZING/THAWING SEDIMENTS

To investigate the impacts of future thawing on seismic properties as implicated by the results of the previous sections, we evaluate the effects of altered temperature and ice saturation distributions on the elastic properties through rock physics modeling. Numerous authors, including Zimmerman and King (1986), Dvorkin et al. (1994, 1999), Minshull et al. (1994), Ecker et al. (1998), Carcione and Seriani (1998), Johansen et al. (2003), and Dou et al. (2017) discuss the effects of freezing pore water on elastic properties of rocks. For unconsolidated sediments, freezing can cause the seismic velocities to increase extensively, as documented by Timur (1968), King et al. (1988), and Dou et al. (2016). Note that for consolidated sediments, the impact of freezing on the elastic parameters is not found to be as strong (Matsushima et al., 2016), and thus our approach is only valid for unconsolidated sediments. For rock physics modeling, we describe the freezing effects on the bulk modulus K and shear modulus μ .

Figure 7 illustrates our workflow for modeling elastic properties of unconsolidated sands for various freezing and fluid saturation scenarios discussed in the previous sections. The schematics define the rock physics modeling of two elastic members: A is representing sand in unfrozen state, and B is representing sand in frozen state. Member A is either a (1) dry, (2) fully water-saturated, or (3) patchy water-saturated sand, while member B is either a (4) fully or (5) patchy ice-saturated sand. The rock physics modeling strategies used for computing the elastic parameters of sand in state (1) – (5) are listed in Table 4; for completeness, the details of the modeling procedures are fully reviewed in Appendix B. Further, we apply the same approach as Dou et al. (2017), and use the Hashin-Shtrikman (HS) bounds (Hashin and Shtrikman, 1963) to describe the transition from unfrozen (A) to frozen state (B), or vice versa. The microstructural interpretation of the lower bound (HS⁻) is that it applies to simulate a situation where the frozen pore water in sand occurs in local domains, which means that the pore ice

remains disconnected, except when it is fully saturated and completely frozen. Correspondingly, the upper bound (HS⁺) describes a situation where the ice gradually forms as a connected aggregate within the sand. If the freezing of pore water occurs both ways, we use the average of the two bounds, which is similar to the Hill average (Hill, 1963; Mavko et al., 2009). Dou et al. (2016, 2017) show that the Hill average of the HS bounds coincides most with the elastic bulk modulus measured during controlled freeze-thaw experiments, and also compared with models assuming a single type of ice distribution (Dvorkin et al., 1994, 1999; Dvorkin and Nur, 1996). We therefore use the Hill average HS bounds in our modeling.

The computed effective elastic properties are related to P-wave (V_p) and S-wave (V_s) velocities in case of elastic isotropy by

$$V_p = \left(\frac{K+4\mu/3}{\rho} \right)^{\frac{1}{2}}, \quad (5)$$

and

$$V_s = \left(\frac{\mu}{\rho} \right)^{\frac{1}{2}}. \quad (6)$$

Here, ρ denotes the density, given by

$$\rho = (1 - \varphi)\rho_s + \varphi(S_w\rho_w + S_i\rho_i + S_a\rho_a), \quad (7)$$

where φ is sediment porosity and ρ_s is sediment density. Furthermore, S_j and ρ_j are saturation and density of water, ice, and air ($j=w, i, a$), respectively.

Figure 8 shows the modeled effective elastic and seismic parameters for unconsolidated sand at 10.0 m depth when the sediment is either fully or partially saturated, and transitioning from unfrozen to frozen. Effective elastic moduli and seismic velocities are higher for fully than for partly saturated pores (except S-wave velocity at 0% ice saturation) due to the significantly

higher elastic moduli of ice than air. The shear modulus is here seen to be particularly sensitive to the freezing condition (Figure 8b).

ELASTIC RESPONSE OF COLD SEDIMENTS TO VARIOUS CLIMATE MODELS

We now combine heat flux modeling of the various climate models T1 – T3 with rock physics modeling of typical near-surface sediments at Svalbard as defined by Table 2, and assuming a fully saturated medium. The rock physics modeling workflow of Figure 7 is implemented based on the isotherms of Figure 6a, which indicate the spatial and temporal temperature distribution within the near-surface sediments. Further, the relations of Potter et al. (1978) plotted in Figure 2 provide a direct estimate of ice saturation distribution with depth and time.

Figure 9 shows modeled temperatures and velocities at 1.0 m and 3.0 m depth through the fourth year of the heat-flux modeling plotted in Figure 6a, for models T1, T2, and T3. We note that even at subzero temperatures, there are major variations in the seismic velocities with time due to the gradual phase change caused by saline pore water. Variations are greater at 1.0 m depth than at 3.0 m depth, which is due to less heat being conducted down to the deeper sediments. For T1, temperatures at both 1.0 m and 3.0 m depth remain subzero most of the year, while for T3, temperatures exceed 0°C for large parts of the year. This corresponds to high seismic velocities for T1, and much lower velocities for T3, which indicates that a warming climate will have a significant impact on the seismic velocities of the shallow unconsolidated sediments. We also observe that due to the time lag of the heat flux, the coldest day at 1.0 m depth is not the coldest day at 3.0 m depth. This is in accordance with Isaksen et al. (2007), who observed a time lag of about 1.5 months in maximum and minimum temperatures between 0.0-3.0 m depth at a site close to the well indicated in Figure 3.

In addition to evaluating how the near-surface seismic model perturbs throughout a year for each climate model, we also study how seismic velocity profiles with depth vary between winter and summer for each climate model. Figure 10 shows seismic velocity profiles for the

coldest and the warmest day at 1.0 m depth in Figure 9a. The velocity profiles differ extensively between winter (Figures 10a-10c) and summer (Figures 10d-10f). Temperatures in the uppermost sediments are strongly affected by the top ground temperature, so that higher top ground temperature corresponds to warmer upper sediments and lower seismic velocities. Thus, Figure 10 illustrates the softening of the uppermost sediments associated with a warmer climate. Temperatures at depths larger than 10.0 m are fairly constant, but can possibly also be affected by heat flux if temperatures continue to increase. A sharp decrease in velocity around 3.0 m depth is visible in all velocity profiles, which coincides with the depth of transition from eolian to raised marine deposits, and correspondingly, a transition from low to high salinity. An interesting feature is seen in the winter velocity profiles for models T2 and T3, showing that this sharp velocity decrease may disappear with a future warmer climate where winter temperatures are high enough that summer thawing is not completely reversed during winter. A similar tendency is seen during summer, where the thickness of the layer that thaws completely during summer increases from T1 to T3, indicating that if warming continues, the high velocity layer in the eolian sediments may completely disappear during summer.

USING SURFACE SEISMIC DATA TO DETECT THAWING IN COLD SEDIMENTS

Since freezing conditions strongly influence on the shear modulus as seen in Figure 8, this implicates that surface waves should be sensitive to changing surface temperature. Surface waves of Rayleigh type propagate along a surface with a retrograde particle motion having an amplitude decreasing exponentially with increasing depth from the surface. The phase velocity of a Rayleigh wave depends on the elastic properties of the surface layer, but mostly on its shear modulus (Xia et al., 1999). A variation in the elastic properties of the near-surface layers means altered surface-wave signatures, and thus, as elastic properties vary with time and depth, this will cause time-lapse effects in the surface seismic data.

Both Figures 9 and 10 show that seismic velocities respond significantly to thawing associated with future climate change. The difference between the various models also show that thawing has an impact on the general shape of the near-surface velocity profile (e.g., steadily/irregularly increasing/decreasing with depth). Hence, Rayleigh waves can potentially be used to monitor effects of surface temperature alterations on the freezing conditions of near-surface sediments. To further scrutinize this, six seismic models constructed from the velocity profiles in Figure 10 were input to seismic modeling based on a full wavenumber integration method denoted OASES (Schmidt and Jensen, 1985). Figure 11 shows the corresponding modeled seismograms. There are significant differences between the various gathers, but the largest temperature time-lapse effects are revealed by the data representing summer conditions. For the data representing winter, the fundamental mode of the Rayleigh wave is distinct. The slope of this event becomes increasingly steeper from T1 to T3, which is related to the velocity decrease due to extended thawing. The gathers associated with summer are more complex. Also here, the velocity of the fundamental mode is decreasing from T1 to T3, but higher-order wave modes now become more extensive which makes the wavefield more complicated to interpret.

Figure 12 shows seismic data acquired from two repeated seismic experiments in Adventdalen at two different seasons: in May, before summer thawing commenced, and in September, when the surface temperature had been above 0°C for a longer time period. The data display seasonal time-lapse effects; however, a direct comparison with the synthetic seismic data is impossible since the exact mineralogy, salinity, and saturation at the study site is unknown. In particular, the data displayed here were collected in an area of Adventdalen with high and laterally heterogeneous moisture content, which our previous results have demonstrated can significantly affect the data. Nevertheless, both examples demonstrate that surface seismic data may be a suitable tool for monitoring heat flux into areas that today are subjected to permafrost.

DISCUSSION

This study aims towards developing an integrated workflow for understanding how the warming of the terrestrial Arctic can be monitored using time-lapse surface seismic data. Subsurface isotherms are constructed from heat flux modeling, which are converted to ice saturation distribution using the equations of Potter et al. (1978). Existing rock physics modeling strategies are then applied to relate ice saturation to effective elastic properties. The modeling workflow thus enables us to estimate how altered surface temperatures affect the heat flux into cold, saline sediments, and the corresponding effects on the elastic properties of the near-surface unconsolidated sediments. As such, it provides a basis for seismic monitoring of thawing of frozen near-surface sediments associated with ongoing and future Arctic climate change.

Validity and limitations of the heat flux modeling

The bulk of geoscience research on the effects of a warmer climate in the Arctic focuses on heating of the oceans and atmosphere, and the associated thawing of sea ice, glaciers, and the ice cap of Greenland. The heating of the vast terrestrial areas with permafrost in the Northern hemisphere is less understood, and few studies on the effect of climate change on the permafrost in Svalbard are available. Our modeled freezing point isotherm for scenario T1 reaches a maximum depth of about 1.2 m, which is comparable to measurements of the current active layer thickness in Adventdalen (Christiansen et al., 2010). This suggests that despite the simplifications in our heat-flux modeling, it provides realistic estimates of the heat flux into the ground today, which is also supported by the good correlation between modeled and observed temperatures in Figure 4.

When it comes to future thawing, our heat-flux modeling approach is more difficult to verify. Isaksen et al. (2007) observe drastic permafrost temperature increases detectable down

to 15.0 m depth on Svalbard during a high temperature event within the range of temperature increase associated with future climate change. Our heat-flux modeling results are consistent with findings in the report “Climate in Svalbard 2100” (NCCS, 2019). The report suggests that the limit between whether permafrost remains or disappears by the year 2100 seems to be somewhere between RCP4.5 (our model T2) and RCP8.5 (our model T3). Figure 6a shows the maximum depth of the freezing point isotherm stabilizing at around 1.6 m depth for T2, while increasing in depth every year for T3.

How climate will actually change in the Arctic regions is a topic of great debate. Although most scientists agree that temperatures will increase drastically over the next decades, the temperature projections used here represent just a few of numerous possible future scenarios. We also make the assumption that the increase in air temperature will be transmitted somewhat unfiltered into the near surface, but alteration of snow cover, vegetation, and drainage will also affect the heat transfer. The spring snow cover in the Northern hemisphere is likely to decrease by 25% by the year 2100 under RCP8.5 (IPCC, 2014). Since snow is an efficient insulation to heat flux due to its very low thermal conductivity and high reflectivity, alteration of snow cover constitutes a complicated variable to take into account (Groisman et al., 1994; French, 2017). Increased surface temperatures can lead to increased vegetation, but also an increase in the frequency of forest fires (Tchebakova et al., 2009). Additionally, precipitation in the form of rain will likely increase by year 2100, leading to increased runoff due to both increased rainfall and meltwater volume (NCCS, 2019). The effects of heat flux caused by water infiltration are not considered here. In that respect, our modeled effects of heating of sediments are conservative, as convection may provide an efficient heat transport from the surface into the ground as the degree of freezing decreases.

Validity and limitations of the rock physics modeling

Deriving the effective elastic properties of partially frozen sediments is a complex process due to their strong dependence on the pore ice morphology. Dvorkin et al. (1994, 1999) and Dvorkin and Nur (1996) describe models for how elastic properties are affected by generation of ice at various pore-scale distributions, including ice occurring at grain contacts, ice coating the sediment grains, or ice filling the pore space. The first two models immediately act to stiffen the medium because the ice cements the grains together, while the latter model does not affect the effective stiffness significantly at low ice saturations because the ice is not initially in contact with the grains. Experimental results indicate that neither of these models can by itself explain the P-wave velocity observed during laboratory experiments with freezing/thawing sediments (Dou et al., 2016; Matsushima et al., 2016; Wu et al., 2017). We therefore instead choose to use the effective medium theory of Dou et al. (2017) due to the good agreement between the modeled P-wave velocities and the experimental results reported in Dou et al. (2016). Dou et al. (2016) did not measure S-wave velocities, but their modeled S-wave velocities coincide well with the experimental results of Matsushima et al. (2016). This approach inherently assumes a mix of both pore-filling and frame-strengthening ice forming at all ice saturations, which appears to be a decent approximation in unconsolidated sediments with low clay content (Dou et al., 2017). Although the approach of combining Hertz-Mindlin contact theory, self-consistent approach, and Hashin-Shtrikman bounds in itself has not been extensively tested, the individual approaches are all well known.

Impact of physical parameters on elastic properties

The geological model used here is a simplified representation of the geology in Adventdalen, which most certainly affects the results. We show that the salinity and saturation of the pore water are particularly important factors for the quantitative results, and our choice

of inaccurate parameters may have significantly affected the agreement between observed and modeled elastic properties. In this regard, the type and provenance of the near-surface sediments is crucial. Marine sediments contain salt, while extensive convection will over time act to reduce the salinity. We here assume a single low salinity in the upper 3.0 m, and a single higher salinity in the lower sediments, in addition to fully saturated sediments, even though Bratlie (2018) identify a range of salinities and saturations in a core from the area. Also, our model considers a simplified mineralogy and neglects the clay effects, which usually act to reduce the thermal conductivity and increase the unfrozen water content at low temperatures (Midttømme and Roaldset, 1998). This means that our modeled velocity profiles and corresponding seismic data are not exact representations of what would be collected in experiments in this area; however, the estimated degree of variation in elastic properties with time is likely relevant for terrestrial Arctic environments with saline unconsolidated sediments. Thus, our study provides valuable insight into how seismic studies can be useful for monitoring the warming of cold surface sediments.

As the pore fluid changes phase from brine to ice, a volume expansion of up to 9% will occur. In our rock physics modeling, we account for the volumetric deformation of the sediment during freezing and thawing by implementing an effective density that is a function of ice saturation, as given by equation 7. From this, it follows that the effective density is reduced as the ice saturation is increased, and hence, the seismic velocities computed using equations 5 and 6 are also slightly increased relative to assuming no volume expansion. However, pore volume expansion following phase change is ignored in our procedure for estimating ice saturation at a given temperature. Following Dou et al. (2017), the reasoning for making this assumption is that ice formation does not necessarily cause a linear pore volume expansion because some fraction of the ice may form without being in contact with the grains, especially in the early stages of freezing. The thicknesses of the layers in the model are also assumed to

be constant, but volume expansion would in nature typically lead to the generation of frost heave (Harris et al., 2009). Other effects of the volumetric deformation not accounted for in the modeling are due to the generation of cracks, including altered permeability that affects heat flux, and reduced strength of the frame which further acts to reduce the effect of increased effective shear modulus associated with the transition from brine to ice.

Estimating elastic properties of near-surface sediments from seismic data

Both the full waveform modeling of the seismic models adapted for various summer and winter scenarios and the real seismic data reveal significant time-lapse effects, indicating that seismic data can be used to detect near-surface thawing. However, to estimate near-surface temperature distribution, the seismic properties need to be inverted to elastic properties, which can then be related to temperature when the type of pore fluid is known. When the stiffnesses of the near-surface sediments increase with depth, the dispersion characteristics of surface-wave data can provide the vertical S-wave velocity profile by using the MASW inversion (Park et al., 1999). However, our results demonstrate that when the near surface is frozen, stiffness potentially decreases from surface and downward, and previous studies have shown that in this case, this technique cannot be used due to the presence of higher-order wave modes (O'Neill and Matsuoka, 2005; Dou and Ajo-Franklin, 2014). Thus, an inversion of the surface-wave properties for elastic parameters needs to be conducted more carefully, including higher-order wave modes. This means that the design of data acquisition and the inversion strategy has to be carefully planned. Since we do not know the exact local geology and pore fluid chemistry at the site of the real data experiment, it is beyond the scope of this study to analyze the seismic data in order to estimate near-surface temperature distribution here.

CONCLUSIONS

The contribution of our study is to provide a link between changing top ground temperature and the corresponding change in elastic parameters and mechanical strength of near-surface sediments in the Arctic. First, we have established a finite-element heat flux formulation for modeling vertical heat flux through a horizontally layered sediment model where each layer is defined by its heat transport properties. Based on well data providing the vertical lithology, fluid composition, and temperature, a one-year time series of top ground temperature data was used to model the corresponding temperature variation within the subsurface sediments. The modeled data were consistent with the well data, even though the effects of less conductive clay and convective heat transport were neglected. The heat-flux model was applied to various published future climate scenarios to evaluate future thawing of near-surface Arctic sediments. The modeled thawing depths were in agreement with other published studies. Second, the resulting subsurface isotherms were converted to ice saturation distribution, which was input to rock physics modeling of P- and S-wave velocities of the upper unconsolidated sediments.

Our study has demonstrated that elastic properties of shallow saline unconsolidated sediments are strongly affected by increasing the top ground temperature, even at subzero temperatures. The properties strongly depend on salinity at subzero temperatures, due to its dominating effect on ice saturation. Full waveform modeling of the various climate-related seismic models reveals how signatures of Rayleigh waves alter with the various temperature models for such sediments, and observed seismic data also reveal a seasonal time-lapse effect. Hence, time-lapse analysis of surface-wave data may potentially be used for evaluating the heat flux into the cold saline terrestrial Arctic. This may be important for evaluating the consequences of rising temperatures in the Arctic with respect to both the stability and

geomorphology of currently frozen sediments, and their sealing capacity to prevent emissions of greenhouse gases from within and below.

ACKNOWLEDGMENTS

This research is funded by ARCEX partners and the Research Council of Norway (grant number 228107). We would like to thank the CASE 2 consortium for sponsoring the fieldwork, and the reviewers for their constructive comments that helped significantly improve the manuscript.

APPENDIX A

Sensitivity analysis of the heat flux model

Figure A-1 illustrates the effect of increasing salinity on equivalent heat capacity and thermal conductivity, computed using the Heaviside function and the approach outlined in the section “Heat transport in cold sediments”. Increasing the salinity leads to a larger phase change interval, and thus heat capacity starts to increase and thermal conductivity starts to decrease at a lower temperature. We here assume that the dominant effect of salinity is on the phase change interval, and neglect the minor effect of progressive salination of the residual pore water on the density and thermal properties of pore water. We therefore use the thermal properties of non-saline water as defined in Table 1 for the water constituent in equations 2 and 3.

Figure A-2 shows various results of applying equations 2 and 3 on quartz sand with saturation and moisture content varying from 0 – 100%, and thus illustrates the impact of these physical properties on the thermal properties. We first consider increased water saturation (Figures A-2a and A-2c). As revealed by Table 1, air has a significantly lower heat capacity than water and slightly lower than ice, and a thermal conductivity significantly lower than ice and slightly lower than water. This means that increasing the water saturation increases both the effective heat capacity (most in the unfrozen state) and the effective thermal conductivity (most in the frozen state). Although this implies that saturation can affect the thawing depth of permafrost, the case of full saturation is often considered in such modeling studies (e.g., Mottaghy and Rath, 2006; Govaerts et al., 2016). The inset of Figure A-2a shows how increased latent heat follows increased water saturation. This is because water changes phase in the temperature range considered here, as opposed to air and matrix. Further, we consider the effect of increasing volumetric moisture content (Figures A-2b and A-2d). This causes higher latent heat, while it reduces the effective heat capacity in the frozen state, and increases it in the

unfrozen state, even though the matrix material has a lower heat capacity than both water and ice. This is an effect of the large density difference between matrix and ice, which is evident from Table 1 and equation 2. Since the effective thermal conductivity is independent of density, we see that increased moisture content causes it to decrease severely in the unfrozen state, and slightly in the frozen state due to the very low thermal conductivity of water and ice.

APPENDIX B

Rock physics modeling of unconsolidated sediments with varying ice saturation

Fully saturated unfrozen ground:

We start by computing effective dry rock moduli with Hertz-Mindlin contact theory (CT) (Mindlin, 1949)

$$K_{CT} = \left(\frac{n^2(1-\varphi_0)^2\mu_G^2}{18\pi^2(1-\nu_G)^2} P \right)^{\frac{1}{3}}, \quad (\text{B-1})$$

and

$$\mu_{CT} = \frac{5-4\nu_G}{5(2-\nu_G)} \left(\frac{3n^2(1-\varphi_0)^2\mu_G^2}{2\pi^2(1-\nu_G)^2} P \right)^{\frac{1}{3}}. \quad (\text{B-2})$$

The subscript CT means the effective dry rock moduli and the subscript G means the sediment grain property. K and μ are the bulk and shear modulus, respectively, ν is the Poisson's ratio, φ_0 is the porosity, P is the pressure, and n is the coordination number. We assume that we have spherical grains, and chose $n=8.6$ because it is well within the range of 8.0-9.0 that is considered typical for 36-40% porosity sandstones according to Dvorkin and Brevik (1999). Johansen et al. (2003) also use values within this range to model freezing of unconsolidated sediments.

We then compute the effective water-saturated rock properties with Gassmann fluid substitution (Gassmann, 1951)

$$K_{SatW} = K_G \frac{\varphi_0 K_{CT} - (1 + \varphi_0) K_W K_{CT} / K_G + K_W}{(1 - \varphi_0) K_W + \varphi_0 K_G - K_W K_{CT} / K_G}. \quad (\text{B-3})$$

The subscript satW means the effective fully water-saturated moduli, and the subscript W means water. The shear modulus is unaffected by the presence of a fluid, so

$$\mu_{satW} = \mu_{CT}. \quad (\text{B-4})$$

Fully saturated frozen ground

Further, we compute the effective elastic properties of the fully ice-saturated rock using the self-consistent approximation (SCA) of Berryman (1980a,b). The principle of the SCA is to assume that ice-filled pores and sediment grains are inclusions in a background medium with unknown properties. The strategy is to adjust the elastic properties of the background medium iteratively until the net scattering from a wave incident on the background medium with inclusions is zero. When this is accomplished, we have found the effective properties of the medium with matrix and ice-filled pores. In practice, this means we set up two scenarios, $j=\{1, 2\}$. Scenario 1 is for penny-shaped ice inclusions in a background medium, and scenario 2 is for spherical sediment grain inclusions in a background medium. We compute the elastic moduli K_j and μ_j for each scenario as a function of ice-filled rock effective moduli K_{satl} and μ_{satl} by using formulas from Berryman (1995)

$$K_1 = (K_i - K_{satl})S_i P_i, \quad (\text{B-5})$$

$$\mu_1 = (\mu_i - \mu_{satl})S_i Q_i, \quad (\text{B-6})$$

$$K_2 = (K_g - K_{satl})S_g P_g, \quad (\text{B-7})$$

$$\mu_2 = (\mu_g - \mu_{satl})S_g Q_g. \quad (\text{B-8})$$

S_i and S_g are the fractions of each inclusion type, and we use shape-dependent factors P_i , P_g , Q_i and Q_g as found in Dou et al. (2017)

$$P_i = \frac{K_{satl} + \frac{4}{3}\mu_i}{K_i + \frac{4}{3}\mu_i + \pi\alpha_i\beta^*}, \quad (\text{B-9})$$

$$Q_i = \frac{1}{5} \left(1 + \frac{8\mu_{satl}}{4\mu_i + \pi\alpha_i(\mu^* + 2\beta^*)} + 2 \frac{K_i + \frac{2}{3}(\mu_i + \mu_{satl})}{K_i + \frac{4}{3}\mu_i + \pi\alpha_i\beta^*} \right), \quad (\text{B-10})$$

$$P_g = \frac{K_{satI} + \frac{4}{3}\mu_{satI}}{K_g + \frac{4}{3}\mu_{satI}}, \quad (\text{B-11})$$

$$Q_g = \frac{\mu_{satI} + \zeta^*}{\mu_g + \zeta^*}, \quad (\text{B-12})$$

where α_i is the aspect ratio of the grains, and β^* and ζ^* are defined by

$$\beta^* = \mu_{satI} \frac{3K_{satI} + \mu_{satI}}{3K_{satI} + 4\mu_{satI}}, \quad (\text{B-13})$$

$$\zeta^* = \frac{\mu_{satI}}{6} \left(\frac{9K_{satI} + 8\mu_{satI}}{K_{satI} + 2\mu_{satI}} \right). \quad (\text{B-14})$$

We then require $K_1 + K_2 = 0$ and $\mu_1 + \mu_2 = 0$, and finally solve these equations iteratively for K_{satI} and μ_{satI} , our ice-filled rock effective elastic moduli.

Patchy saturated ground

For the case of a patchy saturated ground, we use the Hill average (Hill, 1963; Mavko et al., 2009) on the dry rock moduli and fully saturated moduli. For patchy water-saturated ground, this means

$$K_{patchyW} = \frac{1}{2} (K_{CT} + K_{satW}), \quad (\text{B-15})$$

$$\mu_{patchyW} = \frac{1}{2} (\mu_{CT} + \mu_{satW}), \quad (\text{B-16})$$

and for patchy ice-saturated ground, this means

$$K_{patchyI} = \frac{1}{2} (K_{CT} + K_{satI}), \quad (\text{B-17})$$

$$\mu_{patchyI} = \frac{1}{2} (\mu_{CT} + \mu_{satI}), \quad (\text{B-18})$$

with subscripts as defined above.

Partly frozen ground

For the case of a partly frozen zone, we compute elastic properties of a rock with pores filled with a water-ice mixture by following the approach in Dou et al. (2017), which is a modified version of the two-end-member mixing method proposed by Minshull et al. (1994). The strategy is to mix the two end-members computed using CT + Gassmann and SCA, respectively, with a modified version of Hashin-Shtrikman (1963) bounds where the volume fraction of each material in the original formulas are replaced with the amount of water or ice in the pore space, respectively s_w or s_i ($s_w + s_i = 1$ for fully saturated pore space). The Hashin-Shtrikman bounds are developed to mix two mineral phases, and this approach of mixing two multi-phase end-members has no physical basis, however, because of the good match between the model and experimental data in Dou et al. (2017), we nevertheless choose to follow their approach.

Hashin-Shtrikman bounds are upper and lower bounds for elastic moduli: K_{HS+} , K_{HS-} , μ_{HS+} , and μ_{HS-} . The effective properties K_{PF} and μ_{PF} at any given saturation are then simplified as the arithmetic average of these two bounds (Dou et al., 2017)

$$K_{PF} = \frac{1}{2}(K_{HS+} + K_{HS-}), \quad (\text{B-19})$$

$$\mu_{PF} = \frac{1}{2}(\mu_{HS+} + \mu_{HS-}), \quad (\text{B-20})$$

where

$$K_{HS+} = K_{satI} + \frac{s_w}{(K_{satW} - K_{satI})^{-1} + s_i(K_{satI} + \frac{4}{3}\mu_{satI})^{-1}}, \quad (\text{B-21})$$

$$K_{HS-} = K_{satW} + \frac{s_i}{(K_{satI} - K_{satW})^{-1} + s_w(K_{satW} + \frac{4}{3}\mu_{satW})^{-1}}, \quad (\text{B-22})$$

$$\mu_{HS+} = \mu_{satI} + \frac{s_w}{(\mu_{satW} - \mu_{satI})^{-1} + 2s_i} \frac{K_{satI} + 2\mu_{satI}}{5\mu_{satI}(K_{satI} + \frac{4}{3}\mu_{satI})}, \quad (B-23)$$

$$\mu_{HS-} = \mu_{satW} + \frac{s_i}{(\mu_{satI} - \mu_{satW})^{-1} + 2s_w} \frac{K_{satW} + 2\mu_{satW}}{5\mu_{satW}(K_{satW} + \frac{4}{3}\mu_{satW})}. \quad (B-24)$$

The subscript PF means partially frozen.

To find the elastic moduli of partly frozen, patchy saturated ground, we follow exactly the same approach, but replace the elastic end-members with the patchy saturation moduli $K_{patchy,w}$, $K_{patchy,i}$, $\mu_{patchy,w}$, and $\mu_{patchy,i}$ computed using the approach described above.

REFERENCES

- Andersland, O. B. and Ladanyi, B., 1994, An introduction to Frozen ground engineering: Chapman & Hall.
- Berryman, J. G., 1980a, Long-wavelength approximation in composite elastic media I: Spherical inclusions: *The Journal of the Acoustical Society of America*, **68**, 1809–1819, doi: 10.1121/1.385171.
- Berryman, J. G., 1980b, Long-wavelength approximation in composite elastic media II: Ellipsoidal inclusions: *The Journal of the Acoustical Society of America*, **68**, 1820–1831, doi: 10.1121/1.385172.
- Berryman, J. G., 1995, Mixture theories for rock properties, *in* T. J. Ahrens, ed., *Rock physics & phase relations: A handbook of physical constants: American Geophysical Union*, 205–228.
- Biskaborn, B. K., S. L. Smith, J. Noetzli, H. Matthes, G. Vieira, D. A. Streletskiy, P. Schoeneich, V. E. Romanovsky, A. G. Lewkowicz, A. Abramov, and M. Allard, 2019, Permafrost is warming at a global scale: *Nature communications*, **10**, 264, doi: 10.1038/s41467-018-08240-4.
- Bratlie, U. H. H., 2018, An Experimental Study of Thermal Properties of Permafrost Soils: M.S. thesis, Norwegian University of Science and Technology.
- Briggs, M. A., S. Campbell, J. Nolan, M. A. Walvoord, D. Ntarlagiannis, F. D. Day-Lewis, and J. W. Lane, 2016, Surface geophysical methods for characterising frozen ground in transitional permafrost landscapes: *Permafrost and Periglacial Processes*, **28**, 52-65, doi: 10.1002/ppp.1893.

Burn, C. R., 1998, The active layer: two contrasting definitions: Permafrost and Periglacial Processes, **9**, 411-416.

Carcione, J.M., and G. Seriani, 1998, Seismic and ultrasonic velocities in permafrost: Geophysical Prospecting, **46**, 441-454, doi: 10.1046/j.1365-2478.1998.1000333.x.

Christiansen, H. H., B. Etzelmüller, K. Isaksen, H. Juliussen, H. Farbrot, O. Humlum, M. Johansson, T. Ingeman-Nielsen, L. Kristensen, J. Hjort, and P. Holmlund, 2010, The thermal state of permafrost in the Nordic area during the International Polar Year 2007–2009: Permafrost and Periglacial Processes, **21**, 156-181, doi: 10.1002/ppp.687.

Comyn-Platt, E., G. Hayman, C. Huntingford, S. E. Chadburn, E. J. Burke, A. B. Harper, W. J. Collins, C. P. Webber, T. Powell, P. M. Cox, and N. Gedney, 2018, Carbon budgets for 1.5 and 2 °C targets lowered by natural wetland and permafrost feedbacks: Nature Geoscience, **11**, 568-573, doi: 10.1038/s41561-018-0174-9.

de Vries, D. A., 1963, Thermal properties of soils, *in* W. R. Wijk, ed., Physics of Plant Environment: North-Holland Publishing Corporation, 210–235.

Dou, S., and J. Ajo-Franklin, 2014, Full-wavefield inversion of surface waves for mapping embedded low-velocity zones in permafrost: Geophysics, **79**, no. 6, EN107–EN124, doi: 10.1190/geo2013-0427.1.

Dou, S., S. Nakagawa, D. Dreger, and J. Ajo-Franklin, 2016, A rock-physics investigation of unconsolidated saline permafrost: P-wave properties from laboratory ultrasonic measurements: Geophysics, **81**, no. 1, WA233-WA245, doi: 10.1190/geo2015-0176.1.

Dou, S., S. Nakagawa, D. Dreger, and J. Ajo-Franklin, 2017, An effective-medium model for P-wave velocities of saturated, unconsolidated saline permafrost: Geophysics, **82**, no. 3, EN33-EN50, doi: 10.1190/geo2016-0474.1.

-
- Dvorkin, J., A. Nur, and H. Yin, 1994, Effective properties of cemented granular materials: *Mechanics of Materials*, **18**, 351–366, doi: 10.1016/0167-6636(94)90044-2.
- Dvorkin, J., and A. Nur, 1996, Elasticity of high-porosity sandstones: Theory for two North Sea data sets: *Geophysics*, **61**, 1363-1370, doi: 10.1190/1.1444059.
- Dvorkin, J., J. Berryman, and A. Nur, 1999, Elastic moduli of cemented sphere packs: *Mechanics of Materials*, **31**, 461–469, doi: 10.1016/S0167-6636(99)00009-5.
- Dvorkin, J., and I. Brevik, 1999, Diagnosing high-porosity sandstones: Strength and permeability from porosity and velocity: *Geophysics*, **64**, 795-799, doi: 10.1190/1.1444589.
- Ecker, C., J. Dvorkin, and A. Nur, 1998, Sediments with gas hydrates: Internal structure from seismic AVO: *Geophysics*, **63**, 1659–1669, doi: 10.1190/1.1444462.
- Etzelmüller, B., T. V. Schuler, K. Isaksen, H. H. Christiansen, H. Farbrot, and R. Benestad, 2011, Modeling the temperature evolution of Svalbard permafrost during the 20th and 21st century: *The Cryosphere*, **5**, 67-79, doi: 10.5194/tc-5-67-2011.
- French, H. M., 2017, *The periglacial environment*: John Wiley & Sons.
- Gassmann, F., 1951, Elastic waves through a packing of spheres: *Geophysics*, **16**, 673-685, doi: 10.1190/1.1437718.
- Gilbert, G. L., H. B. O'Neill, W. Nemeč, C. Thiel, H. H. Christiansen, and J. P. Buylaert, 2018, Late Quaternary sedimentation and permafrost development in a Svalbard fjord-valley, Norwegian high Arctic: *Sedimentology*, **65**, 2531-2558, doi: 10.1111/sed.12476.
- Govaerts, J., K. Beerten, and J. T. Veen, 2016, Weichselian permafrost depth in the Netherlands: a comprehensive uncertainty and sensitivity analysis: *The Cryosphere*, **10**, 2907-2922, doi: 10.5194/tc-10-2907-2016.

Groisman, P. Y., T. R. Karl, and R. W. Knight, 1994, Observed impact of snow cover on the heat balance and the rise of continental spring temperatures: *Science*, **263**, 198-200, doi: 10.1126/science.263.5144.198.

Harris, C., L. U. Arenson, H. H. Christiansen, B. Etzelmüller, R. Frauenfelder, S. Gruber, W. Haerberli, C. Hauck, M. Hoelzle, O. Humlum, and K. Isaksen, 2009, Permafrost and climate in Europe: Monitoring and modelling thermal, geomorphological and geotechnical responses: *Earth-Science Reviews*, **92**, 117-171, doi: 10.1016/j.earscirev.2008.12.002.

Hashin, Z., and S. Shtrikman, 1963, A variational approach to the theory of the elastic behaviour of multiphase materials: *Journal of the Mechanics and Physics of Solids*, **11**, 127–140, doi: 10.1016/0022-5096(63)90060-7.

Hill, R., 1963, Elastic properties of reinforced solids: Some theoretical principles: *Journal of the Mechanics and Physics of Solids*, **11**, 357–372, doi: 10.1016/0022-5096(63)90036-x.

Hjort, J., O. Karjalainen, J. Aalto, S. Westermann, V. E. Romanovsky, F. E. Nelson, B. Etzelmüller, and M. Luoto, 2018, Degrading permafrost puts Arctic infrastructure at risk by mid-century: *Nature Communications*, **9**, 5147, doi: 10.1038/s41467-018-07557-4.

IPCC, 2014, *Climate Change 2014: Synthesis Report. Contribution of Working Groups I, II and III to the Fifth Assessment Report of the Intergovernmental Panel on Climate Change*, Core Writing Team, R. K. Pachauri and L. A. Meyer, eds.

Isaksen, K., R. E. Benestad, C. Harris, and J. L. Sollid, 2007, Recent extreme near-surface permafrost temperatures on Svalbard in relation to future climate scenarios: *Geophysical Research Letters*, **34**, L17502, doi:10.1029/2007GL031002.

-
- Johansen, T. A., P. Digranes, M. van Schaack, and I. Lønne, 2003, Seismic mapping and modeling of near-surface sediments in polar areas: *Geophysics*, **68**, 566-573, doi: 10.1190/1.1567226.
- Kane, D. L., K. M. Hinkel, D. J. Goering, L. D. Hinzman, and S. I. Outcalt, 2001, Non-conductive heat transfer associated with frozen soils: *Global and Planetary Change*, **29**, 275-292, doi: 10.1016/s0921-8181(01)00095-9.
- Keating, K., A. Binley, V. Bense, R. L. Van Dam, and H. H. Christiansen, 2018, Combined geophysical measurements provide evidence for unfrozen water in permafrost in the Adventdalen valley in Svalbard: *Geophysical Research Letters*, **45**, 7606-7614, doi: 10.1029/2017gl076508.
- King, M. S., R. W. Zimmerman, and R. F. Corwin, 1988, Seismic and electrical properties of unconsolidated permafrost: *Geophysical Prospecting*, **36**, 349-364, doi: 10.1111/j.1365-2478.1988.tb02168.x.
- Kitover, D. C., R. T. van Balen, D. M. Roche, J. Vandenberghe, and H. Renssen, 2013, New estimates of permafrost evolution during the last 21 k years in Eurasia using numerical modelling: *Permafrost and Periglacial Processes*, **24**, 286-303, doi: 10.1002/ppp.1787.
- Kneisel, C., C. Hauck, R. Fortier, and B. Moorman, 2008, Advances in geophysical methods for permafrost investigations: *Permafrost and Periglacial Processes*, **19**, 157-178, doi: 10.1002/(ISSN)1099-1530.
- Matsushima, J., M. Suzuki, Y. Kato, and S. Rokugawa, 2016, Ultrasonic measurements of attenuation and velocity of compressional and shear waves in partially frozen unconsolidated sediment and synthetic porous rock: *Geophysics*, **81**, no. 2, D141-D153, doi: 10.1190/geo2015-0350.1.

- Mavko, G., T. Mukerji, and J. Dvorkin, 2009, *Rock physics handbook: Tools for seismic analysis in porous media*, 2nd ed.: Cambridge University Press.
- Midttømme, K., and E. Roaldset, 1998, The effect of grain size on thermal conductivity of quartz sands and silts: *Petroleum Geoscience*, **4**, 165-172, doi: 10.1144/petgeo.4.2.165.
- Mindlin, R. D., 1949, Compliance of elastic bodies in contact: *Journal of Applied Mechanics*, **16**, 259–268.
- Minshull, T. A., S. C. Singh, and G. K. Westbrook, 1994, Seismic velocity structure at a gas hydrate reflector, offshore western Colombia, from full waveform inversion: *Journal of Geophysical Research: Solid Earth*, **99**, 4715-4734, doi: 10.1029/93JB03282.
- Mottaghy, D., and V. Rath, 2006, Latent heat effects in subsurface heat transport modelling and their impact on palaeotemperature reconstructions: *Geophysical Journal International*, **164**, 236-245, doi: 10.1111/j.1365-246x.2005.02843.x.
- Muller, S. W., 1947, *Permafrost or Permanently Frozen Ground and Related Engineering Problems*: J. W. Edwards.
- NCCS, 2019, *Climate in Svalbard 2100 – a knowledge base for climate adaptation*, I.Hanssen-Bauer, E. J. Førland, H. Hisdal, S. Mayer, A. B. Sandø, A. Sorteberg, eds.: The Norwegian Centre for Climate Services, report no. M-1242, 1/2019.
- Nelson, F. E., O. A. Anisimov, and N. I. Shiklomanov, 2001, Subsidence risk from thawing permafrost: *Nature*, **410**, 889, doi: 10.1038/35073746.
- O'Neill, A., and T. Matsuoka, 2005, Dominant higher surface-wave modes and possible inversion pitfalls: *Journal of Environmental & Engineering Geophysics*, **10**, 185-201, doi: 10.2113/jeeg10.2.185.

-
- Overland, J. E., M. Wang, J. E. Walsh, and J. C. Stroeve, 2014, Future Arctic climate changes: Adaptation and mitigation time scales: *Earth's Future*, **2**, 68-74, doi: 10.1002/2013ef000162.
- Park, C.B., R. D. Miller, J. Xia, 1999, Multichannel analysis of surface waves: *Geophysics*, **64**, 800-808, doi: 10.1190/1.1444590.
- Potter, R. W., M. A. Clynne, and D. L. Brown, 1978, Freezing point depression of aqueous sodium chloride solutions: *Economic Geology*, **73**, 284-285, doi: 10.2113/gsecongeo.73.2.284.
- Pryor, R. W., 2009, *Multiphysics modeling using COMSOL®: a first principles approach*: Jones & Bartlett Publishers.
- Romanovsky, V. E., and T. E. Osterkamp, 2000, Effects of unfrozen water on heat and mass transport processes in the active layer and permafrost: *Permafrost and Periglacial Processes*, **11**, 219-239.
- Seneviratne, S. I., M. G. Donat, A. J. Pitman, R. Knutti, and R. L. Wilby, 2016, Allowable CO₂ emissions based on regional and impact-related climate targets: *Nature*, **529**, 477, doi: 10.1038/nature16542.
- Schmidt, H. and F. B. Jensen, 1985, A full wave solution for propagation in multilayered viscoelastic media with application to Gaussian beam reflection at fluid–solid interfaces: *The Journal of the Acoustical Society of America*, **77**, 813-825, doi: 10.1121/1.392050.
- Schoolmeester, T., H. L. Gjerdi, J. Crump, B. Alfthan, J. Fabres, K. Johnsen, L. Puikkonen, T. Kurvits, and E. Baker, 2019, *Global Linkages – A graphic look at the changing Arctic*: UN Environment and GRID-Arendal.

Schuur, E. A., A. D. McGuire, C. Schädel, G. Grosse, J. W. Harden, D. J. Hayes, G. Hugelius, C. D. Koven, P. Kuhry, D. M. Lawrence, and S. M. Natali, 2015, Climate change and the permafrost carbon feedback: *Nature*, **520**, 171.

Tchebakova, N. M., E. Parfenova, and A. J. Soja, 2009, The effects of climate, permafrost and fire on vegetation change in Siberia in a changing climate: *Environmental Research Letters*, **4**, 045013, doi: 10.1088/1748-9326/4/4/045013.

Timur, A., 1968, Velocity of compressional waves in porous media at permafrost temperatures: *Geophysics*, **33**, 584-595, doi: 10.1190/1.1439954.

TSP Norway (Permafrost Observatory Project: A Contribution to the Thermal State of Permafrost in Norway and Svalbard), 2013, Old Auroral station 2/AS-B-2 Data Set, The Norwegian Permafrost Database, Geological Survey of Norway (NGU). Data set accessed 05 March 2019 at http://aps.ngu.no/pls/oradb/minres_bo_fakta.boho?p_id=126&p_spraak=E.

Tsuji, T., T. A. Johansen, B. O. Ruud, T. Ikeda, and T. Matsuoka, 2012, Surface-wave analysis for identifying unfrozen zones in subglacial sediments S-wave velocity in subglacial sediment: *Geophysics*, **77**, no. 3, EN17-EN27, doi: 10.1190/geo2011-0222.1.

Veuille, S., D. Fortier, M. Verpaelst, K. Grandmont, and S. Charbonneau, 2015, Heat advection in the active layer of permafrost: physical modelling to quantify the impact of subsurface flow on soil thawing: 68th Canadian Geotechnical Conference and 7th Canadian Permafrost Conference, Proceedings, 722.

Weismüller, J., U. Wollschläger, J. Boike, X. Pan, Q. Yu, and K. Roth, 2011, Modeling the thermal dynamics of the active layer at two contrasting permafrost sites on Svalbard and on the Tibetan Plateau: *The Cryosphere*, **5**, 741, doi: 10.5194/tc-5-741-2011.

Wu, Y., S. Nakagawa, T. J. Kneafsey, B. Dafflon, and S. Hubbard, 2017, Electrical and seismic response of saline permafrost soil during freeze-thaw transition: *Journal of Applied Geophysics*, **146**, 16-26, doi: 10.1016/j.jappgeo.2017.08.008.

Xia, J., R. D. Miller, and C. B. Park, 1999, Estimation of near-surface shear-wave velocity by inversion of Rayleigh waves: *Geophysics*, **64**, 691-700, doi: 10.1190/1.1444578.

Zhang, Y., S. K. Carey, and W. L. Quinton, 2008, Evaluation of the algorithms and parameterizations for ground thawing and freezing simulation in permafrost regions: *Journal of Geophysical Research: Atmospheres*, **113**, D17116, doi:10.1029/2007JD009343 .

Zimmerman, R.W. and M. S. King, 1986, The effect of the extent of freezing on seismic velocities in unconsolidated permafrost: *Geophysics*, **51**, 1285-1290, doi: 10.1190/1.1442181.

FIGURE AND TABLE CAPTIONS

Figure 1: The top ground temperature affects the temperature distribution T with depth z . The active layer is defined as the layer that experiences $T > 0^\circ\text{C}$ annually (Muller, 1947). Freezing point depression due to, e.g., salinity can lower the temperature where ice starts to form, and so the active layer thickness is not necessarily equal to the seasonally thawed layer thickness. Climate projections point to increasing top ground temperatures in the future, which means increased active layer thickness, increased seasonally thawed layer thickness, and increased thickness of the layer that is affected by seasonal temperature variations. Modified after Andersland and Ladanyi (1994) and Burn (1998).

Figure 2: Ice saturation varies with temperature for saline water. The figure shows ice saturation at subzero temperatures for pore water with initial salinities of 25 parts per thousand (ppt) and 3 ppt, based on the equations by Potter et al. (1978).

Figure 3: Map of study area, with location of well AS-B-2 marked with a red dot (maps courtesy of Norwegian Polar Institute).

Figure 4: Modeled temperatures compared with temperatures measured in the well in Adventdalen on four selected dates: a) 30th of September, b) 31st of December, c) 31st of March, and d) 30th of June. The modeling ran for a year before the modeled temperatures were extracted. The corresponding measured top ground temperatures are indicated by arrows in Figure 5a.

Figure 5: a) Hourly top ground temperatures measured in well AS-B-2 for one year from 10th of August 2012. In the heat flux modeling, we repeat this time series four times. The red arrows mark the dates displayed in Figure 4. b) Hourly top ground temperatures for the situation of today (T1), the year 2100 for RCP4.5 (T2), and the year 2100 for RCP8.5 (T3). We only display three months here, starting 29th of September.

Figure 6: Thawing depth from the heat flux modeling for the scenarios defined in Table 3. The -0.17°C isotherm (freezing point for 3 ppt salinity pore water) is plotted for all scenarios, except S2, where the 0°C isotherm is plotted due to the non-saline pore water in that specific scenario. The modeling runs for four years (starting 10th of August) to assure that the system is stabilized to some extent since the heat flux from the surface to the underlying sediments is a slow process. Some minor inter-annual variations are evident due to the complexity of the upper boundary condition and the finite element scheme itself, but do not significantly affect the observed trends. Modeled thawing depth for: a) Top ground temperature T1 (today), T2 (RCP4.5), and T3 (RCP8.5). b) Non-saline permafrost and 3 ppt salinity permafrost when top ground temperature is T1. c) Saturation from 0 to 100% when top ground temperature is T1. d) Model with and without lenticular ice at 2.0–3.0 m depth when top ground temperature is T1 and T3.

Figure 7: Schematic illustration of the rock physics modeling approach we use in this study to model patchy and fully saturated ground with 0 to 100% ice in the pore space. First, elastic properties of unfrozen (Member A) and frozen (Member B) unconsolidated sand in various states (1) – (5) are computed using the rock physics models listed in Table 4. Note that technically, completely dry sand cannot be frozen due to the lack of moisture, and can therefore not by itself constitute Member B, but only as part of state (5). Subsequently, elastic properties of sand with varying ice saturation are computed by assuming that the case of disconnected ice is estimated by the lower Hashin-Shtrikman bound (Member B embedded in Member A), and the case of connected ice is estimated by the upper Hashin-Shtrikman bound (Member A embedded in Member B). See Appendix B for details.

Figure 8: Elastic moduli computed using the approach illustrated in Figure 7 assuming fully or patchy 50% saturated pores, and seismic velocities computed using equations 5 and 6. Elastic moduli and seismic velocities change with ice saturation in the partly frozen zone. HS+ is the

upper Hashin-Shtrikman bound, HS- is the lower Hashin-Shtrikman bound. The seismic velocities are computed from the Hill average elastic moduli. a) Bulk modulus, b) Shear modulus, c) P-wave velocity, d) S-wave velocity.

Figure 9: Variation in a)-b) temperature, c)-d) P-wave velocity, and e)-f) S-wave velocity with time for the fourth year in Figure 6a for T1 (today), T2 (RCP4.5), and T3 (RCP8.5) at 1.0 m depth (left column), and 3.0 m depth (right column). We assume constant matrix moduli and porosity with depth, and full saturation.

Figure 10: Variation in a)-b) temperature, c)-d) P-wave velocity, and e)-f) S-wave velocity with depth for T1 (today), T2 (RCP4.5), and T3 (RCP8.5) in February (left column), and August (right column) of the fourth year in Figure 6a. We assume constant matrix moduli and porosity with depth, and full saturation. The transition from 3 ppt salinity to 25 ppt salinity at 3.0 m depth has a large impact on the seismic velocities.

Figure 11: Synthetic seismograms created using OASES for scenarios T1 (today), T2 (RCP4.5), and T3 (RCP8.5) for the same calendar times as in Figure 10.

Figure 12: Unprocessed real seismic data recorded on vertical component geophones with one meter receiver interval in Adventdalen before (May) and after (September) summer thawing occurred. The seismic source was a sledgehammer at 25.0 m offset. The May data is displayed with a gain of 20 dB more than the September data. The linear event starting at approximately 80 ms in both gathers is the air wave traveling at 330 m/s.

Figure A-1: The effect of increasing the salinity of the pore water in a pure quartz sandstone on equivalent heat capacity and thermal conductivity. The properties are modeled with equations 2 and 3, using the Heaviside function to represent the phase change. This not an accurate

physical representation, but it is a decent approximation at modest subzero temperatures and low salinities.

Figure A-2: The effect of changing model parameters of quartz sand on thermal properties, displayed for a phase change interval from -1°C to 0°C for clarity. a) Impact of saturation on equivalent heat capacity (30% porosity). Full extent in small window, detailed view in main window. Both windows have the same axes units. b) Impact of moisture content on equivalent heat capacity (full water saturation), c) impact of saturation on thermal conductivity (30% porosity), and d) impact of moisture content on thermal conductivity (full water saturation).

Table 1: Typical values for heat capacity, thermal conductivity, and density based on Midttømme and Roaldset (1998), Mavko et al. (2009), and Govaerts et al. (2016). Additionally, the latent heat of fusion for water is 333.6 kJ/kg.

Table 2: Properties of the layers used in the 1D model in this study. We consider a simplified model consisting only of quartz sand and silt, even though Gilbert et al., (2018) report a variety of minerals and clay content in cores from the Adventdalen area.

Table 3: The scenarios we use for modeling thawing depth in this study. Except from the perturbed parameter, the properties from Table 2 are used in all scenarios.

Table 4: List of the rock physics models used to compute effective elastic properties of unconsolidated sand in the various states illustrated in Figure 7. Details of the rock physics models are outlined in Appendix B.

FIGURE 1

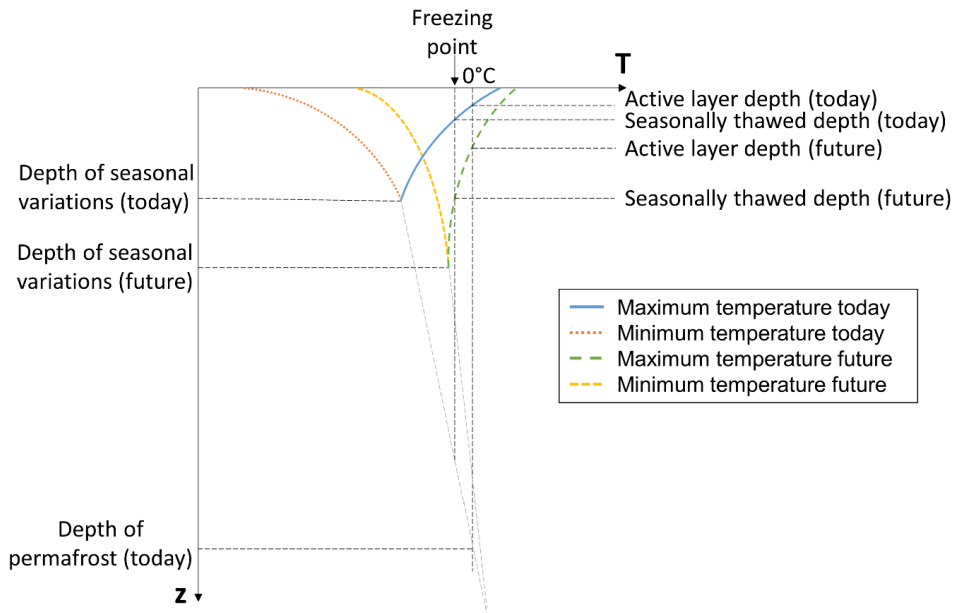


Figure 1: The top ground temperature affects the temperature distribution T with depth z . The active layer is defined as the layer that experiences $T > 0^{\circ}\text{C}$ annually (Muller, 1947). Freezing point depression due to, e.g., salinity can lower the temperature where ice starts to form, and so the active layer thickness is not necessarily equal to the seasonally thawed layer thickness. Climate projections point to increasing top ground temperatures in the future, which means increased active layer thickness, increased seasonally thawed layer thickness, and increased thickness of the layer that is affected by seasonal temperature variations. Modified after Andersland and Ladanyi (1994) and Burn (1998).

FIGURE 2

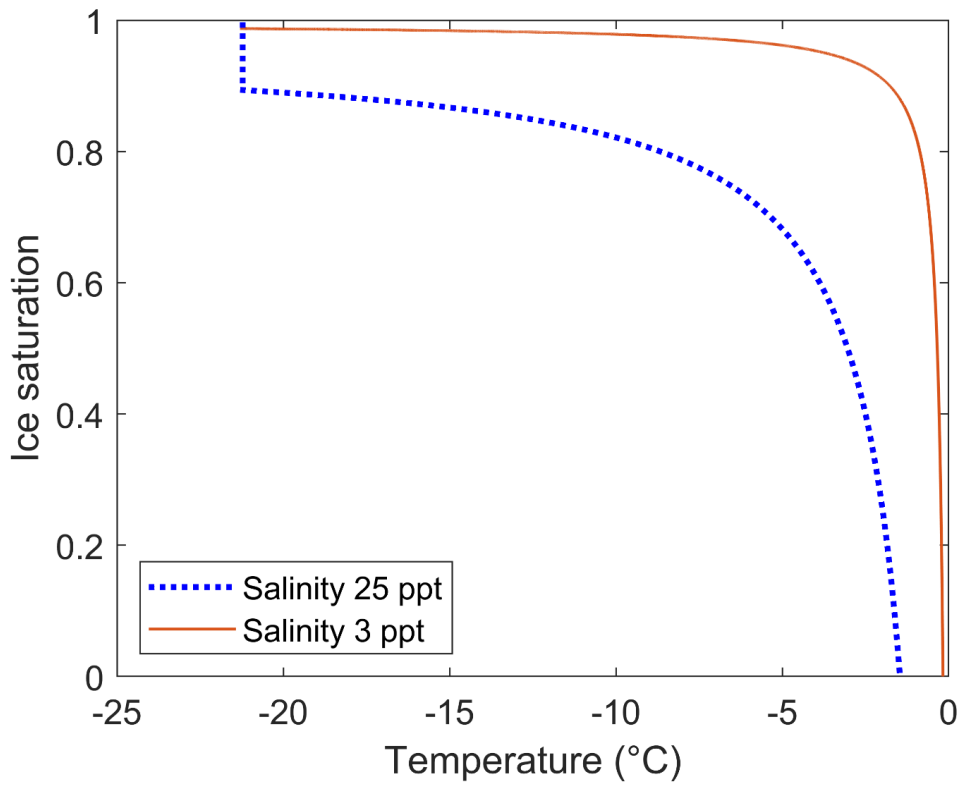


Figure 2: Ice saturation varies with temperature for saline water. The figure shows ice saturation at subzero temperatures for pore water with initial salinities of 25 parts per thousand (ppt) and 3 ppt, based on the equations by Potter et al. (1978).

FIGURE 3

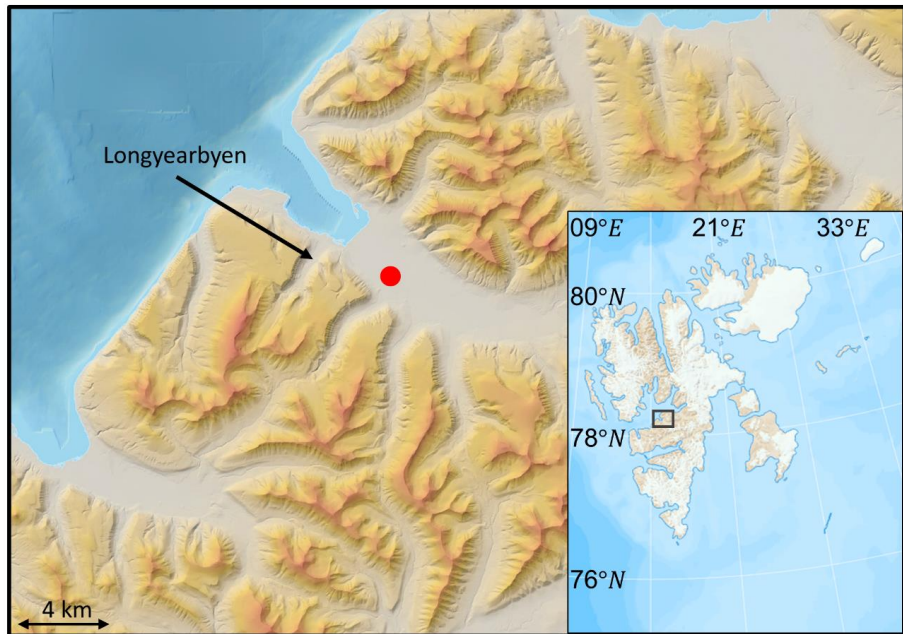


Figure 3: Map of study area, with location of well AS-B-2 marked with a red dot (maps courtesy of Norwegian Polar Institute).

FIGURE 4

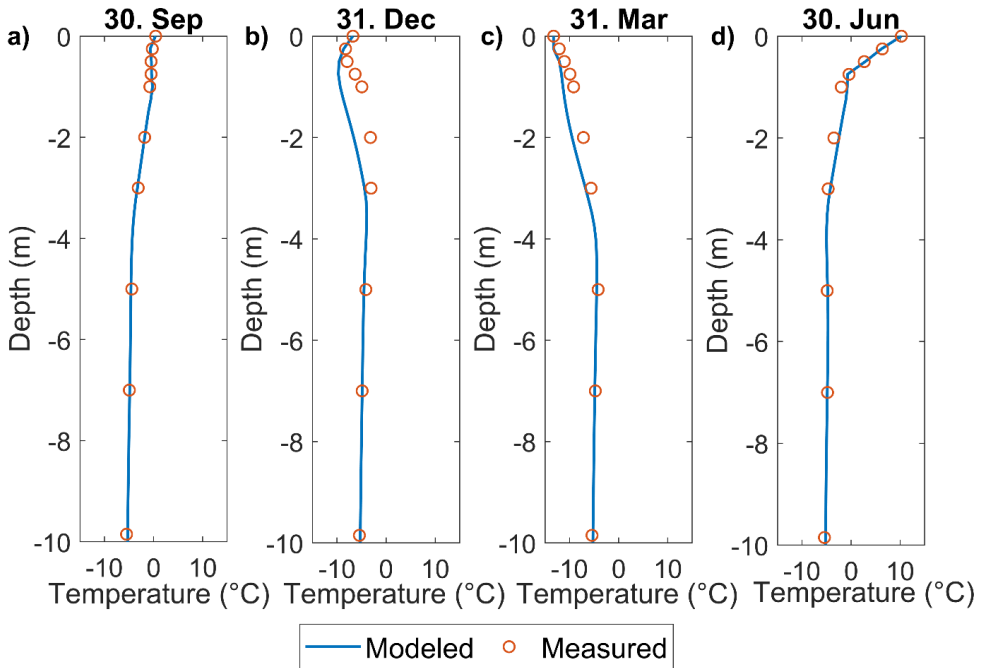


Figure 4: Modeled temperatures compared with temperatures measured in the well in Adventdalen on four selected dates: a) 30th of September, b) 31st of December, c) 31st of March, and d) 30th of June. The modeling ran for a year before the modeled temperatures were extracted. The corresponding measured top ground temperatures are indicated by arrows in Figure 5a.

FIGURE 5

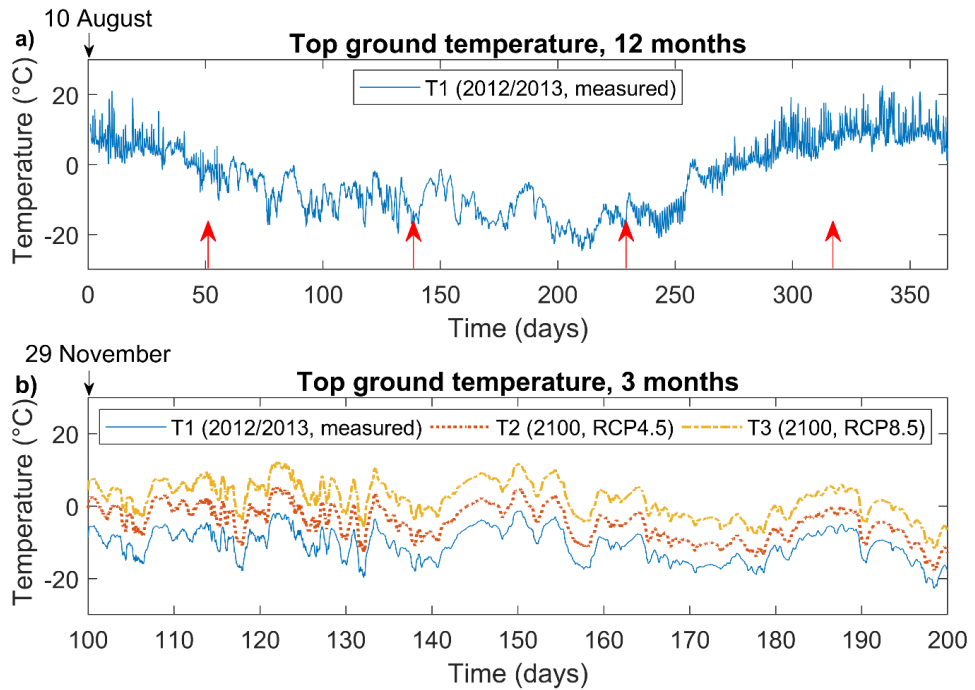


Figure 5: a) Hourly top ground temperatures measured in well AS-B-2 for one year from 10th of August 2012. In the heat flux modeling, we repeat this time series four times. The red arrows mark the dates displayed in Figure 4. b) Hourly top ground temperatures for the situation of today (T1), the year 2100 for RCP4.5 (T2), and the year 2100 for RCP8.5 (T3). We only display three months here, starting 29th of September.

FIGURE 6

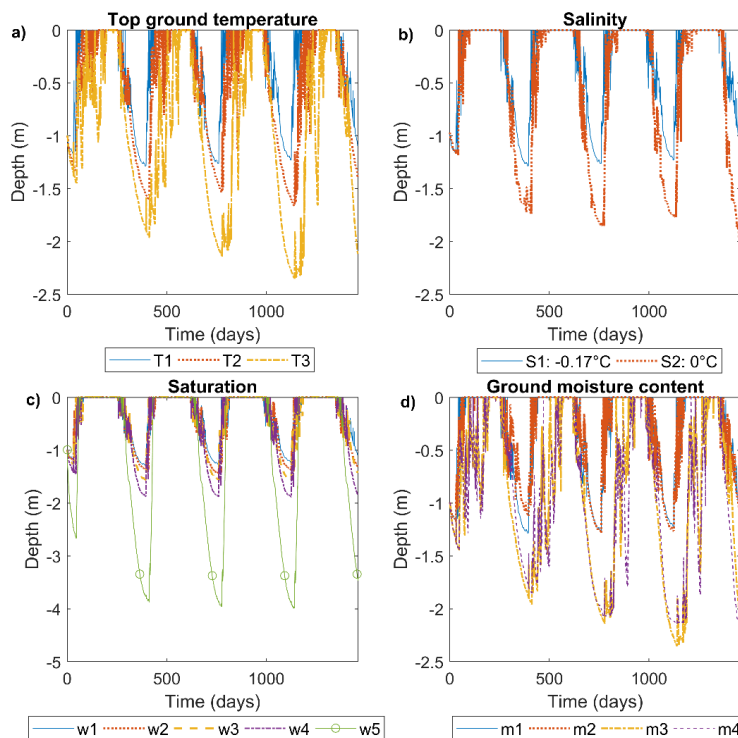


Figure 6: Thawing depth from the heat flux modeling for the scenarios defined in Table 3. The -0.17°C isotherm (freezing point for 3 ppt salinity pore water) is plotted for all scenarios, except S2, where the 0°C isotherm is plotted due to the non-saline pore water in that specific scenario. The modeling runs for four years (starting 10th of August) to assure that the system is stabilized to some extent since the heat flux from the surface to the underlying sediments is a slow process. Some minor inter-annual variations are evident due to the complexity of the upper boundary condition and the finite element scheme itself, but do not significantly affect the observed trends. Modeled thawing depth for: a) Top ground temperature T1 (today), T2 (RCP4.5), and T3 (RCP8.5). b) Non-saline permafrost and 3 ppt salinity permafrost when top ground temperature is T1. c) Saturation from 0 to 100% when top ground temperature is T1. d) Model with and without lenticular ice at 2.0–3.0 m depth when top ground temperature is T1 and T3.

FIGURE 7

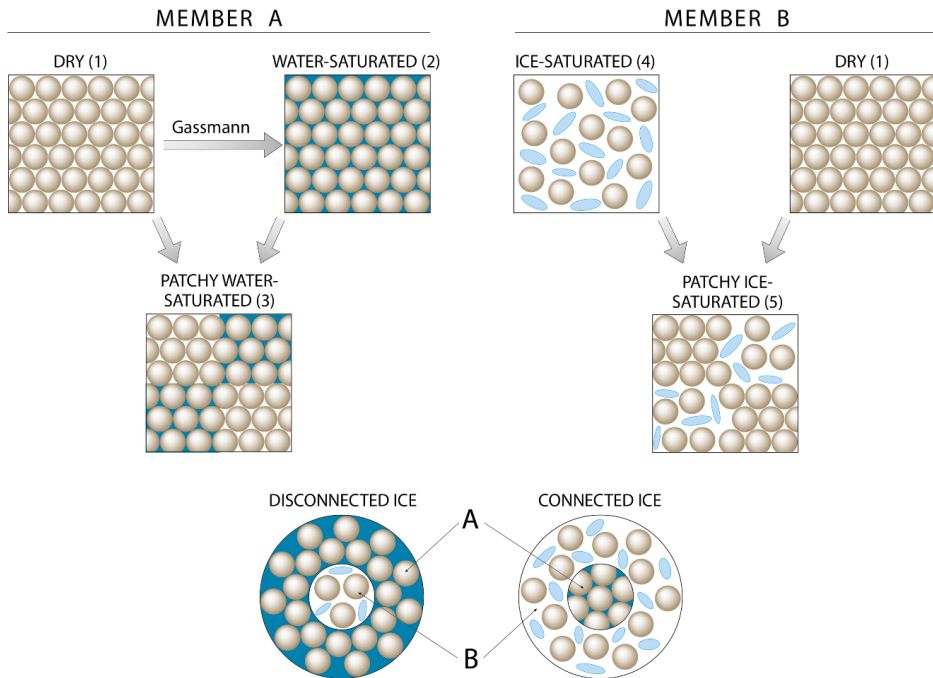


Figure 7: Schematic illustration of the rock physics modeling approach we use in this study to model patchy and fully saturated ground with 0 to 100% ice in the pore space. First, elastic properties of unfrozen (Member A) and frozen (Member B) unconsolidated sand in various states (1) – (5) are computed using the rock physics models listed in Table 4. Note that technically, completely dry sand cannot be frozen due to the lack of moisture, and can therefore not by itself constitute Member B, but only as part of state (5). Subsequently, elastic properties of sand with varying ice saturation are computed by assuming that the case of disconnected ice is estimated by the lower Hashin-Shtrikman bound (Member B embedded in Member A), and the case of connected ice is estimated by the upper Hashin-Shtrikman bound (Member A embedded in Member B). See Appendix B for details.

FIGURE 8

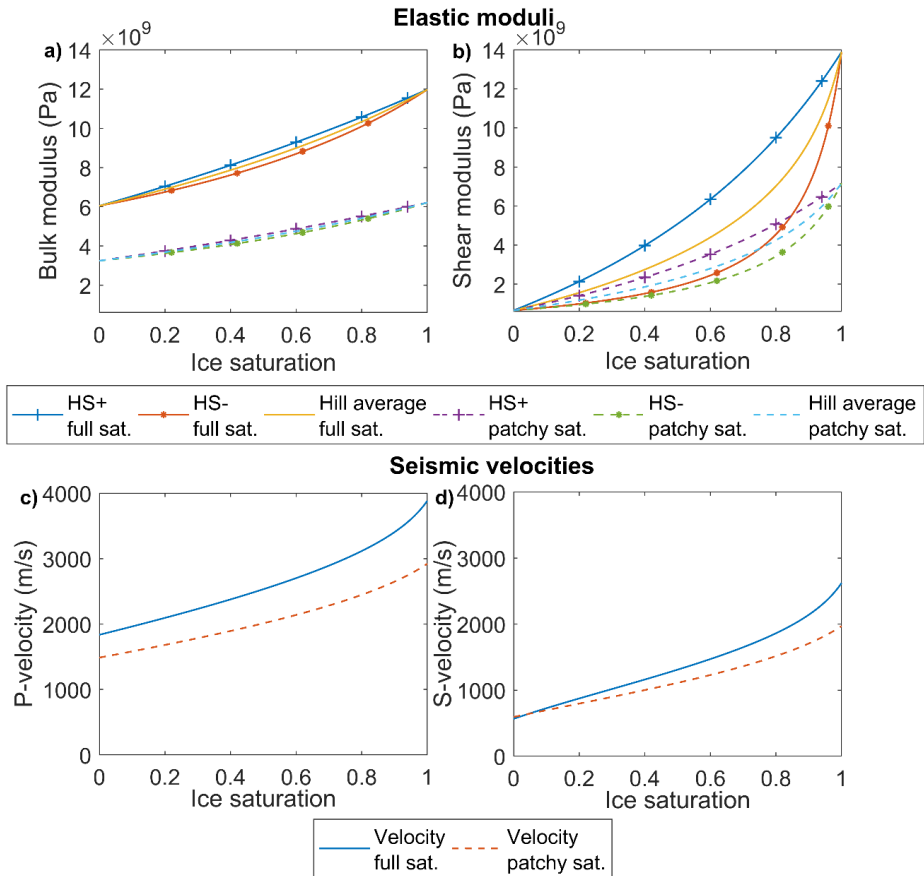


Figure 8: Elastic moduli computed using the approach illustrated in Figure 7 assuming fully or patchy 50% saturated pores, and seismic velocities computed using equations 5 and 6. Elastic moduli and seismic velocities change with ice saturation in the partly frozen zone. HS+ is the upper Hashin-Shtrikman bound, HS- is the lower Hashin-Shtrikman bound. The seismic velocities are computed from the Hill average elastic moduli. a) Bulk modulus, b) Shear modulus, c) P-wave velocity, d) S-wave velocity.

FIGURE 9

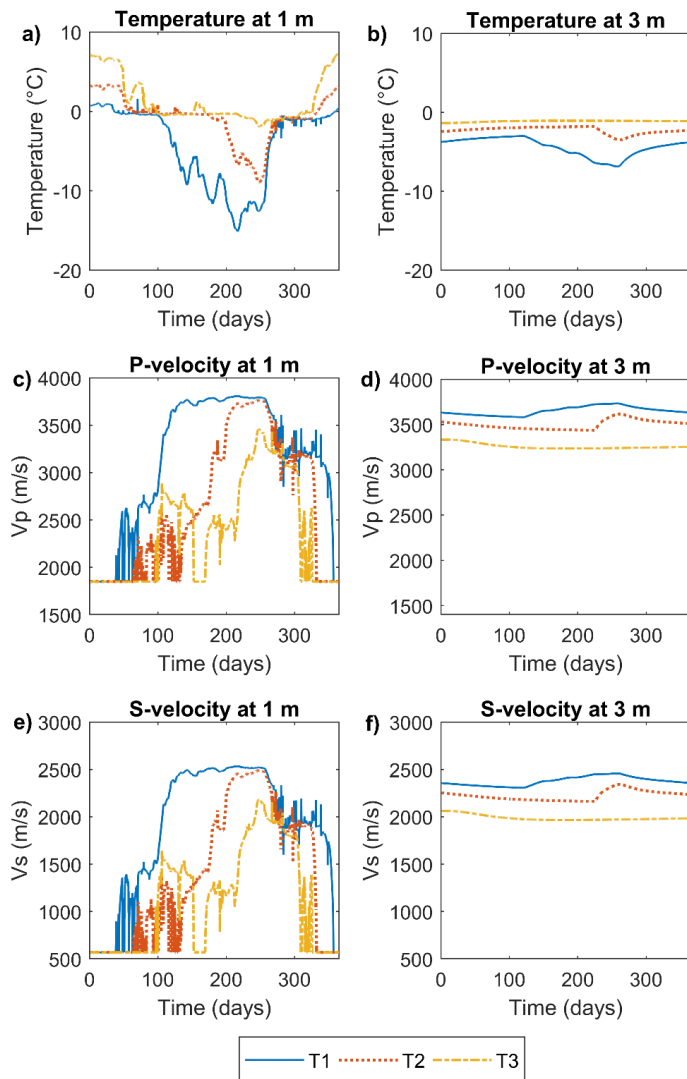


Figure 9: Variation in a)-b) temperature, c)-d) P-wave velocity, and e)-f) S-wave velocity with time for the fourth year in Figure 6a for T1 (today), T2 (RCP4.5), and T3 (RCP8.5) at 1.0 m depth (left column), and 3.0 m depth (right column). We assume constant matrix moduli and porosity with depth, and full saturation.

FIGURE 10

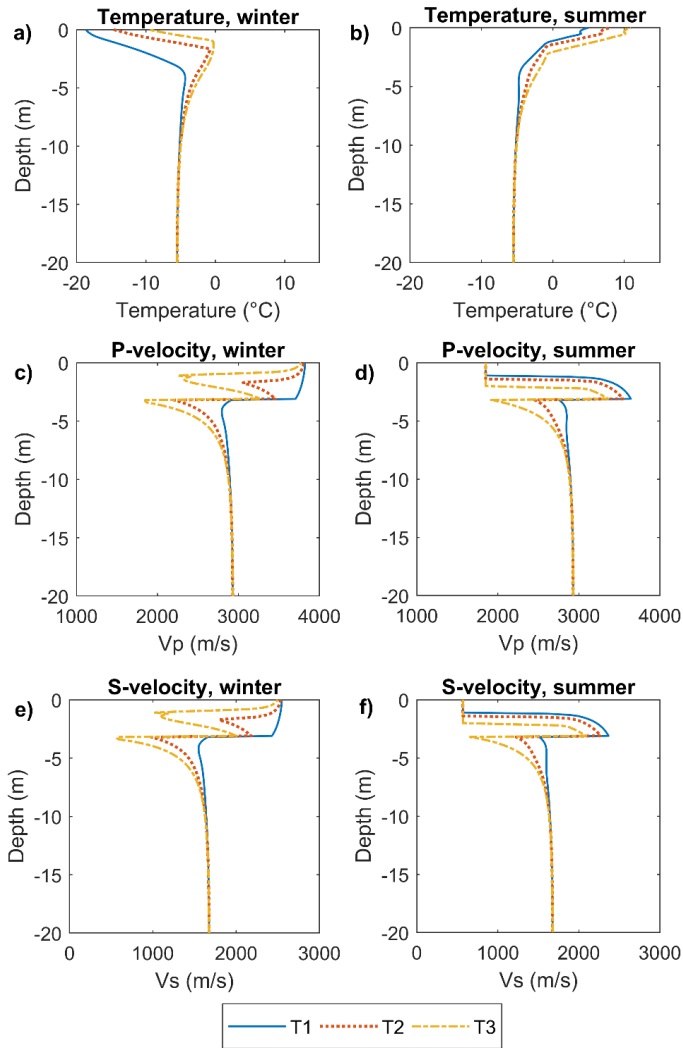


Figure 10: Variation in a)-b) temperature, c)-d) P-wave velocity, and e)-f) S-wave velocity with depth for T1 (today), T2 (RCP4.5), and T3 (RCP8.5) in February (left column), and August (right column) of the fourth year in Figure 6a. We assume constant matrix moduli and porosity with depth, and full saturation. The transition from 3 ppt salinity to 25 ppt salinity at 3.0 m depth has a large impact on the seismic velocities.

FIGURE 11

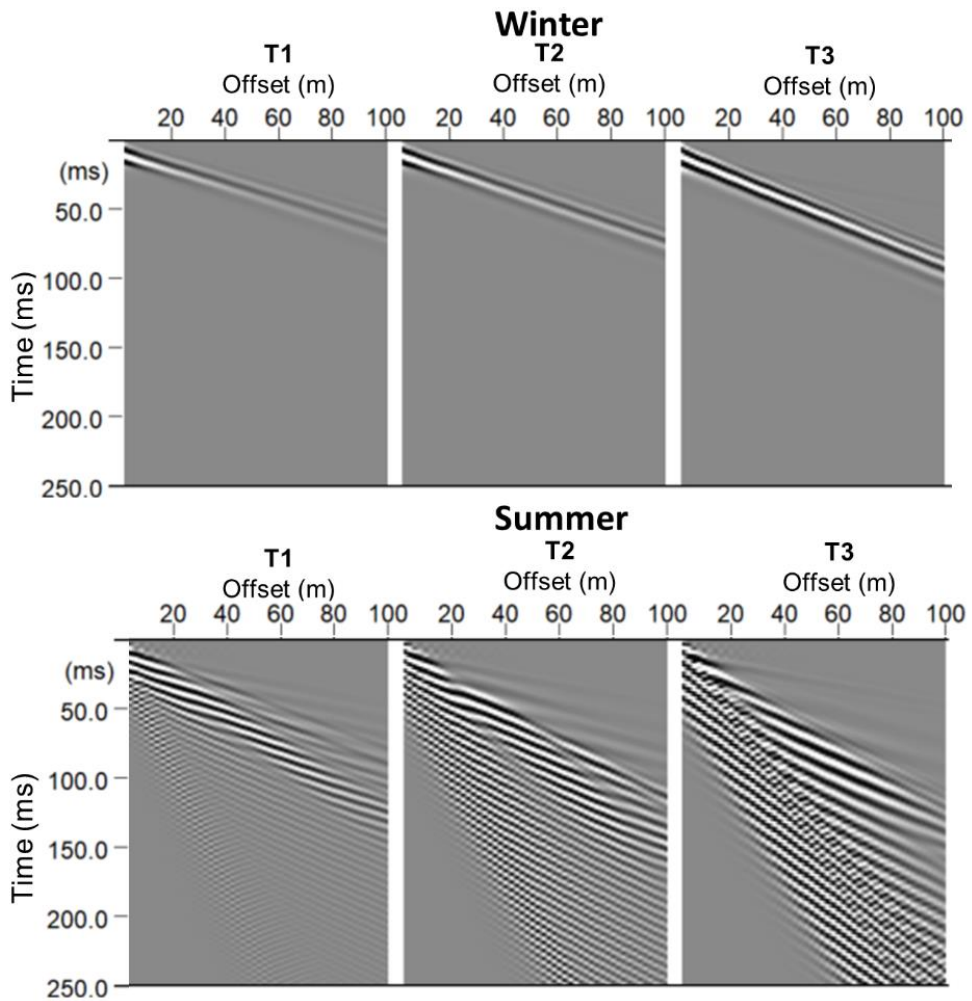


Figure 11: Synthetic seismograms created using OASES for scenarios T1 (today), T2 (RCP4.5), and T3 (RCP8.5) for the same calendar times as in Figure 10.

FIGURE 12

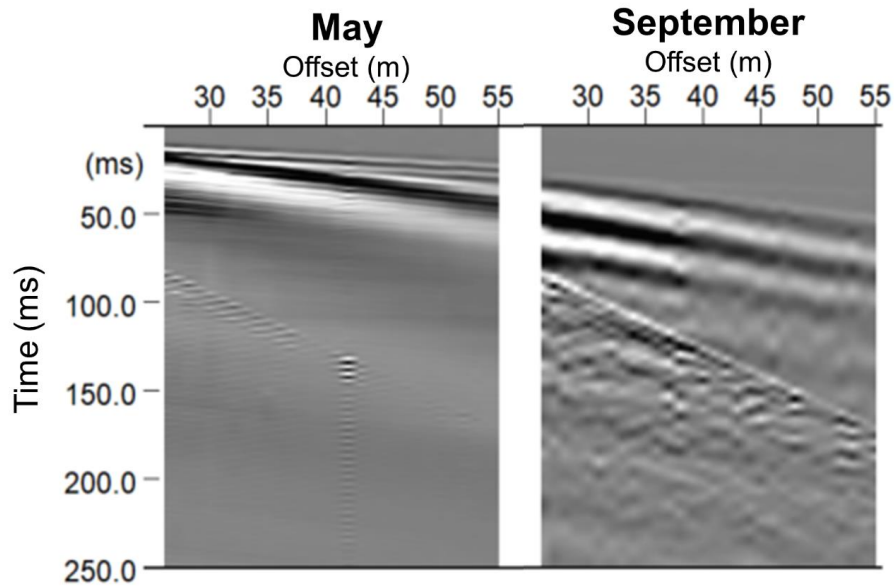


Figure 12: Unprocessed real seismic data recorded on vertical component geophones with one meter receiver interval in Adventdalen before (May) and after (September) summer thawing occurred. The seismic source was a sledgehammer at 25.0 m offset. The May data is displayed with a gain of 20 dB more than the September data. The linear event starting at approximately 80 ms in both gathers is the air wave traveling at 330 m/s.

FIGURE A-1

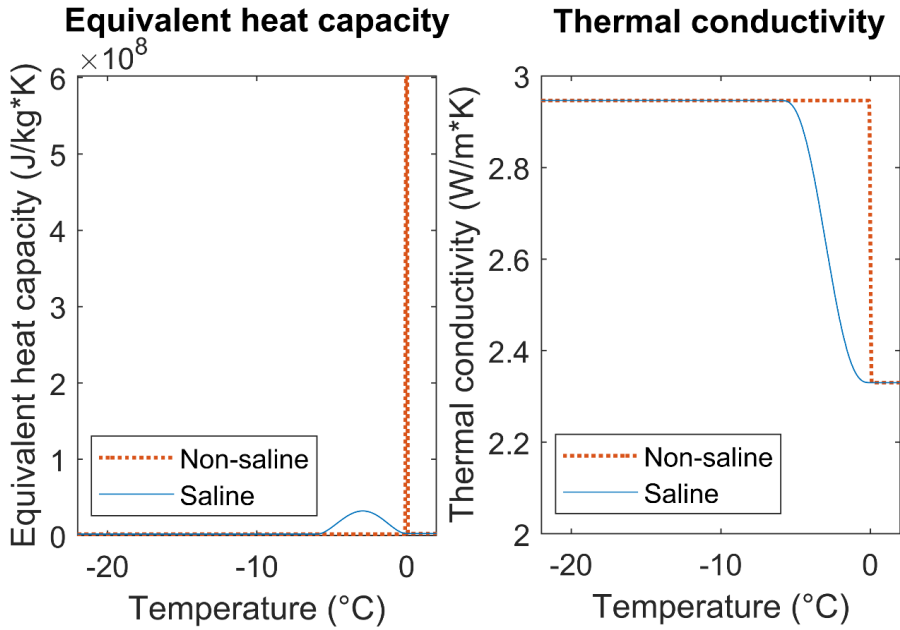


Figure A-1: The effect of increasing the salinity of the pore water in a pure quartz sandstone on equivalent heat capacity and thermal conductivity. The properties are modeled with equations 2 and 3, using the Heaviside function to represent the phase change. This not an accurate physical representation, but it is a decent approximation at modest subzero temperatures and low salinities.

FIGURE A-2

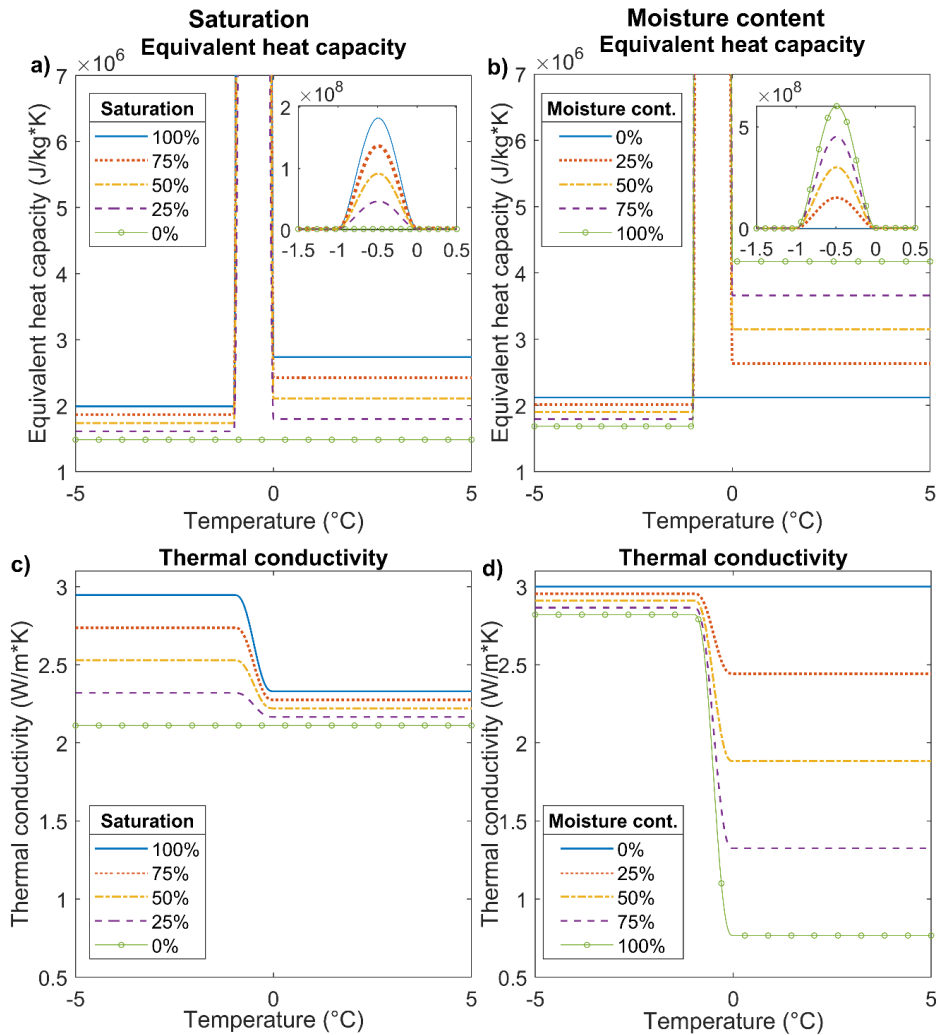


Figure A-2: The effect of changing model parameters of quartz sand on thermal properties, displayed for a phase change interval from -1°C to 0°C for clarity. a) Impact of saturation on equivalent heat capacity (30% porosity). Full extent in small window, detailed view in main window. Both windows have the same axes units. b) Impact of moisture content on equivalent heat capacity (full water saturation), c) impact of saturation on thermal conductivity (30% porosity), and d) impact of moisture content on thermal conductivity (full water saturation).

TABLE 1

Material	Heat capacity C [Jkg⁻¹K⁻¹]	Thermal conductivity κ [Wm⁻¹K⁻¹]	Density ρ (kgm⁻³)
Sand, quartz	830	3	2650
Silt, quartz	835	2.5	2650
Air	1005	0.025	1.225
Water	4185	0.54	997
Ice	1835	2.37	918

TABLE 2

Depth	Composition (depositional environment)	Salinity	Porosity
0.0–1.5 m	Quartz: 70% silt, 30% sand (eolian)	3 ppt	0.38
1.5–2.0 m	Quartz: 60% silt, 40% sand (eolian)	3 ppt	0.38
2.0–3.0 m	Quartz: 60% silt, 40% sand (eolian) or lenticular ice	3 ppt	0.38
3.0–8.0 m	Quartz: 50% silt, 50% sand (raised marine)	25 ppt	0.38
8.0–20.0 m	Quartz: 100% sand (raised marine)	25 ppt	0.38

TABLE 3

Parameter	Scenario
Top ground temperature	T1: Today T2: RCP4.5 T3: RCP8.5
Salinity	S1: From Table 2 S2: Zero salinity
Saturation	w1: 100% w2: 75% w3: 50% w4: 25% w5: 0%
Ground moisture content	m1: T1 without lenticular ice m2: T1 with pure ice at 2.0–3.0 m m3: T3 without lenticular ice m4: T3 with pure ice at 2.0–3.0 m

TABLE 4

State of unconsolidated sand	Rock physics model
(1) Dry	Hertz-Mindlin contact theory (Mindlin, 1949)
(2) Fully water-saturated	Gassmann equation (Gassmann, 1951) with result from (1) as the dry rock moduli
(3) Patchy water-saturated	Arithmetic average (Hill, 1963; Mavko et al., 2009) of results from (1) and (2)
(4) Fully ice-saturated	Self-consistent approach (Berryman, 1980a, b)
(5) Patchy ice-saturated	Arithmetic average (Hill, 1963; Mavko et al., 2009) of results from (1) and (4)

Paper 3

Published in *Applied Sciences*.

Paper 3: **Stemland, H. M.**, Johansen, T. A., & Ruud, B. O. (2020).
Potential Use of Time-Lapse Surface Seismics for Monitoring
Thawing of the Terrestrial Arctic. *Applied Sciences*, 10(5), 1875.


Published version reprinted. Published under Open Access license
CC BY 4.0. Copyright: The Authors 2020.

doi: <https://doi.org/10.3390/app10051875>



Article

Potential Use of Time-Lapse Surface Seismics for Monitoring Thawing of the Terrestrial Arctic

Helene Meling Stemland ^{1,2,*} , Tor Arne Johansen ^{1,2,3}  and Bent Ole Ruud ^{1,2} ¹ Department of Earth Science, University of Bergen, P.O. Box 7803, 5020 Bergen, Norway;

TorArne.johansen@uib.no (T.A.J.); bent.ruud@uib.no (B.O.R.)

² ARCEX, UiT The Arctic University of Norway, P.O. Box 6050 Langnes, 9037 Tromsø, Norway³ Department of Arctic Geology, The University Centre in Svalbard (UNIS), P.O. Box 156, 9171 Longyearbyen, Norway

* Correspondence: helene.stemland@uib.no

Received: 9 February 2020; Accepted: 5 March 2020; Published: 9 March 2020



Featured Application: We investigate the feasibility of using seismic data acquired in repeated active experiments for monitoring changes in the degree of freezing in unconsolidated sediments.

Abstract: The terrestrial Arctic is warming rapidly, causing changes in the degree of freezing of the upper sediments, which the mechanical properties of unconsolidated sediments strongly depend upon. This study investigates the potential of using time-lapse surface seismics to monitor thawing of currently (partly) frozen ground utilizing synthetic and real seismic data. First, we construct a simple geological model having an initial temperature of $-5\text{ }^{\circ}\text{C}$, and infer constant surface temperatures of $-5\text{ }^{\circ}\text{C}$, $+1\text{ }^{\circ}\text{C}$, $+5\text{ }^{\circ}\text{C}$, and $+10\text{ }^{\circ}\text{C}$ for four years to this model. The geological models inferred by the various thermal regimes are converted to seismic models using rock physics modeling and subsequently seismic modeling based on wavenumber integration. Real seismic data reflecting altered surface temperatures were acquired by repeated experiments in the Norwegian Arctic during early autumn to mid-winter. Comparison of the surface wave characteristics of both synthetic and real seismic data reveals time-lapse effects that are related to thawing caused by varying surface temperatures. In particular, the surface wave dispersion is sensitive to the degree of freezing in unconsolidated sediments. This demonstrates the potential of using surface seismics for Arctic climate monitoring, but inversion of dispersion curves and knowledge of the local near-surface geology is important for such studies to be conclusive.

Keywords: geophysics; permafrost; rayleigh wave; heat flux modeling; seismic modeling; rock physics modeling; seismic experiments; frozen ground; saline

1. Introduction

Adventdalen is located on Svalbard in the Norwegian Arctic, in an area that traditionally has experienced stable subzero winter temperatures and minimal annual rainfall. However, measurements in recent years show that climate is changing rapidly in this region and in the Arctic in general [1]. The IPCC [2] projects that temperatures and precipitation will continue to increase drastically in the years to come, likely contributing to thawing of currently frozen surfaces, including sea ice, glaciers, snow, and fully or partly frozen ground, often referred to as permafrost. Permafrost is defined as ground that stays at or below $0\text{ }^{\circ}\text{C}$ for at least two years [3], and this purely thermal definition implies that the degree of freezing in permafrost can vary considerably.

Methods for monitoring thawing of permafrost are desirable because thawing of currently frozen ground may have large geomorphic consequences [4]. Frozen ground is stiffer and more rigid than

unfrozen ground [5], therefore, subsidence and increased avalanche risk are likely consequences of thawing. Additionally, the large currently frozen land areas in the Northern hemisphere hold huge reserves of carbon that may be released to the atmosphere in the thawing process, inducing further climate change [6]. These methods should preferably be non-intrusive due to efficiency and environmental constraints.

Kneisel, et al. [7] provide an overview of some previously tested geophysical methods for monitoring thawing of permafrost, based on changes in electric, electromagnetic, elastic, or dielectric properties. All methods show limitations, particularly in areas with saline pore water, see [8] for a good overview. Salt causes freezing point depression and gradual freezing of pore water at subzero temperatures because the salinity of the residual pore water increases as salt is expelled when the water freezes [9]. Typical for saline permafrost is therefore unfrozen water within the permafrost, the amount depending on the salinity. If the salinity varies with depth, the amount of ice also varies with depth leading to an irregularly varying stiffness gradient with depth. For such partially frozen soils, the correlation between temperature and resistivity can be complicated [8,10], making electric methods difficult to use. Additionally, refraction seismics cannot be used in such environments, because it will not detect softer layers if these are located below stiffer layers.

Effective elastic properties of a medium depend on the physical properties and quantity of its constituents, as well as their geometrical distribution, which for permafrost typically means sediment grains, water, ice, and air. Thus, since thawing of a frozen material leads to a change in the ice-to-water ratio, referred to as the ice saturation, thawing will change the effective elastic and seismic properties. Laboratory measurements of the seismic properties of permafrost during the freeze-thaw process [8,11] support the idea that elastic properties of unconsolidated sediments decrease with increased thawing, however the relation between the degree of thawing and change in elastic properties is not linear.

Shear modulus of unconsolidated sediments is particularly affected by variation in ice saturation [12], and since surface wave properties strongly depend on the shear modulus, surface wave methods may be a viable option for detecting thawing in permafrost. Multichannel analysis of surface waves (MASW) was first introduced by Park, et al. [13], and has been extensively used for determining the properties of near-surface sediments through inversion of surface wave properties. However, MASW inversion shows limited success for soils with irregular stiffness gradients, and so more sophisticated methods are needed here. Several studies have focused on modified versions of MASW or other surface-wave methods to detect low velocity layers within permafrost with promising results [14,15], since the surface wave properties depend on how the elastic properties of the near-surface sediments vary with depth. For example, Tsuji, et al. [16] detected unfrozen sediments at the base of a glacier on Svalbard using common-midpoint cross-correlation followed by MASW. However, few have used surface wave methods to detect variations in permafrost with time, so-called time-lapse surface seismics. Ajo-Franklin, et al. [17] conducted a controlled warming experiment using distributed acoustic sensing to study the seismic response of such thawing, but we are not aware of any published studies focusing on variations in the seismic signatures of surface waves caused only by natural temperature variations.

The objective of this study is to evaluate the potential of using seismic data in general, and dispersion properties of surface waves in particular, to monitor temporal changes in the permafrost of the Arctic region caused by surface temperature variation. To study this, we make use of both synthetic seismic data generated by seismic modeling, and real time-lapse seismic data obtained by experiments in Adventdalen.

2. Materials and Methods

2.1. Modeling Thawing of Frozen Sediments

Heat transport in the subsurface occurs through conduction or convection, where conduction is commonly believed to be the dominant process in permafrost environments except for during extensive

spring thawing [18,19]. Heat is conducted downward into the ground if surface temperature is higher than ground temperature, and opposite. Surface temperature is primarily controlled by air temperature, therefore heat flux into the ground is typically largest during summer, but other factors such as snow cover and vegetation also affect surface temperature [3]. If the ground is initially frozen, which is common in the Arctic, this heat flux may cause thawing. In the Arctic today, winter temperatures are generally cold enough so that summer thawing is completely reversed during winter, but if Arctic temperatures increase as they are expected to do [2,20], we will likely see increased thawing of currently frozen ground in the near future.

By considering conduction only, we can describe the strength of the vertical heat flux by the heat transport equation:

$$C \frac{\partial T}{\partial t} + \nabla \cdot (-\kappa \nabla T) = Q. \tag{1}$$

Here, C ($\text{Jkg}^{-1}\text{K}^{-1}$) is the volumetric specific heat capacity (in the following referred to as heat capacity), T ($^{\circ}\text{C}$) is temperature at depth z (m), t is time, κ ($\text{Wm}^{-1}\text{K}^{-1}$) is thermal conductivity, and Q (Wm^{-2}) is external heat flux. The effective thermal properties of a composite depend on the thermal properties of the individual constituents and their volume fractions. For permafrost that is typically a matrix, water, ice, and air (in the following defined by subscripts m , w , i , and a , respectively). We also need to include latent heat L (kJ/kg) when one or more of the materials involved changes phase (here: water/ice, $L = 333.6$ kJ/kg), and following [21], we do this by replacing C with an equivalent heat capacity C_{eq} that includes latent heat:

$$C_{eq} = \theta_m \rho_m c_m + \theta_a \rho_a c_a + \theta_w \rho_w \left(c_w + \frac{\partial \Phi}{\partial T} L \right) + \theta_i \rho_i \left(c_i + \frac{\partial \Phi}{\partial T} L \right). \tag{2}$$

Density, heat capacity, and volume fraction of each constituent are defined by ρ_n , c_n , and θ_n , respectively, with subscripts as defined above. Total porosity is $\theta = \theta_a + \theta_w + \theta_i$, and the volume fractions of water and ice are given by $\theta_w = (\theta - \theta_a)\Phi$ and $\theta_i = (\theta - \theta_a) - \theta_w$, where Φ is a variable changing from 0 to 1 for fully frozen to fully unfrozen material over the phase change temperature interval. Note that saturation here denotes total fluid content in the pore space, i.e., $\frac{\theta_w + \theta_i}{\theta}$, while ice saturation denotes the amount of the fluid that is frozen, i.e., $\frac{\theta_i}{\theta_w + \theta_i}$. Furthermore, we parameterize thermal conductivity using the approximation of De Vries [22]:

$$\kappa_{eq} = \frac{f_m \theta_m \kappa_m + f_a \theta_a \kappa_a + f_w \theta_w \kappa_w + f_i \theta_i \kappa_i}{\theta_m f_m + \theta_a f_a + \theta_w f_w + \theta_i f_i}. \tag{3}$$

The shape factors f_n are given by [19] as:

$$f_n = \left[1 + \frac{1}{3} \left(\frac{\kappa_n}{\kappa_0} - 1 \right) \right]^{-1}, \tag{4}$$

where κ_0 denotes the thermal conductivity of the background medium (here: $\kappa_0 = \kappa_m$).

By assuming that the only heat source is the surface temperature ($Q = 0$), we can model how temperature distribution evolves with time and depth by using Equation (1) with thermal properties as given by Equations (2)–(4) in a finite-element scheme as provided by COMSOL [23].

Porosity, saturation, and salinity all affect thawing depth in frozen ground because the effective thermal properties of a composite are sensitive to the volume fractions of each constituent. Heat transport in Arctic terrestrial sediments is particularly sensitive to changes in the amount and chemistry of pore water because it may change phase in the temperature range commonly encountered here. In this paper, we assume full saturation and, therefore, porosity is the only factor determining water content. For a material to change phase from a solid to a liquid (e.g., ice to water), energy is absorbed to change the molecular structure of the material, meaning that heat transport to depth slows down. Non-saline water changes phase instantaneously at 0°C , while salinity leads to gradual phase change

and freezing point depression. Expressions were derived by [9] relating temperature to ice saturation, and using these expressions, we can estimate the ice saturation at a given temperature, assuming known salinity. Combining this knowledge with Equation (1), we can now determine how ice saturation evolves with time and depth.

Figure 1 shows the freezing point isotherm computed using Equation (1) for a simple model consisting of quartz sand with initial temperature $T_0 = -5\text{ }^\circ\text{C}$ throughout the sediment column for three different assumptions of surface temperature: T1 is $+1\text{ }^\circ\text{C}$, T2 is $+5\text{ }^\circ\text{C}$, and T3 is $+10\text{ }^\circ\text{C}$. We use typical values for the physical properties of the constituents from [21,24]. All three scenarios are displayed for a high-porosity (Figure 1a) and a low-porosity sand (Figure 1b) and for high-salinity (solid line) and low-salinity pore water (dashed line). It is evident from Figure 1 that higher surface temperature, increased salinity, and lower porosity all lead to increased thawing depth. This is because higher porosity means that a higher ice content needs to thaw for the thawing depth to progress deeper, and higher salinity means that phase change from ice to water is initiated at a lower temperature.

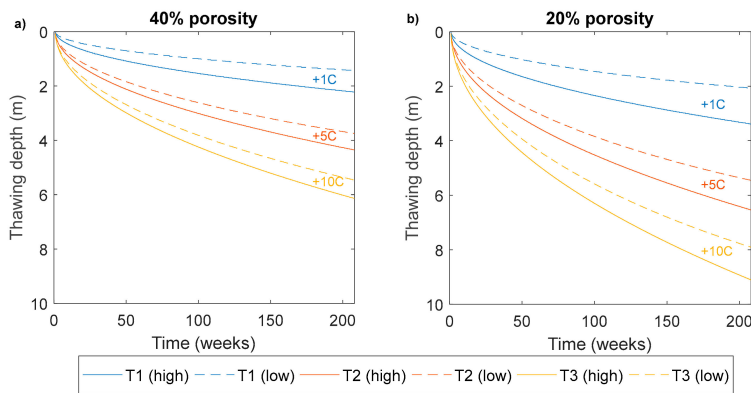


Figure 1. Freezing point isotherm throughout four years for (a) high porosity sand, and (b) low porosity sand. Both models are displayed for low salinity (dashed lines, freezing point temperature is $-0.17\text{ }^\circ\text{C}$) and high salinity (solid lines, freezing point temperature is $-1.43\text{ }^\circ\text{C}$) pore water, and for models T1 (top boundary temperature = $+1\text{ }^\circ\text{C}$), T2 (top boundary temperature = $+5\text{ }^\circ\text{C}$), and T3 (top boundary temperature = $+10\text{ }^\circ\text{C}$).

2.2. Modeling Effects of Thawing on Seismic Properties

To understand the effects of thawing and freezing on the elastic properties of unconsolidated, fully saturated near-surface sediments, we refer to papers of Dvorkin et al. [25–27] who described the effects of cement (here: ice) forming at various pore-scale configurations on the effective elastic properties of sediments. Ice can form at the grain contacts where it significantly increases the elastic properties, or within the pore space where the effect on effective properties is smaller. Since seismic experiments are dominated by low frequencies (usually $<200\text{ Hz}$), the relevant wavelengths are orders of magnitude larger than the heterogeneities of the sediments. To convert sediment composition and texture to elastic properties, we can adopt standard rock physics principles. In our case, we will consider isotropic sediments, which then elastically are fully characterized by the bulk modulus K and the shear modulus μ . We use a rock physics model similar to the two-end member mixing approach used by Minshull, et al. [28] and Dou, et al. [29] that inherently assumes cementing and pore-filling ice forming simultaneously at all ice saturations. We compute elastic properties of a fully unfrozen composite ($\theta_i = 0$) by first using Hertz–Mindlin contact theory [30] to compute dry rock properties, and subsequently Gassmann fluid substitution [31] to compute fully water-saturated rock properties. Furthermore, we compute elastic properties of a fully frozen composite ($\theta_f = 0$) using

the self-consistent approach (SCA) as described by [32,33] by assuming penny-shaped ice inclusions and spherical sediment grain inclusions in a background medium with initially unknown properties. Lastly, to find elastic properties of a composite with ice saturation varying from 0% to 100%, we use the Hill average of the modified Hashin–Shtrikman bounds to mix the fully unfrozen and the fully frozen end-members [34]. For completeness, the main procedure for computing elastic properties of thawing or freezing sediments is outlined in Appendix A.

The resulting elastic properties can together with density ρ be input to the equations for seismic P- and S-wave velocities V_p and V_s , respectively:

$$V_p = \sqrt{\left(K + \frac{4}{3}\mu\right)/\rho}, \tag{5}$$

and

$$V_s = \sqrt{\mu/\rho}. \tag{6}$$

Combining the resulting velocities with Equation (1), we can determine how seismic velocities vary with time and depth. The complete approach of combining heat flux modeling, rock physics modeling, and the equations for seismic velocities to investigate how seismic velocities vary with time is described in detail in [35].

Figure 2 shows the result of using this approach on high-porosity sand with high-salinity pore water, considering scenarios T1, T2, and T3 (solid lines in Figure 1a). The figure shows how velocities at two stationary points in the subsurface: 2 m depth (Figure 2b,c) and 10 m depth (Figure 2e,f), vary with time. The resulting velocity variations are consistent with the temperature variation with time at these two depths (Figure 2a,d): as temperatures increase, velocities decrease because the water content increases. The largest velocity change is at 2 m depth, consistent with the larger temperature change at 2 m depth than at 10 m depth because less heat is conducted down to 10 m depth.

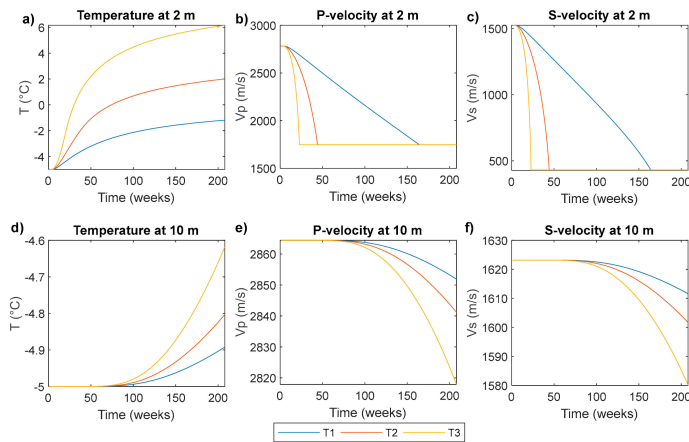


Figure 2. Variation in temperature and seismic velocities with time throughout four years at two stationary points for the models T1 (top boundary temperature = +1 °C), T2 (top boundary temperature = +5 °C), and T3 (top boundary temperature = +10 °C): (a) temperature at 2 m depth, (b) P-wave velocity at 2 m depth, (c) S-wave velocity at 2 m depth, (d) temperature at 10 m depth, (e) P-wave velocity at 10 m depth, (f) S-wave velocity at 10 m depth. Note the different axis scales for the two depths. The velocity decrease for all models is caused by the decreasing ice saturation due to temperature increase.

Figure 3 shows how temperature varies with depth at the last time step in Figure 2 for the scenarios T0, T1, and T3, for a 20 m thick model consisting of four layers. Each layer is quartz sand, but the porosity decreases with depth to mimic a compaction effect, as pressure increases with depth due to increased sediment load. A lower porosity means lesser effects of thawing on the elastic properties, because less material changes phase. For T1 and T3, the temperature distribution in the sediment column has significantly altered from the initial state, and the effects of this change are also evident in the corresponding seismic velocity profiles in Figure 3b,c. Since the only factor that varies between the models is the temperature, the large velocity change from T0 to T1 and T3 is solely ascribed to effects caused by the change in the thermal regime.

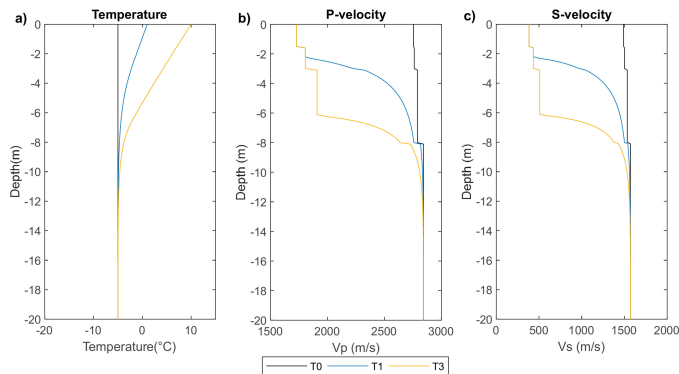


Figure 3. Variation in temperature and seismic velocities with depth for a specific point in time (after four years) for models T0 (initial model, $-5\text{ }^{\circ}\text{C}$ through the column), T1 (top boundary temperature = $+1\text{ }^{\circ}\text{C}$), and T3 (top boundary temperature = $+10\text{ }^{\circ}\text{C}$). (a) Temperature profiles, (b) P-wave velocity profiles, and (c) S-wave velocity profiles. Temperature is equal at all depths for T0, so the observed velocity variation with depth is only due to the porosity decrease: 40% in the upper layer, 35% in the second layer, 30% in the third layer, and 20% in the bottom layer.

2.3. Surface Seismic Analysis

Seismic data acquired in permafrost environments often show strong surface waves [12] and, therefore, we expect to observe these in both synthetic and real seismic data. Vertical geophones record surface waves of Rayleigh type. These propagate in the uppermost sediments of the subsurface as an interaction phenomenon between P- and S-waves. The phase velocity of a Rayleigh wave depends on the elastic properties of the medium that the wave travels in, which for a homogenous medium corresponds to the solution of the following equation [36]:

$$\zeta^3 - 8\zeta^2 + 8\zeta(3 - 2\eta) - 16(1 - \eta) = 0, \tag{7}$$

where $\zeta = \frac{c_R^2}{V_s^2}$ and $\eta = \frac{V_p^2}{V_s^2}$. c_R is phase velocity, and V_p and V_s are the P- and S- wave velocities defined by Equations (5) and (6).

There is no frequency dependence inherent in Equation (7), meaning that for a wave propagating in a homogenous medium, all frequency components of the surface wave travel with the same phase velocity c_R . However, when a wave propagates along the surface, the amplitude of higher frequencies decreases more rapidly with depth than the lower frequencies; thus, low frequency energy is generally dominating at larger depths. If the elastic properties of the subsurface vary with depth, the various frequency components are influenced by different effective elastic properties, and c_R becomes a function of depth and frequency. The equations describing surface wave propagation can then have several

solutions (i.e., possible combinations of frequencies and phase velocities), called modes, where the fundamental mode is the solution with the lowest phase velocity for a given frequency [37]. Since the Rayleigh wave is not inherently dispersive, any observed dispersion must be due to varying elastic properties of the near-surface sediments. Equation (7) infers that c_R depends on the sediment shear modulus through V_s , which has been shown to strongly respond to freezing/thawing. Thus, an inversion of frequency-dependent surface wave phase velocity for obtaining S-wave velocity with depth can reveal the degree of freezing with depth if the sediment composition is known [38].

To analyze surface wave dispersion, we generate frequency-phase velocity spectra (FV-spectra) by using a wavefield transform. This transform builds an FV-spectrum by decomposing the gather into separate frequency components through Fourier transformation, applying amplitude normalization to each component, and scanning for a range of phase velocities to find the magnitude of summed amplitudes for each frequency component [39]. The FV-spectrum is useful for separating body and surface wave energy, and when the surface wave phase velocity is constant for all frequencies, there is no variation in the elastic properties with depth. Correspondingly, if the FV-spectra of the surface wave vary between equal experiments conducted at different times, this implies a temporal variation of the elastic properties. In our case, this time-lapse effect represents a signal of altered freezing conditions.

3. Results

To investigate the impact of thawing on seismic data, we use seismic gathers and FV-spectra from synthetic seismic data and real seismic data acquired in the Norwegian Arctic.

3.1. Synthetic Seismic Data

We use an implementation of the wavenumber integration method called OASES [40] to generate synthetic seismic data corresponding to the velocity models shown in Figure 3. We model the vertical particle displacement for a 120 m-long line with geophones spaced 1 m apart and an impulsive source.

Figure 4a–c show synthetic seismic gathers corresponding to the velocity profiles for T0, T1, and T3 of Figure 3. We observe significant differences between the various gathers, and the complexity of the data increases as the temperature variability with depth increases. For T0, only two events are visible: a non-dispersive strong event travelling at approximately 1450 m/s, which is the fundamental mode of the surface wave (A), and one weaker non-dispersive event travelling at approximately 2700 m/s, which is the direct P-wave (B). The seismic gathers for T1 and T3 are more difficult to interpret, so in addition to the seismic gathers showed here, we make use of computed group velocities and modeling of separate modes of surface waves (as done in normal mode summation [41]). For T1, dispersive waves dominate the wavefield. This includes a wide fan-shaped event with group velocities ranging from approximately 200 m/s to 1450 m/s (C), which is associated with the fundamental mode of the surface wave, and a narrower fan-shaped event with group velocities ranging from approximately 500 m/s to 850 m/s (D), which is the first higher mode. Also for T3, dispersive events dominate the wavefield. The lower fan-shaped event (E) has group velocities ranging from approximately 200 m/s to 1450 m/s, and is the fundamental mode of the surface wave. Amplitudes are particularly high at a group velocity of approximately 380 m/s, which we attribute to the fundamental mode being dispersive at low frequencies, but becoming non-dispersive and correspondingly have a constant group velocity of 380 m/s at higher frequencies. The weaker fan-shaped event (F) is the first higher mode of surface wave with group velocities ranging from 380 m/s to 1000 m/s.

Figure 4d–f show the corresponding FV-spectra, with theoretical modal curves computed from the input models overlaid on the spectra for easier mode identification. Just as with the seismic gathers, there are significant differences between the various models. For T0, the peak in the FV-spectrum appears at fairly constant phase velocities of around 1450 m/s for all frequencies, corresponding with the non-dispersive event observed in Figure 4a. T1 and T3 have similar and constant phase velocities of about 380 m/s at frequencies >120 Hz, but at frequencies between approximately 63 and 120 Hz, phase velocities are higher for T1 than T3. By comparing the FV-spectra with the modal curves, the spectrum

peak for T0 corresponds well with the fundamental mode at all frequencies. For T1, it corresponds well with the fundamental mode below 31 Hz and above 63 Hz, and with the first higher mode from 31 to 63 Hz. We observe a weak fundamental mode between 31 and 63 Hz as well, but the first higher mode is dominant. For T3, the modal curves correspond well with the strong fundamental mode in most of the frequency range displayed here, while the first higher mode is dominant in a narrow frequency range of approximately 20 to 30 Hz. We also observe two weak higher modes starting at approximately 60 Hz and 110 Hz, respectively. At low frequencies for all models, we find energy at phase velocities higher than the S-wave velocity in the lower half space, which cannot be normal mode Rayleigh waves and, therefore, we interpret these as leaky wave modes.

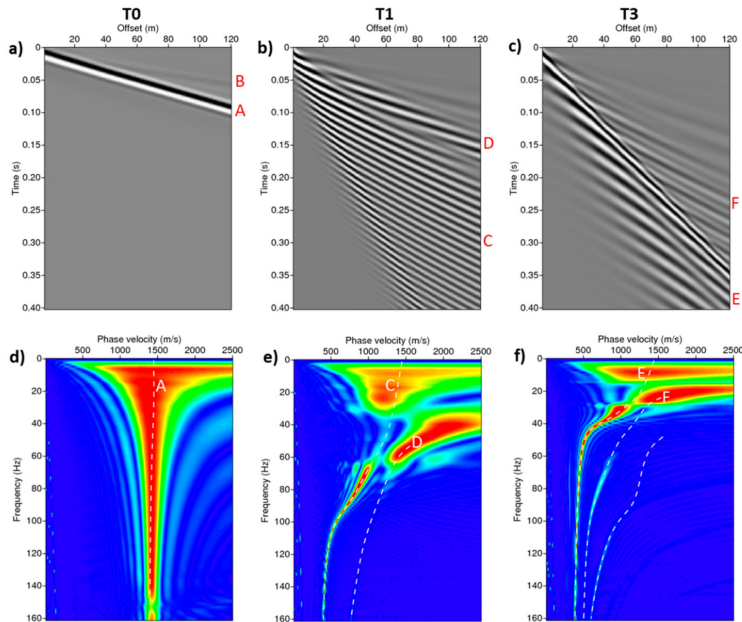


Figure 4. Top: synthetic seismic gathers for (a) model T0 (initial model, $-5\text{ }^{\circ}\text{C}$ through the column), (b) model T1 (top boundary temperature = $+1\text{ }^{\circ}\text{C}$), and (c) model T3 (top boundary temperature = $+10\text{ }^{\circ}\text{C}$). Bottom: corresponding frequency-phase velocity spectra (FV-spectra) with theoretical modal curves computed from the input models overlaid for (d) model T0, (e) model T1, and (f) model T3. The traces are plotted with an Ormsby-filter (1–25–40–120 Hz) to enhance the low frequencies and reduce aliasing. The capital letters A–F indicate the various modes of surface waves: A, C, and E is the fundamental mode, and D and F is the first higher mode.

3.2. Real Seismic Data Example

To further study the effects of thawing and freezing on the seismic wavefield, we conducted three similar seismic experiments on permafrost in Adventdalen on Svalbard in the Norwegian Arctic in October 2013, January 2014, and August 2014. Permafrost in this area typically extends to a depth of around 100 m, and the upper approximately 1.2 m is the active layer that thaws seasonally [1]. There are several boreholes in the area that indicate that the upper approximately 2–3 m of sediments in Adventdalen are eolian with a lower salinity than the deeper sediments of marine origin that extend down to the bedrock at approximately 65 m depth. However, these boreholes were drilled with the objective of obtaining information about the deeper bedrock, and thus lack detailed information about the near-surface soil properties, such as saturation, salinity, and porosity [42]. Gilbert, et al. [43] studied

several cores acquired throughout Adventdalen and showed that the near-surface geology is somewhat laterally homogenous in the area, but with some local variations. Temperature measurements from a borehole near the study site show that when the experiments were conducted in October, the surface temperature had been fluctuating around 0 °C for a couple of weeks. In January, surface temperature had been subzero since October (average surface temperature −9.81 °C), while in August, the surface temperature had been stable above zero since mid-May (average surface temperature 0.47 °C). From this, we presume that the ice saturation in the ground was highest in January and lowest in August. We also assume that the ice saturation was more laterally heterogeneous in October than during the other two experiments because the temperatures were close to the freezing point in the weeks prior to this experiment. The soil may also have varied laterally, but this should not affect the time-lapse effect observed in the data, since all three experiments were conducted at the same location.

The objective of the experiments was to acquire reflected, refracted, and surface waves, and we therefore used gimbaled geophone strings as seismic receivers in all experiments. Each geophone string consisted of 8 geophones spread out over an interval of 2.5 m, which was also the group interval. Geophone strings reduce the effect of the ground roll (Rayleigh wave), and the actual group length is critical for acquiring surface waves. The array response dampens the ground roll at wavelengths equal to or shorter than the group length, but this effect rapidly decreases for longer wavelengths (lower frequencies). Figure 5 shows that for the seismic setup applied here, we get half of the full response already at around 80 Hz (4 m wavelength) for the air wave traveling at 330 m/s, and the quality improves rapidly with decreasing frequency (increasing wavelength). Therefore, we limit our study to frequencies <100 Hz, where the surface waves should be minorly filtered due to the geophone group length.

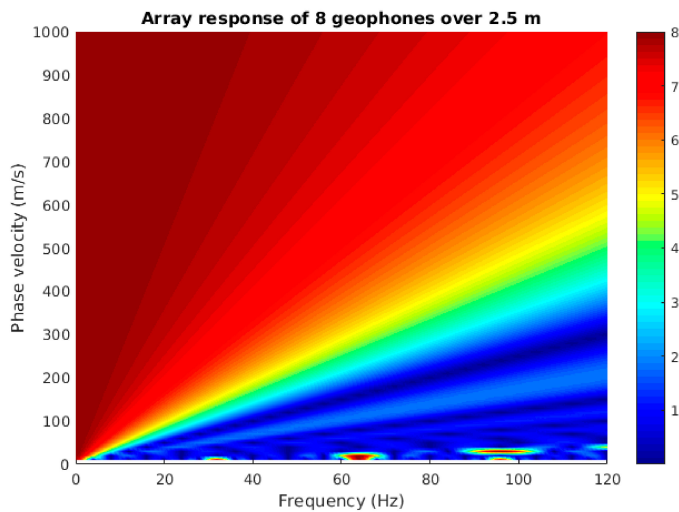


Figure 5. The array response of geophone strings with eight geophones where the length and group intervals are 2.5 m. The colors represent the gain of using the array relative to using a single geophone. Using geophone groups significantly downgrades the quality of the surface wave data at high frequencies, but affects in a minor way the amplitudes at low frequencies, except for at very low phase velocities.

The seismic source was firecrackers placed in a 0.2–0.3 m deep hole in the ground. These create an impulsive source signature. The receivers were placed along a 75 m long straight line, with the first receiver 9.5 m from the shot point. Figure 6 shows the location of the study site, and a picture of the

seismic spread in October 2013. As the picture and topographic map reveals, the ground below the seismic line was flat, and thus no topography effects were assumed.

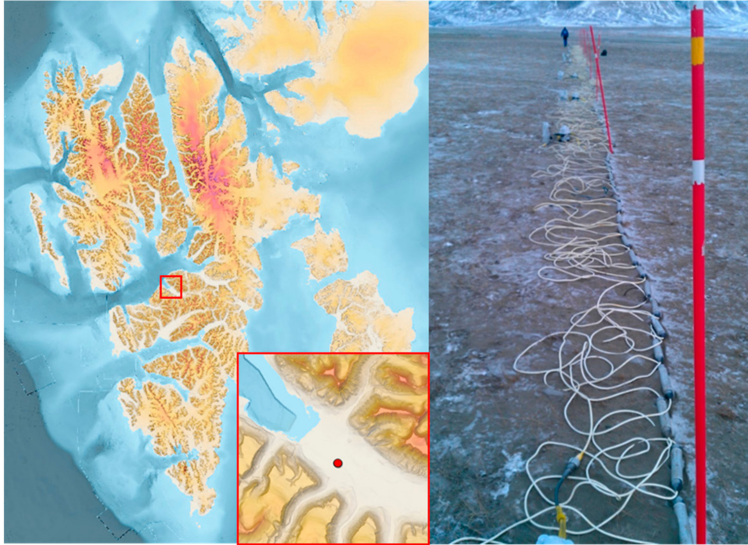


Figure 6. The location of the real seismic experiments in Adventdalen on Svalbard in the Norwegian Arctic is marked with a red dot in the small topographic map. The picture shows the study site in October 2013. Gimballed geophone strings are laid out with a 2.5 m group interval. Maps courtesy of Norwegian Polar Institute.

Since we lack information about the exact near-surface soil properties and the corresponding elastic properties at the study site, it is not possible to compute theoretical modal curves for these data. However, since we know that salinity is assumed to increase with depth in this area, this implies that the upper sediments freeze at a higher temperature than the deeper sediments due to the freezing point depression in saline pore water. When temperatures decrease gradually with depth, like in the synthetic example, a few possible scenarios are likely: the first is that during summer, we have an irregular velocity gradient in Adventdalen: a thawed upper low velocity layer above a largely frozen low-salinity and high velocity layer, above a less frozen high-salinity and lower velocity layer. A second possibility is that temperatures are high enough during summer so that the low-salinity layer completely thaws, which implies an increasing velocity gradient with depth: a thawed low-salinity and low velocity layer above a partly frozen high-salinity and higher velocity layer. This implies a similar velocity gradient as seen for the synthetic data example. During winter, it is likely that the uppermost low velocity layer disappears, i.e., velocity decreases with depth.

Figure 7a–c show seismic gathers obtained from the three seismic experiments. The data from January are clearly of different nature to the other two gathers, while the differences between the data from October and August are more subtle. A weak event (G) can be seen in all gathers. This is most likely a refraction or reflection from the underlying stiff, consolidated sediments at approximately 65 m depth. The ringing nature of this event seen in the gathers from October and August is probably due to related multiples. Event H in the January data is the Rayleigh wave caused by the frozen, stiff near-surface sediments. The air wave is defined by event I in all gathers. The lack of distinct Rayleigh waves in the data from October and August reveals that the surface sediments are soft. As noted by [44], there could be a strong coupling between the air wave and Rayleigh waves when the upper soil layer supports surface waves with a phase velocity identical to that of the air wave. This requires a soil layer

with an S-wave velocity less than 330 m/s at the surface and increasing with depth. The surface waves in the August and October data make a monochromatic wave train (J), which is further indicative of a group velocity lower than phase velocity. This is typical for Rayleigh waves when V_s is increasing with depth (i.e., phase velocity decreasing with increasing frequency).

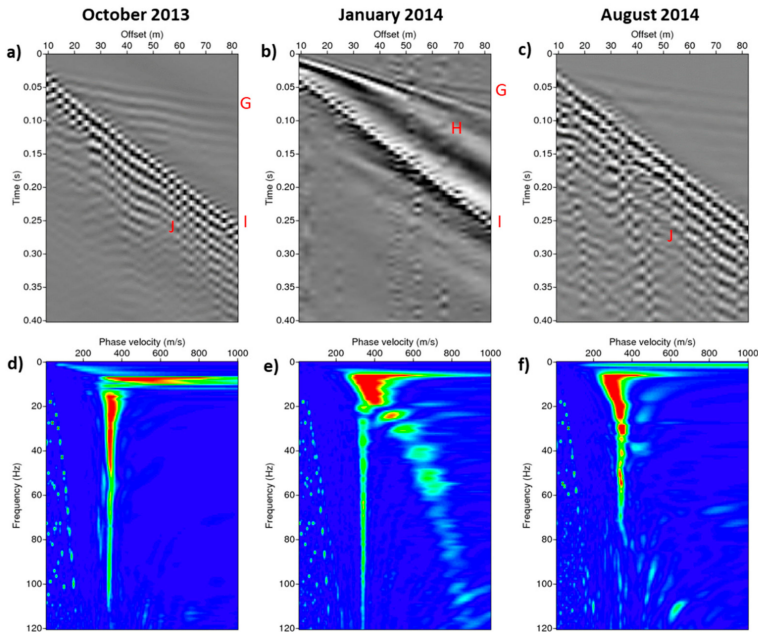


Figure 7. Top: seismic gathers acquired in Adventdalen in (a) October 2013, (b) January 2014, and (c) August 2014. Bottom: corresponding FV-spectra for (d) October 2013, (e) January 2014, and (f) August 2014. The capital letters G–J identify various wave modes.

Figure 7d–f show the corresponding FV-spectra for the three seismic experiments. The energy peak in all spectra is related to the air wave, with a velocity of about 330 m/s, but other events are also seen to vary between the different spectra. The most prominent events are observed in the data from January, where there are several strong amplitude events at increasing phase velocities with increasing frequency. This inversely dispersive trend is probably linked to several higher modes of surface waves, and they are absent in data from October and August. For the August data, some weak events seem to resemble those seen for the synthetic seismic models T1 and T3 at frequencies below 40 Hz. Thus, both the seismic gathers and the FV-spectra show changes in the freezing conditions between the experiments, specifically from January to October and August.

4. Discussion and Conclusions

Both the modeled and the real seismic data reveal that thawing has a significant impact on the seismic wavefield. Seismic properties depend on the ice saturation. Increased surface temperature causes increased heat flux, thawing, and lower seismic velocities of near-surface sediments. The largest change in seismic properties occurs at shallow depths when the surface temperature is high, because this implies the largest heat flux. Since Rayleigh waves are not inherently dispersive, surface wave dispersion means that the elastic properties alter with depth. Correspondingly, thawing or freezing will thus cause temporal changes in the FV-spectra.

In the synthetic seismic data, the fundamental mode of surface wave is dominant for all experiments. Since lower frequencies are more influenced by elastic properties of deeper sediments than higher frequencies, the fundamental mode in the FV-spectra reveals that the seismic velocities in the shallow layers decrease from the T0 to the T1 model and, furthermore, from the T1 to the T3 model. This is consistent with the input data. Since the velocity decrease extends to lower frequencies for T3 than for T1, T3 implies deeper thawing than T1 due to the reduced velocities with increased thawing.

The real seismic data are, as expected, quite different from the modeled seismic data, since the subsurface model used for the synthetic data was not designed to represent local conditions. Since the inversely dispersive trend in the FV-spectra is the strongest in January, weaker in October, and missing in August, this indicates that the presence of higher modes is related to ice saturation. Temperature data indicate that the upper sediments are most frozen in January when the higher modes are strong, and least frozen in August, when the higher modes are absent. Surface waves are generally attenuated more in unfrozen ground than in frozen ground, which also explains why more low-frequency surface waves are seen in the data from January.

We did not consider a varying salinity in the synthetic data example, meaning that seismic velocities here increase steadily with depth. At the study site of the real seismic data, the ground salinity most probably varies with depth, which implies that several velocity depth models are possible. During winter, a stiff upper layer overlies softer sediments, and in this case, strong higher modes are typically generated [14,45–47]. This also happens when a low velocity layer is embedded in layers of higher velocities. An analogue to a stiff frozen layer on top of a stack of softer unconsolidated sediments is pavement, which constitutes a thin, very stiff layer overlaying softer sediments. For such velocity depth models, higher order modes of Rayleigh waves have been observed as an inversely dispersive trend in FV-spectra, as well as a large amount of leaky guided waves [48], which are also seen in our synthetic data. During summer, we either have stiffer sediments embedded in softer sediments, or stiffness increasing with depth. For such velocity depth models, higher modes are rarely seen [14,45]. This supports our observation that the fundamental mode is more dominant in October and August, and higher modes are more dominant in January when the uppermost layer is frozen.

Differences in the signatures of the modeled and real seismic data can also be caused by the fact that unlike in the synthetic model, the surface temperature varied frequently between low and high temperatures in the time period between October 2013 and August 2014. Furthermore, variable precipitation throughout the year affects the data. While snow leads to effective insulation of the heat flux, rain alters the moisture content in the uppermost sediments. We also assume a simple horizontally layered geological model, and no lateral soil heterogeneity or anisotropy. Adding complexity to the geological model will certainly affect the seismic data, but will to a lesser degree affect the time-lapse effects in data collected at the same location. The seismic experiments in Adventdalen also included a second seismic data line with the same shot point, but having a 67.5 degree azimuth to the east of the current line. These data display similar FV-spectra and time-lapse effects, indicating gentle variation in the soil properties laterally. The seismic setup of the experiments was not particularly designed for recording surface waves. As full thawing only occurs in the top meter or so in Adventdalen, the receiver interval should in general be minimized to gain more high-frequency data. Although geophone strings were used, the array response retains frequencies up to 100 Hz, which is sufficient for our study.

Our results show significant time-lapse effects in both the seismic gathers and the estimated Rayleigh wave dispersion curves, which can be related to thawing of near-surface Arctic sediments. The synthetic seismic data were made with full control over the physical properties of the models, and show distinct time-lapse effects that are due to changes in the thermal regime. The time-lapse study of the real seismic data strongly indicate that low-frequency time-lapse effect are due to changes in the freezing conditions. Analysis of FV-spectra basically provide trends in the stiffness gradient (increasing/decreasing/irregular). However, to quantify exact changes in the mechanical properties of the subsurface due to thawing requires more sophisticated inversion of FV-spectra to S-wave

velocity with depth. Conventional inversion techniques using normal mode methods are not designed for (irregularly) decreasing velocities with depth, or when higher-order modes dominate [45,49,50]. This was seen to occur for the real seismic data example, where higher modes became dominant with increasing frequencies. Full-waveform inversion often works for small modal jumps, but fails for large modal jumps, and where the main energy does not return to the fundamental mode at high frequencies [14,45]. An in-depth discussion or execution of more complex inversion methods is beyond the scope of this study. Our study has been limited to qualitatively assessing the differences between the various seismic gathers and FV-spectra at low frequencies. Our results also highlight the need to know the near-surface soil and pore water properties to estimate the degree of thawing from estimated velocity profiles. The contribution of this study is to demonstrate the potential of using time-lapse surface seismic data in climate monitoring of the terrestrial Arctic.

Author Contributions: Conceptualization, H.M.S. and T.A.J.; Data curation, H.M.S., T.A.J. and B.O.R.; Formal analysis, H.M.S. and B.O.R.; Funding acquisition, T.A.J.; Investigation, H.M.S., T.A.J. and B.O.R.; Methodology, H.M.S., T.A.J. and B.O.R.; Project administration, T.A.J.; Software, H.M.S. and B.O.R.; Supervision, T.A.J.; Validation, H.M.S., T.A.J. and B.O.R.; Visualization, H.M.S. and B.O.R.; Writing—original draft, H.M.S.; Writing—review and editing, H.M.S., T.A.J. and B.O.R. All authors have read and agreed to the published version of the manuscript.

Funding: This research is funded by ARCEX partners and the Research Council of Norway (grant number 228107).

Conflicts of Interest: The authors declare no conflict of interest. The funders had no role in the design of the study; in the collection, analyses, or interpretation of data; in the writing of the manuscript, or in the decision to publish the results.

Appendix A

Hertz–Mindlin contact theory (CT):

Hertz–Mindlin contact theory can be used to compute effective dry rock moduli:

$$k_{CT} = \left(\frac{n^2(1 - \varphi_0)^2 \mu_G^2}{18\pi^2(1 - \nu_G)^2} P \right)^{\frac{1}{3}}, \tag{A1}$$

and:

$$\mu_{CT} = \frac{5 - 4\nu_G}{5(2 - \nu_G)} \left(\frac{3n^2(1 - \varphi_0)^2 \mu_G^2}{2\pi^2(1 - \nu_G)^2} P \right)^{\frac{1}{3}}. \tag{A2}$$

The subscript CT means the effective dry rock moduli and the subscript G means the sediment grain property. k and μ are the bulk and shear modulus, respectively, ν is the Poisson’s ratio, φ_0 is the porosity, P is the pressure, and n is the coordination number.

Gassmann fluid substitution (Gassmann, 1951):

Gassmann fluid substitution can be used to compute the effective water-saturated rock properties for a case where the wavelengths \gg characteristic pore sizes:

$$k_{satW} = k_G \frac{\varphi_0 k_{CT} - (1 + \varphi_0) k_W k_{CT} / k_G + k_W}{(1 - \varphi_0) k_W + \varphi_0 k_G - k_W k_{CT} / k_G}. \tag{A3}$$

The subscript satW means the effective fully water-saturated moduli, and the subscript W means water. The shear modulus is unaffected by the presence of a fluid, so:

$$\mu_{satW} = \mu_{CT}. \tag{A4}$$

Self-consistent approach (SCA) (Berryman (1980a,b)):

The self-consistent approach (SCA) can be used to compute the effective ice-saturated rock properties. The principle of the SCA is to assume inclusions of the constituents in a background medium with initially unknown properties. The strategy is to adjust the elastic properties of the

background medium iteratively until the net scattering from a wave incident on the background medium with inclusions is zero. Here, this means setting up two scenarios, $j = 1, 2$. Scenario 1 is for penny-shaped ice inclusions in a background medium, and scenario 2 is for spherical sediment grain inclusions in a background medium. We compute the elastic moduli k_j and μ_j for each scenario as a function of ice-filled rock effective moduli k_{satl} and μ_{satl} by using formulas:

$$k_1 = (k_i - k_{satl})S_i P_i, \tag{A5}$$

$$\mu_1 = (\mu_i - \mu_{satl})S_i Q_i, \tag{A6}$$

$$k_2 = (k_g - k_{satl})S_g P_g, \tag{A7}$$

$$\mu_2 = (\mu_g - \mu_{satl})S_g Q_g. \tag{A8}$$

S_j and S_g are the fractions of each inclusion type, and we use shape-dependent factors P_i, P_g, Q_i and Q_g as found in Dou et al. (2017):

$$P_i = \frac{k_{satl} + \frac{4}{3}\mu_i}{k_i + \frac{4}{3}\mu_i + \pi\alpha_i\beta^*}, \tag{A9}$$

$$Q_i = \frac{1}{5} \left(1 + \frac{8\mu_{satl}}{4\mu_i + \pi\alpha_i(\mu^* + 2\beta^*)} + 2 \frac{k_i + \frac{2}{3}(\mu_i + \mu_{satl})}{k_i + \frac{4}{3}\mu_i + \pi\alpha_i\beta^*} \right), \tag{A10}$$

$$P_g = \frac{k_{satl} + \frac{4}{3}\mu_{satl}}{k_g + \frac{4}{3}\mu_{satl}}, \tag{A11}$$

$$Q_g = \frac{\mu_{satl} + St^*}{\mu_g + St^*}, \tag{A12}$$

where α_i is the aspect ratio of the grains, and β^* and St^* are defined by:

$$\beta^* = \mu_{satl} \frac{3k_{satl} + \mu_{satl}}{3k_{satl} + 4\mu_{satl}}, \tag{A13}$$

$$St^* = \frac{\mu_{satl}}{6} \left(\frac{9k_{satl} + 8\mu_{satl}}{k_{satl} + 2\mu_{satl}} \right). \tag{A14}$$

We require $k_1 + k_2 = 0$ and $\mu_1 + \mu_2 = 0$, and solve these equations iteratively for k_{satl} and μ_{satl} , which are the ice-filled rock effective elastic moduli.

Modified Hashin–Shtrikman bounds (Hashin and Shtrikman, 1963; Dou et al., 2017):

Hashin–Shtrikman bounds were originally developed to mix two mineral phases. To use Hashin–Shtrikman bounds to mix to fully frozen and fully unfrozen multi-phase composites for estimating elastic properties at varying ice saturations, we replace the volume fraction of each material in the original formulas with the amount of water or ice in the pore space, respectively s_w or s_i ($s_w + s_i = 1$ for fully saturated pore space).

Hashin–Shtrikman bounds are upper and lower bounds for elastic moduli: $k_{HS+}, k_{HS-}, \mu_{HS+}$, and μ_{HS-} . The effective properties k_{PF} and μ_{PF} at any given saturation are simplified as the arithmetic average (Hill average) of these two bounds. The subscript PF means partially frozen.

$$k_{PF} = \frac{1}{2}(k_{HS+} + k_{HS-}), \tag{A15}$$

$$\mu_{PF} = \frac{1}{2}(\mu_{HS+} + \mu_{HS-}), \tag{A16}$$

where

$$k_{HS+} = k_{satI} + \frac{s_w}{(k_{satW} - k_{satI})^{-1} + s_i \left(k_{satI} + \frac{4}{3} \mu_{satI} \right)^{-1}}, \quad (\text{A17})$$

$$k_{HS-} = k_{satW} + \frac{s_i}{(k_{satI} - k_{satW})^{-1} + s_w \left(k_{satW} + \frac{4}{3} \mu_{satW} \right)^{-1}}, \quad (\text{A18})$$

$$\mu_{HS+} = \mu_{satI} + \frac{s_w}{(\mu_{satW} - \mu_{satI})^{-1} + 2s_i \frac{k_{satI} + 2\mu_{satI}}{5\mu_{satI} \left(k_{satI} + \frac{4}{3} \mu_{satI} \right)}}, \quad (\text{A19})$$

$$\mu_{HS-} = \mu_{satW} + \frac{s_i}{(\mu_{satI} - \mu_{satW})^{-1} + 2s_w \frac{k_{satW} + 2\mu_{satW}}{5\mu_{satW} \left(k_{satW} + \frac{4}{3} \mu_{satW} \right)}}. \quad (\text{A20})$$

References

- Christiansen, H.H.; Etzelmüller, B.; Isaksen, K.; Juliussen, H.; Farbrot, H.; Humlum, O.; Johansson, M.; Ingeman-Nielsen, T.; Kristensen, L.; Hjort, J. The thermal state of permafrost in the Nordic area during the International Polar Year 2007–2009. *Permafr. Periglac. Process.* **2010**, *21*, 156–181. [[CrossRef](#)]
- Pachauri, R.K.; Allen, M.R.; Barros, V.R.; Broome, J.; Cramer, W.; Christ, R.; Church, J.A.; Clarke, L.; Dahe, Q.; Dasgupta, P. *Climate Change 2014: Synthesis Report. Contribution of Working Groups I, II and III to the Fifth Assessment Report of the Intergovernmental Panel on Climate Change*; 9291691437; IPCC: Geneva, Switzerland, 2014.
- French, H.M. *The Periglacial Environment*, 5th ed.; John Wiley & Sons: West Sussex, UK, 2017.
- Hjort, J.; Karjalainen, O.; Aalto, J.; Westermann, S.; Romanovsky, V.E.; Nelson, F.E.; Etzelmüller, B.; Luoto, M. Degrading permafrost puts Arctic infrastructure at risk by mid-century. *Nat. Commun.* **2018**, *9*, 5147. [[CrossRef](#)] [[PubMed](#)]
- Zimmerman, R.W.; King, M.S. The effect of the extent of freezing on seismic velocities in unconsolidated permafrost. *Geophysics* **1986**, *51*, 1285–1290. [[CrossRef](#)]
- Schaefer, K.; Zhang, T.; Bruhwiler, L.; Barrett, A.P. Amount and timing of permafrost carbon release in response to climate warming. *Tellus B Chem. Phys. Meteorol.* **2011**, *63*, 168–180. [[CrossRef](#)]
- Kneisel, C.; Hauck, C.; Fortier, R.; Moorman, B. Advances in geophysical methods for permafrost investigations. *Permafr. Periglac. Process.* **2008**, *19*, 157–178. [[CrossRef](#)]
- Wu, Y.; Nakagawa, S.; Kneafsey, T.J.; Dafflon, B.; Hubbard, S. Electrical and seismic response of saline permafrost soil during freeze–thaw transition. *J. Appl. Geophys.* **2017**, *146*, 16–26. [[CrossRef](#)]
- Potter, R.W.; Clyne, M.A.; Brown, D.L. Freezing point depression of aqueous sodium chloride solutions. *Econ. Geol.* **1978**, *73*, 284–285. [[CrossRef](#)]
- Wu, Y.; Hubbard, S.S.; Ulrich, C.; Wulschleger, S.D. Remote monitoring of freeze–thaw transitions in Arctic soils using the complex resistivity method. *Vadose Zone J.* **2012**, *12*, vzi2012.0062. [[CrossRef](#)]
- Dou, S.; Nakagawa, S.; Dreger, D.; Ajo-Franklin, J. A rock-physics investigation of unconsolidated saline permafrost: P-wave properties from laboratory ultrasonic measurements. *Geophysics* **2016**, *81*, WA233–WA245. [[CrossRef](#)]
- Johansen, T.A.; Digranes, P.; van Schaack, M.; Lønne, I. Seismic mapping and modeling of near-surface sediments in polar areas. *Geophysics* **2003**, *68*, 566–573. [[CrossRef](#)]
- Park, C.B.; Miller, R.D.; Xia, J. Multichannel analysis of surface waves. *Geophysics* **1999**, *64*, 800–808. [[CrossRef](#)]
- Dou, S.; Ajo-Franklin, J.B. Full-wavefield inversion of surface waves for mapping embedded low-velocity zones in permafrost. *Geophysics* **2014**, *79*, EN107–EN124. [[CrossRef](#)]
- Strobbia, C.; Glushchenko, A.; Laake, A.; Vermeer, P.; Papworth, T.; Ji, Y. Arctic near surface challenges: The point receiver solution to coherent noise and statics. *First Break* **2009**, *27*, 69–76.
- Tsuji, T.; Johansen, T.A.; Ruud, B.O.; Ikeda, T.; Matsuoka, T. Surface-wave analysis for identifying unfrozen zones in subglacial sediments. *Geophysics* **2012**, *77*, EN17–EN27. [[CrossRef](#)]
- Ajo-Franklin, J.; Dou, S.; Daley, T.; Freifeld, B.; Robertson, M.; Ulrich, C.; Wood, T.; Eckblaw, I.; Lindsey, N.; Martin, E. Time-lapse surface wave monitoring of permafrost thaw using distributed acoustic sensing and a permanent automated seismic source. In *SEG Technical Program Expanded Abstracts 2017*; Society of Exploration Geophysicists: Tulsa, OK, USA, 2017; pp. 5223–5227.

18. Romanovsky, V.E.; Osterkamp, T.E. Effects of unfrozen water on heat and mass transport processes in the active layer and permafrost. *Permafrost. Periglac. Process.* **2000**, *11*, 219–239. [[CrossRef](#)]
19. Weismüller, J.; Wollschläger, U.; Boike, J.; Pan, X.; Yu, Q.; Roth, K. Modeling the thermal dynamics of the active layer at two contrasting permafrost sites on Svalbard and on the Tibetan Plateau. *Cryosphere* **2011**, *5*, 741–757. [[CrossRef](#)]
20. Seneviratne, S.I.; Donat, M.G.; Pitman, A.J.; Knutti, R.; Wilby, R.L. Allowable CO₂ emissions based on regional and impact-related climate targets. *Nature* **2016**, *529*, 477. [[CrossRef](#)]
21. Govaerts, J.; Beerten, K.; Veen, J.T. Weichselian permafrost depth in the Netherlands: A comprehensive uncertainty and sensitivity analysis. *Cryosphere* **2016**, *10*, 2907–2922. [[CrossRef](#)]
22. De Vries, D.A. Thermal properties of soils. In *Physics of Plant Environment*; North-Holland Publishing Corporation: Amsterdam, The Netherlands, 1963; pp. 210–235.
23. Pryor, R.W. *Multiphysics Modeling Using COMSOL®: A First Principles Approach*, 1st ed.; Jones & Bartlett Publishers: Sudbury, MA, USA, 2009.
24. Mavko, G.; Mukerji, T.; Dvorkin, J. *The Rock Physics Handbook*, 2nd ed.; Cambridge University Press: New York, NY, USA, 2009.
25. Dvorkin, J.; Nur, A. Elasticity of high-porosity sandstones: Theory for two North Sea data sets. *Geophysics* **1996**, *61*, 1363–1370. [[CrossRef](#)]
26. Dvorkin, J.; Nur, A.; Yin, H. Effective properties of cemented granular materials. *Mech. Mater.* **1994**, *18*, 351–366. [[CrossRef](#)]
27. Dvorkin, J.; Berryman, J.; Nur, A. Elastic moduli of cemented sphere packs. *Mech. Mater.* **1999**, *31*, 461–469. [[CrossRef](#)]
28. Minshull, T.; Singh, S.; Westbrook, G. Seismic velocity structure at a gas hydrate reflector, offshore western Colombia, from full waveform inversion. *J. Geophys. Res. Solid Earth* **1994**, *99*, 4715–4734. [[CrossRef](#)]
29. Dou, S.; Nakagawa, S.; Dreger, D.; Ajo-Franklin, J. An effective-medium model for P-wave velocities of saturated, unconsolidated saline permafrost. *Geophysics* **2017**, *82*, EN33–EN50. [[CrossRef](#)]
30. Mindlin, R. Compliance of elastic bodies in contact. *J. Appl. Mech. ASME* **1949**, *16*, 259–268.
31. Gassmann, F. Elastic waves through a packing of spheres. *Geophysics* **1951**, *16*, 673–685. [[CrossRef](#)]
32. Berryman, J.G. Long-wavelength propagation in composite elastic media II: Ellipsoidal inclusions. *J. Acoust. Soc. Am.* **1980**, *68*, 1820–1831. [[CrossRef](#)]
33. Berryman, J.G. Long-wavelength propagation in composite elastic media I: Spherical inclusions. *J. Acoust. Soc. Am.* **1980**, *68*, 1809–1819. [[CrossRef](#)]
34. Hashin, Z.; Shtrikman, S. A variational approach to the theory of the elastic behaviour of multiphase materials. *J. Mech. Phys. Solids* **1963**, *11*, 127–140. [[CrossRef](#)]
35. Stemland, H.M.; Johansen, T.A.; Ruud, B.O.; Mavko, G. Elastic properties as indicators of heat flux into cold near-surface arctic sediments. *Geophysics*. under review.
36. Landau, L.D.; Kosevich, A.; Pitaevskii, L.P.; Lifshitz, E.M. *Theory of Elasticity*, 3rd ed.; Butterworth-Heinemann: Oxford, UK, 2012.
37. Zhang, S.X.; Chan, L.S.; Chen, C.Y.; Dai, F.C.; Shen, X.K.; Zhong, H. Apparent phase velocities and fundamental-mode phase velocities of Rayleigh waves. *Soil Dyn. Earthq. Eng.* **2003**, *23*, 563–569. [[CrossRef](#)]
38. Pan, Y.; Xia, J.; Gao, L.; Shen, C.; Zeng, C. Calculation of Rayleigh-wave phase velocities due to models with a high-velocity surface layer. *J. Appl. Geophys.* **2013**, *96*, 1–6. [[CrossRef](#)]
39. Park, C.B.; Miller, R.D.; Xia, J. Imaging dispersion curves of surface waves on multi-channel record. In *SEG Technical Program Expanded Abstracts 1998*; Society of Exploration Geophysicists: Tulsa, OK, USA, 1998; pp. 1377–1380.
40. Schmidt, H.; Jensen, F.B. A full wave solution for propagation in multilayered viscoelastic media with application to Gaussian beam reflection at fluid–solid interfaces. *J. Acoust. Soc. Am.* **1985**, *77*, 813–825. [[CrossRef](#)]
41. Herrmann, R.B. Computer programs in seismology: An evolving tool for instruction and research. *Seismol. Res. Lett.* **2013**, *84*, 1081–1088. [[CrossRef](#)]
42. Braathen, A.; Bælum, K.; Christiansen, H.H.; Dahl, T.; Eiken, O.; Elvebakk, H.; Hansen, F.; Hanssen, T.H.; Jochmann, M.; Johansen, T.A. The Longyearbyen CO₂ Lab of Svalbard, Norway—Initial assessment of the geological conditions for CO₂ sequestration. *Nor. J. Geol. Nor. Geol. Foren.* **2012**, *92*, 353–376.

43. Gilbert, G.L.; O'Neill, H.B.; Nemeč, W.; Thiel, C.; Christiansen, H.H.; Buylaert, J.P. Late Quaternary sedimentation and permafrost development in a Svalbard fjord-valley, Norwegian high Arctic. *Sedimentology* **2018**, *65*, 2531–2558. [[CrossRef](#)]
44. Haskell, N.A. A note on air-coupled surface waves. *Bull. Seismol. Soc. Am.* **1951**, *41*, 295–300.
45. O'Neill, A.; Matsuoka, T. Dominant higher surface-wave modes and possible inversion pitfalls. *J. Environ. Eng. Geophys.* **2005**, *10*, 185–201. [[CrossRef](#)]
46. Tokimatsu, K.; Tamura, S.; Kojima, H. Effects of multiple modes on Rayleigh wave dispersion characteristics. *J. Geotech. Eng.* **1992**, *118*, 1529–1543. [[CrossRef](#)]
47. Lu, L.; Wang, C.; Zhang, B. Inversion of multimode Rayleigh waves in the presence of a low-velocity layer: Numerical and laboratory study. *Geophys. J. Int.* **2007**, *168*, 1235–1246. [[CrossRef](#)]
48. Ryden, N.; Lowe, M.J. Guided wave propagation in three-layer pavement structures. *J. Acoust. Soc. Am.* **2004**, *116*, 2902–2913. [[CrossRef](#)]
49. Xia, J.; Miller, R.D.; Park, C.B.; Tian, G. Inversion of high frequency surface waves with fundamental and higher modes. *J. Appl. Geophys.* **2003**, *52*, 45–57. [[CrossRef](#)]
50. Zhang, S.X.; Chan, L.S. Possible effects of misidentified mode number on Rayleigh wave inversion. *J. Appl. Geophys.* **2003**, *53*, 17–29. [[CrossRef](#)]



© 2020 by the authors. Licensee MDPI, Basel, Switzerland. This article is an open access article distributed under the terms and conditions of the Creative Commons Attribution (CC BY) license (<http://creativecommons.org/licenses/by/4.0/>).

Paper 4

In review in *The Cryosphere*.

Paper 4: Romeyn, R., Hanssen, A., Ruud, B. O., **Stemland, H. M.**, & Johansen, T. A. (2020). Passive seismic recording of cryoseisms in Adventdalen, Svalbard. *The Cryosphere*.

Submitted version reprinted. Preprint published under Open Access license CC BY 4.0. Copyright: The Authors 2020.

doi: <https://doi.org/10.5194/tc-2020-141>

Passive seismic recording of cryoseisms in Adventdalen, Svalbard

Rowan Romeyn^{1,2}, Alfred Hanssen^{1,2}, Bent Ole Ruud^{2,3}, Helene Meling Stemland^{2,3}, Tor Arne Johansen^{2,3,4}

¹Department of Geosciences, University of Tromsø – The Arctic University of Norway, 9037 Tromsø, Norway

²Research Centre for Arctic Petroleum Exploration (ARCEX)

³Department of Earth Science, University of Bergen, 5007 Bergen, Norway

⁴The University Centre in Svalbard (UNIS), 9171 Longyearbyen, Norway

Correspondence to: Rowan Romeyn (rowan.romeyn@uit.no)

Abstract. A series of transient seismic events were discovered in passive seismic recordings from 2D geophone arrays deployed at a frost polygon site in Adventdalen, Svalbard. These events contain a high proportion of surface wave energy and produce high-quality dispersion images through an innovative source localisation approach, based on apparent offset resorting and inter-trace delay minimisation, followed by cross-correlation beamforming dispersion imaging. The dispersion images are highly analogous to surface wave studies of pavements and display a complex multimodal dispersion pattern. Supported by theoretical modelling based on a highly simplified arrangement of horizontal layers, we infer that a ~3.5-4.5 m thick, stiff, high-velocity layer overlies a ~30 m thick layer that is significantly softer and slower at our study site. Based on previous studies we link the upper layer with syngenetic ground-ice formed in aeolian sediments, while the underlying layer is linked to epigenetic permafrost in marine-deltaic sediments containing unfrozen saline pore water. Comparing events from spring and autumn shows that temporal variation can be resolved via passive seismic monitoring. The transient seismic events that we record occur during periods of rapidly changing air temperature. This correlation along with the spatial clustering along the elevated river terrace in a known frost polygon, ice-wedge area and the high proportion of surface wave energy constitutes the primary evidence for us to interpret these events as frost quakes, a class of cryoseism. In this study we have proved the concept of passive seismic monitoring of permafrost in Adventdalen, Svalbard.

1 Introduction

Permafrost is defined as ground that remains at or below 0°C for at least two consecutive years (French, 2017). On Svalbard, an archipelago located in the climatic polar tundra zone (Kottek et al., 2006), at least 90% of the land surface area not covered by glaciers is underlain by

laterally continuous permafrost (Christiansen et al., 2010; Humlum et al., 2003). A seasonally active layer, where freezing/thawing occurs each winter/summer, extends from the surface to a depth of 0.8-1.2 m (Christiansen et al., 2010) and overlies the permafrost. However, the purely thermal definition of permafrost means that the mechanical properties can vary widely depending on the actual ground-ice content. The ground-ice content varies spatially according to sediment texture, organic content, moisture availability and sediment accumulation rate (Gilbert et al., 2016; Kanevskiy et al., 2011; O'Neill and Burn, 2012). Because of the significant impact of ice content on mechanical strength, seismic velocities are a relatively sensitive tool to study the subsurface distribution of ground-ice (Dou et al., 2017; Johansen et al., 2003).

The thermal dynamics of this permafrost environment lead to an interesting phenomenon called cryoseisms, sometimes referred to as frost quakes. Cryoseisms are produced by the sudden cracking of frozen material at the Earth's surface (Battaglia et al., 2016). They are typically observed in conjunction with abrupt drops in air and ground temperature below the freezing point, in the absence of an insulating snow layer and in areas where high water saturation is present in the ground (Barosh, 2000; Battaglia et al., 2016; Matsuoka et al., 2018; Nikonov, 2010). When the surface temperature drops well below 0°C the frozen permeable soil expands, increasing the stress on its surroundings, which can eventually lead to explosive pressure release and tensional fracturing (Barosh, 2000; Battaglia et al., 2016). Seismic waves from these events decay rapidly with distance from the point of rupture, but have been felt at distances of several hundred meters to several kilometres and are usually accompanied by cracking or booming noises, resembling falling trees, gunshots or underground thunder (Leung et al., 2017; Nikonov, 2010). The zero focal depth of cryoseisms means that, relative to tectonic earthquakes, a larger proportion of the energy is distributed in the form of surface waves (Barosh, 2000).

Methods based on the analysis of surface waves are used extensively in engineering fields, such as the non-destructive testing of structures or assessment of the mechanical properties of soils relating to their use as a foundation for built structures (Chillara and Lissenden, 2015; Park et al., 1999; Park et al., 2007; Rose, 2004). In a typical soil profile, the shear velocity and stiffness of the ground increase gradually with depth due to compaction leading to a simple wavefield dominated by fundamental mode Rayleigh waves (Foti et al., 2018). Mechanical properties of the ground are then estimated relatively simply from the geometrical dispersion of the recorded wavefield, i.e., the measured pattern of phase velocity as a function of frequency, where lower frequencies interact with the ground to greater depths than higher frequencies.

By contrast, in permafrost environments, the surface layer freezes solidly during the winter leading to an increase in the shear modulus of the upper layer (Johansen et al., 2003) and an inverse shear velocity with depth profile. This is similar to the case of pavement in civil engineering studies, where a thin, relatively stiff, high-velocity layer at the surface overlies softer and slower ground materials beneath. The high-velocity surface layer acts as a waveguide, permitting the excitation of higher-order wave modes and the wavefield becomes significantly more complicated due to the large number of simultaneously propagating wave modes (Foti et al., 2018; Ryden and Lowe, 2004). Such engineering applications have furthermore driven the development of wave propagation models capable of modelling these complicated wavefields. For example, the ground may be represented by a horizontally layered medium with partial wave balance at the interfaces, for which the dispersion spectrum and stress-displacement field is readily calculated using the global matrix method (Lowe, 1995).



Figure 1: 1:100 000 scale map showing the location of the study area (red box) in Adventdalen. Inset map illustrates the location with respect to the Svalbard archipelago. The Holocene marine limit (red dashed line) is drawn according to Lønne (2005). Map data © Norwegian Polar Institute (npolar.no).

2 Study area and seismic acquisition

Our study site is located in Adventdalen, near the main settlement Longyearbyen on the island Spitsbergen within the Svalbard archipelago in the high Arctic as shown in Figure 1. The climate of this area, as recorded at Longyearbyen airport, is characterised by low mean annual precipitation of 192 mm, and mean annual air temperature of -5.1°C for the period 1990-2004, rising to -2.6°C during the period 2005-2017. The maritime setting and alternating influence of low pressure systems from the south and polar high pressure systems means that rapid temperature swings are common during winter from above 0°C down to -20 or -30°C , while summer temperatures are more stable in the range of 5 - 8°C (Matsuoka et al., 2018). Snow cover in the study area is typically shallow, due to the strong winds that blow along the valley and varies according to local topography with 0 - 0.1 m over local ridges and 0.3 - 0.4 m in troughs. Positive temperature and snowmelt events also occur sporadically through the freezing season (October to May) and subsequently result in the formation of a thin ice-cover. Both shallow snow-cover and thin ice-cover permit efficient ground cooling throughout the freezing season (Matsuoka et al., 2018).

Adventdalen has continuous permafrost extending down to ~ 100 m depth (Humlum et al., 2003), but the highest ground-ice content is restricted to the uppermost ~ 4 m in the loess-covered river terraces that bound the relatively flat, braided Adventelva river plain. The geological setting of the study site is illustrated in Figure 2. The formation of permafrost in Adventdalen began around 3 ka concurrent with the subaerial exposure and onset of aeolian sedimentation on valley-side alluvial terraces (Gilbert et al., 2018). Sediment cores studied by Cable et al. (2018) and Gilbert et al. (2018) show a consistent pattern of an increased ground-ice content over a ~ 4 m thick interval (decreasing towards the coast), beneath a ~ 1 m thick active layer. This interval was observed consistently in cores retrieved from alluvial and loess deposits and is interpreted as ice rich syngenetic permafrost (Cable et al., 2018; Gilbert et al., 2018).

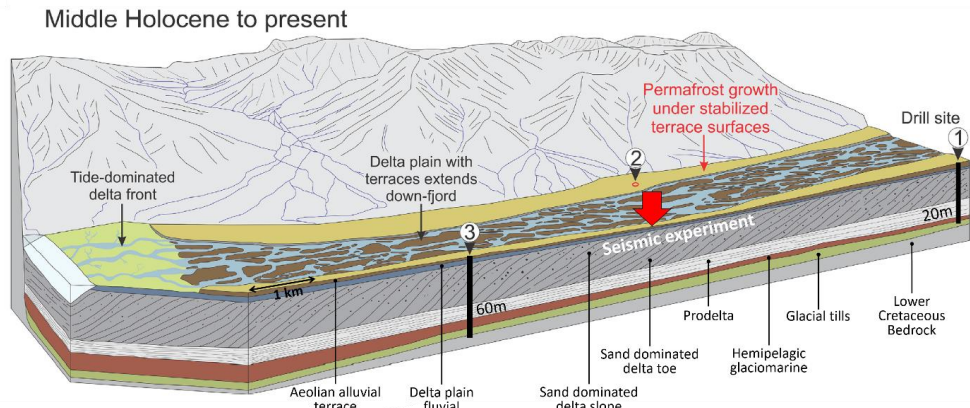


Figure 2: Geological model of Adventdalen, Svalbard modified from Gilbert et al. (2018), the numbered sites mark the coring locations studied by Gilbert et al. (2018) and the red arrow marks the position of the seismic experiments described in this study.

The underlying interval consists of marine-influenced deltaic sediments into which permafrost has grown epigenetically and where ground-ice content remains low (Gilbert et al., 2018). Unfrozen permafrost has been mapped in Adventdalen below the Holocene marine limit (which includes the entire study area as illustrated in Figure 1) using nuclear magnetic resonance and controlled source audio-magnetotelluric data (Keating et al., 2018). This is again related to the presence of saline pore-water in these marine-influenced deltaic sediments that causes the pore-water to remain at least partially unfrozen despite sub-zero temperatures.

Ice wedge polygons, one of the most recognizable landforms in permafrost environments (Christiansen et al., 2016), are present at the investigated site in Adventdalen. They form when freezing winter temperatures cause the ground to contract and crack under stress (Lachenbruch, 1962). Water later infiltrates the cracks and refreezes as thin ice veins that extend down into the permafrost. These veins have lower tensile strength compared to the surrounding ground (Lachenbruch, 1962; Mackay, 1984), so subsequent freeze induced cracking occurs preferentially along this plane of weakness. The repeated cracking, infilling and refreezing causes the ice wedges to grow laterally, forcing the displaced ground upwards and resulting in a series of ridges in a polygonal arrangement that are the surface hallmark of the phenomenon (Christiansen et al., 2016; Lachenbruch, 1962).

Sudden ground accelerations corresponding to cryoseismic events have previously been observed at our study site in Adventdalen. Matsuoka et al. (2018) monitored three ice-wedge

trenches within an area of polygonal patterned ground at the site, using a combination of extensometers, accelerometers and breaking cables connected to timing devices. Their study, which extended over the 12 year period 2005-2017, provides a valuable overview of the seasonality and correspondence between ground motion and environmental parameters. The related study of O'Neill and Christiansen (2018), further details the accelerometer results. Ice-wedge cracking was typically registered in late winter, when the top of the permafrost cooled to around -10°C , resulting in large accelerations of 5 g to more than 100 g. However, O'Neill and Christiansen (2018) also report smaller magnitude accelerations throughout the freezing season, typically in conjunction with rapid surface cooling, that are thought to be caused by the initiation of cracks within the active layer or the horizontal and vertical propagation of existing ice wedge cracks. Given the timing of the field campaigns for the present study, during spring and autumn of 2019, we expect it is rather the latter category of events that have been recorded.

In the present study ground motion was recorded using geophones deployed in 2D arrays (the geometry of which is discussed in sect. 3.3.1). During the spring field campaign, groups of 8 gimballed vertical-component geophones connected in series (geophone type Sensor SM-4/B 14 Hz, 0.7 damping and spurious frequency of 190 Hz) were deployed on the snow surface at each receiver location. During deployment for the autumn field campaign, geophones were embedded into the unfrozen ground surface as an assortment of spike geophones (Sercel SG-10 10Hz) connected in series in strings of 4 geophones and 3C geophones (DT-Solo 3C with z-element HP301V-10Hz) where only the vertical channel was used. Both of these geophone types have damping of 0.7, giving a flat response above the natural frequency up to the spurious frequency of 240 Hz. Data was recorded for defined time intervals as will be discussed in sect. 4.1, mandated primarily by battery considerations.

3 Methods

In this study, we present a methodology to isolate transient seismic signals in passive seismic recordings from two-dimensional vertical component geophone arrays. These transient signals contain surface wave energy with relatively high signal-to-noise ratio. We implement a novel method to localise the unknown source position of these signals based on the 2D receiver array geometry and subsequently recover dispersion spectra using a cross-correlation beamforming technique. In order to infer subsurface physical properties we generate theoretical dispersion curves using the global matrix method (Lowe, 1995) based on idealized horizontally layered

media models. The forward model is manually tuned to achieve best fit with the experimentally observed dispersion spectra. Similar experiments were conducted over two field campaigns in the spring and autumn in order to investigate temporal variation in permafrost mechanical strength.

3.1 Isolation of microseismic events in passive records

Our passive seismic recordings contain a significant amount of non-surface wave energy, including wind noise and air waves. As a result we find it more effective to isolate and analyse specific transient microseismic events rather than attempting to recover the Green's function from ambient noise cross correlations as, e.g., Sergeant et al. (2020) have done for passive recordings on glaciers. The periodic microseismic signals are isolated from background random noise based on permutation entropy, a nonlinear statistical measure of randomness in a time series (Bandt and Pompe, 2002), that produces local minima for coherent signals embedded in noise. We use the implementation of Unakafova and Keller (2013) using ordinal patterns of third order extracted over successive samples and a sliding window size of 200 samples. We then apply a peak-finding algorithm to identify local minima in permutation entropy that meet peak prominence criteria defined by thresholds of peak value, height and width. An example of event detection is shown in Figure 3 for real, noisy data recorded at the study site.

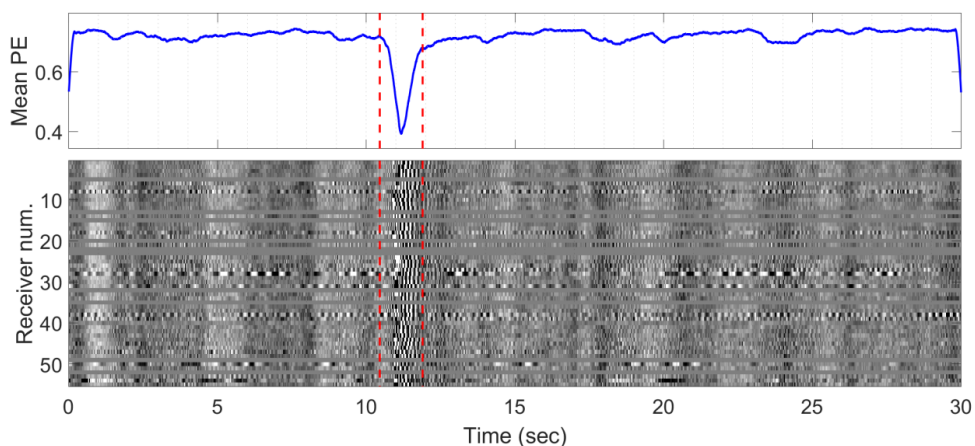


Figure 3: Detection of transient event based on mean permutation entropy (PE), a metric that peaks towards minima when coherent amplitudes are recorded across the array of receivers. Red dashed lines mark the temporal extent of the extracted event that is shown in greater detail in Figure 4. This event was recorded 30-Mar-2019 at 18:06.

The isolated microseismic events can be subsequently processed in a similar way to active source experiments, i.e. using well established multichannel analysis of surface waves (MASW) methodologies, with modification due to the unknown source position.

3.2 MASW dispersion imaging with unknown source position

Several processing methods for multichannel analysis of surface waves (MASW) are possible depending on the acquisition setup. One of the most well-known is the 1D phase shift method of Park et al. (1998), that is straightforward to apply for line arrays of receivers and inline sources at known offsets. The dispersion image is built by scanning over frequency (ω) and phase velocity (v) according to,

$$E_{1D}(\omega, v) = \left| \sum_{i=1}^N e^{j\phi_i} R_i(\omega) \right|, \quad (1)$$

where $R_i(\omega)$ is the Fourier transform of the i -th trace $r_i(t)$ of N recorded traces and $\phi_i = \omega x_i / v$ is the corresponding phase shift at known source-receiver offset x_i . On the other hand, processing of passively recorded microseismic events is complicated by the fact that the source position is unknown. We employed a 2D receiver array to allow us to localise the unknown passive seismic sources. Again, there are several possibilities to process the 2D array data. For example, Park et al. (2004) describe an azimuth scanning technique assuming far-field sources and utilizing the plane-wave projection principle. The dispersion image is formed according to,

$$E_{2D}(\omega, v, \theta) = \left| \sum_{i=1}^N e^{j\phi_x} e^{j\phi_y} R_i(x, y, \omega) \right|, \quad (2)$$

where $R_i(x, y, \omega)$ is the Fourier transform of the i -th trace $r_i(x, y, t)$, located at position (x, y) , of N recorded traces and $\phi_x = -\omega x \cos \theta / v$ and $\phi_y = -\omega y \sin \theta / v$ are the phase shifts corresponding to the x and y components of the phase velocity, where θ denotes the source azimuth. We implement this approach by computing, for each combination of velocity and frequency, the azimuth that maximizes the spectral magnitude. The source azimuth is thus estimated by calculating the modal azimuth across all frequencies and velocities and the dispersion spectrum can be formed by fixing the azimuth and reiterating over frequency and velocity axes. The key drawback of forming the dispersion image according to Eq. (2) is that the source should be distant enough that the plane wave assumption is valid. In Figure 4 we

demonstrate that our experimental data is not consistent with the far-field source approximation, since moving the source position closer to the array simplifies the structure of the apparent offset sorted gather. This observation led us to develop an alternative processing approach.

3.3 Two-step MASW approach

We propose a two-step processing approach where the first step involves locating the unknown source position, permitting the dispersion image to be formed in the second step. Even the simplest 1D phase shift method from Eq. (1) will give superior results to Eq. (2) if a nearby source can be reliably located. Our approach is based on the idea that if the source position was known, the seismic traces from the 2D array could be arranged by their apparent offset from the source to form a shot gather that resembles the simple case of a line array with an inline source at known offset. Figure 4 shows that when we determine the source azimuth using Eq. (2) and re-sort the recorded traces by offset to a distant source lying along this azimuth we observe that the gather begins to resemble the response of a line array. However, when we shift the assumed source position closer to the array, the offset sorted gather resembles the simple linear array response even more closely. Thus, by formalising a metric that encodes the resemblance of an apparent offset sorted gather to a line array response, we can obtain a useful tool for source localisation that leverages the 2D array geometry. This further avoids the problem of picking specific P- and S-phase arrivals, a traditional seismological method for source localisation, since these arrivals are difficult to detect reliably in our experimental data.

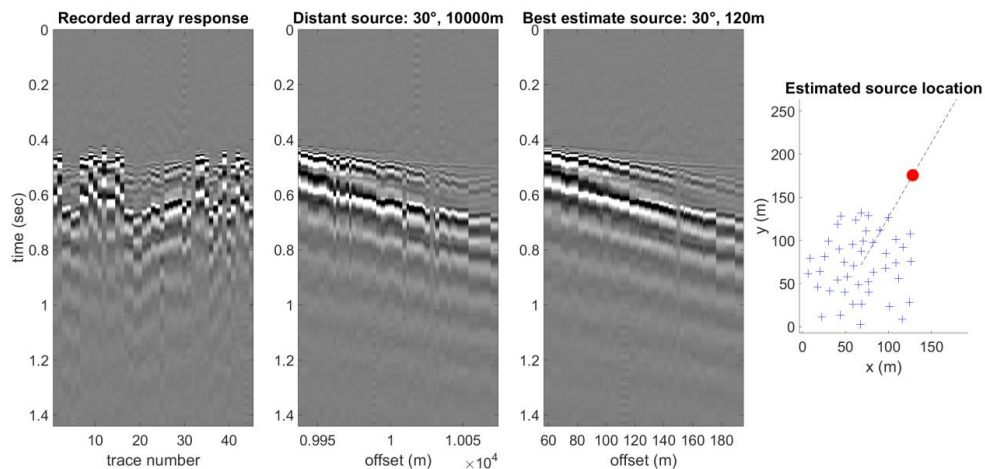


Figure 4 – Field recording of a transient event, whose detection is highlighted in Figure 3, demonstrates that re-sorting traces by apparent offset to a distant source produces a gather with poorer coherence than re-sorting by offset to the best estimate source range at 120 m. Blue crosses denote geophones, while the red circle marks the best estimate source position.

3.3.1 Step 1 - Source localisation

The source is located by re-sorting the seismic traces by offset to a series of test positions. The validity of a given test position is assessed by summing the magnitude of the delays between neighbouring traces in the re-sorted gather. The delays between neighbouring traces are estimated based on the lag that gives maximal value to the normalised cross-correlation between the two signals. The delays are estimated on a relatively narrowband filtered copy of the seismic (10-15-30-45 Hz Ormsby filter), to minimise the influence of random noise and dispersion. After sorting, the source position is selected as the test position that produces the smallest magnitude sum of adjacent trace delays, corresponding to the simplest and most coherent offset sorted gather. This simple approach works well in practice and is fast enough to allow a relatively large number of test positions to be evaluated. However, the most coherent offset sorted gather may correspond to unphysical negative velocities, indicating the true source azimuth lies 180° from the selected azimuth. This situation is identified and corrected by comparing summed frequency-wavenumber (FK) transform magnitudes corresponding to negative k -space to those of positive k -space. If negative k -space produces a larger sum than positive k -space, a negative dip corresponding to unphysical negative velocities exists and we rotate the selected source azimuth 180° .

In Figure 5 we show that the source azimuths estimated using this technique are consistent with those estimated by picking maxima in azimuth scans using Eq. (2), but have the additional benefit that the source range is also estimated.

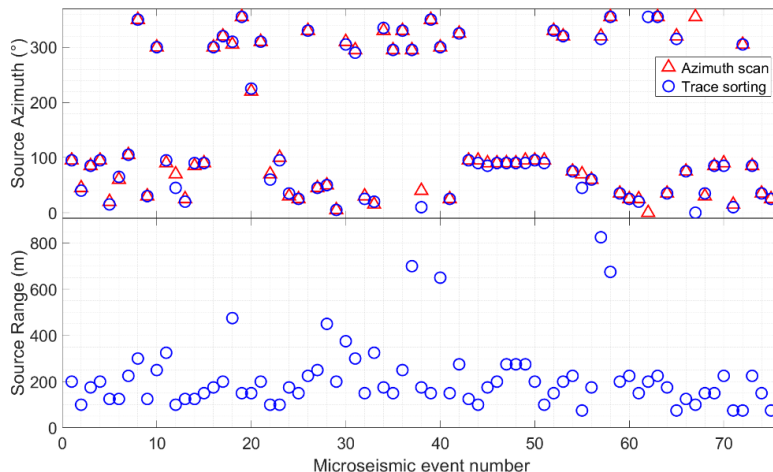


Figure 5 – Comparison of source localisation using the Azimuth Scanning approach, i.e., Eq. (2) (red triangles) and the new approach based on trace re-sorting and delay minimisation (blue circles) which also allows range estimation. Azimuths are given as compass bearings.

The reliability of the proposed method of source localisation was tested using synthetic gathers corresponding to a set of known source azimuths and ranges. We ran a 1D noise-free forward model (that accounts for 3D wavefield divergence) using the OASES package for seismic-acoustic propagation in horizontally stratified waveguides, which employs a wavenumber-integration solution method (Schmidt and Jensen, 1985). We model the wavefield using the layer properties corresponding to the spring field conditions detailed in Table 1. We then specify the receiver positions as deployed in the field and form the synthetic gathers by selecting traces with appropriate offset from the 1D pre-calculated wavefield. The range and azimuth errors produced when attempting to recover the known source positions using the proposed source localisation approach are illustrated in Figure 6. The proposed method demonstrates an excellent ability to recover the direction to the source, regardless of azimuth, although uncertainties relating to the true receiver positions in the field are also important to consider (see sect. 3.3.3). We also observe reliable estimation of source range within a radius of ~ 500 m from the array centre, beyond which we observe an increasing tendency to underestimate the source range. Further tests with a range of different array geometries indicate that the array

aperture is the dominant factor controlling the maximum source range that can be estimated reliably.

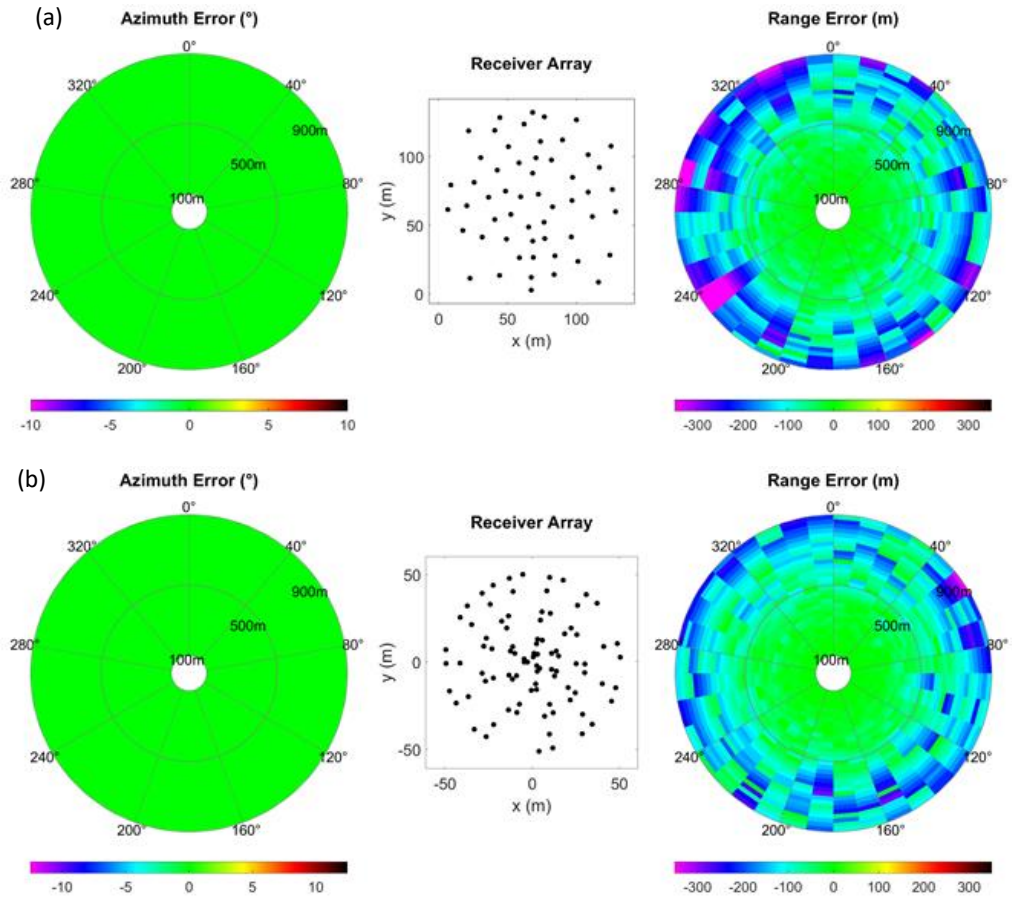


Figure 6: Predicted source localization azimuth and range errors based on forward modelling with known source positions and receiver geometry corresponding to (a) spring and (b) autumn field campaigns.

3.3.2 Step 2 - Dispersion imaging

Once the seismic traces from the 2D array have been sorted by the apparent offset to the localised source, we are left with a gather that resembles a linear receiver array and an inline source, as seen in Figure 4. At this point, the dispersion image may simply be formed by applying Eq. (1), i.e., the 1D phase shift method of Park et al. (1998). However, more advanced processing methodologies have emerged over time and we observe significantly improved

dispersion imaging using the cross-correlation beamforming approach of Le Feuvre et al. (2015), as demonstrated in Figure 7. This approach utilizes the cross-correlations between all possible pairs of receivers, rather than the recorded traces themselves, to increase the effective spatial sampling of the array and thereby reduce aliasing and increase signal-to-noise ratio. In an adaption of this approach, we form the dispersion image, $D(\omega, v)$, a function of frequency (ω) and phase velocity (v), according to the following equation using the source position, $r_S(\mathbf{x}, \mathbf{y})$, estimated as described in Sect. 3.3.1:

$$D(\omega, v) = \left| \sum_{j=1}^{N_R-1} \sum_{k=j+1}^{N_R} \delta(\omega, v, r_s, r_j, r_k) \right|, \quad (3)$$

with N_R the number of receivers and $r_j(\mathbf{x}, \mathbf{y})$, $r_k(\mathbf{x}, \mathbf{y})$ denoting the positions of the receivers for the cross-correlation pair. Furthermore:

$$\delta(\omega, v, r_s, r_j, r_k) = \begin{cases} \tilde{C}_{jk}(\omega) e^{i\omega \frac{\|r_s - r_k\| - \|r_s - r_j\|}{v}} & \text{if } \|r_s - r_j\| \leq \|r_s - r_k\|, \\ \tilde{C}_{kj}(\omega) e^{i\omega \frac{\|r_s - r_j\| - \|r_s - r_k\|}{v}} & \text{if } \|r_s - r_j\| > \|r_s - r_k\|. \end{cases} \quad (4)$$

Here, the causal cross-correlations \tilde{C}_{jk} and \tilde{C}_{kj} between the receivers located at r_j and r_k are selected according to the direction of propagation, determined by comparing the two source-to-receiver distances, while the propagation distance is given by the difference between the two. In practice, we do not compute the cross correlation \tilde{C}_{kj} directly, but instead use the equivalent time-reversed acausal part (negative time delays) of \tilde{C}_{jk} (Le Feuvre et al., 2015). It is important that the seismic traces are pre-whitened prior to computing the cross correlations, as whitening effectively removes the autocorrelation of the signals that can blur the cross-correlation (El-Gohary and McNames, 2007). We find that a simple first-order backward differencing scheme is an effective method to whiten the recorded traces. We furthermore find it convenient to normalise the frequency response of the dispersion spectrum so that the maximum amplitude along a given frequency is unity.

It should also be noted that it is possible to localise the source by searching for source positions that produce dispersion images with maximum amplitude, as the correct source location is expected to produce the most coherent high-amplitude dispersion modes (Le Feuvre et al.,

2015). This approach was tested in the present study. However, we find this method very slow and inefficient compared to the trace resorting approach we implement, even though maximising dispersion image magnitude does appear a valid approach for locating an unknown source.

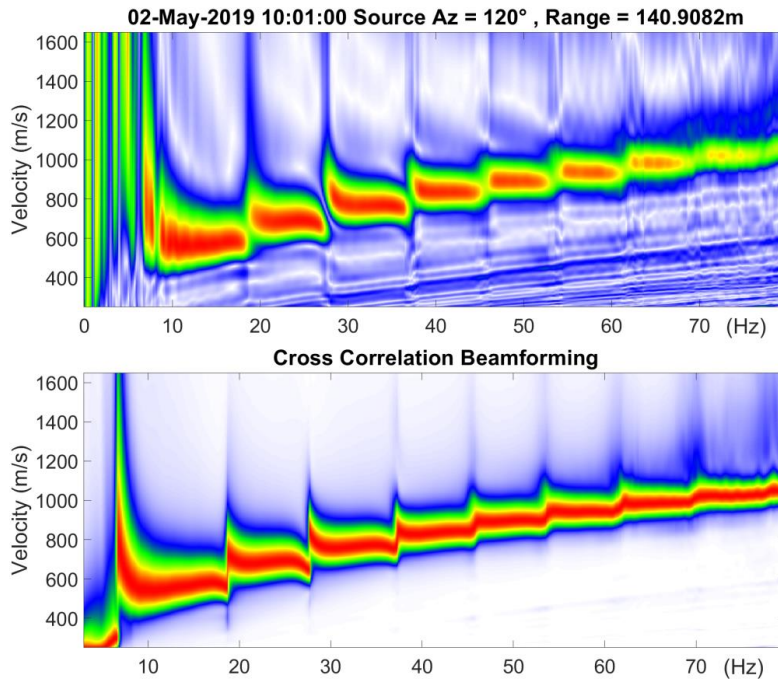


Figure 7: Dispersion spectra using 1D phase shift method (top) and Le Feuvre et al. (2015) cross correlation beamforming (bottom). Source position was localised using delay minimisation approach in both cases and colour scales are linear.

3.3.3 Influence of receiver position errors

During the field campaigns, we recorded GPS positions at the recording nodes that the receivers are connected to, rather than at the receivers themselves. The positions of the receivers were subsequently assigned based on an approximate dead reckoning approach and therefore have a degree of uncertainty associated with them. We estimate that this positional uncertainty lies in the range of $\sim 2\text{-}3$ m. The impact of receiver position errors was investigated using an OASES 1D seismo-acoustic propagation model (Schmidt and Jensen, 1985), for the horizontally stratified waveguide corresponding to the spring field conditions detailed in Table 1. We extracted a reference gather assuming a source range of 200 m, an azimuth of 100° and receiver

geometry corresponding to the spring field campaign. We then ran 1000 iterations adding flat-spectrum random perturbations to the receiver positions. By setting the maximum amplitude of the perturbation, we effectively define a circle with radius corresponding to this amplitude, where there is equal probability that the receiver is positioned at any given point within this circle. We then measure the impact of these perturbations on both source localisation and dispersion spectra. The dispersion spectrum error (ε^2) is given by the sum of squared differences for a given noise-perturbed trial S_{test} , compared to a noise-free reference spectrum S_{ref} over n frequencies (ω) and m velocities (v):

$$\varepsilon^2 = \sum_{i=1}^n \sum_{j=1}^m (S_{test}(\omega_i, v_j) - S_{ref}(\omega_i, v_j))^2. \quad (5)$$

In Figure 8 we show that positional errors up to 4-5 m in radius have a very minor impact on source azimuth estimation and dispersion spectra in the frequency range of interest, i.e., up to 100 Hz. Range estimation is somewhat more sensitive (but less important to dispersion spectrum quality) and we see a general trend that the source range tends to be overestimated rather than underestimated under the influence of receiver position uncertainty. This indicates that the estimated positional uncertainty for the field campaigns (~2-3 m) should not significantly affect our experimental results, although we may expect some minor overestimation of source range. As the positional error magnitude increases further, Figure 8 demonstrates that the source localisation becomes progressively more imprecise, while Figure 9 shows that the maximum frequency imaged coherently in the dispersion spectra progressively decreases. We can formalise this trend by observing the relation that coherent dispersion spectra are recovered for wavelengths of approximately 2-3 times the maximum positional error magnitude.

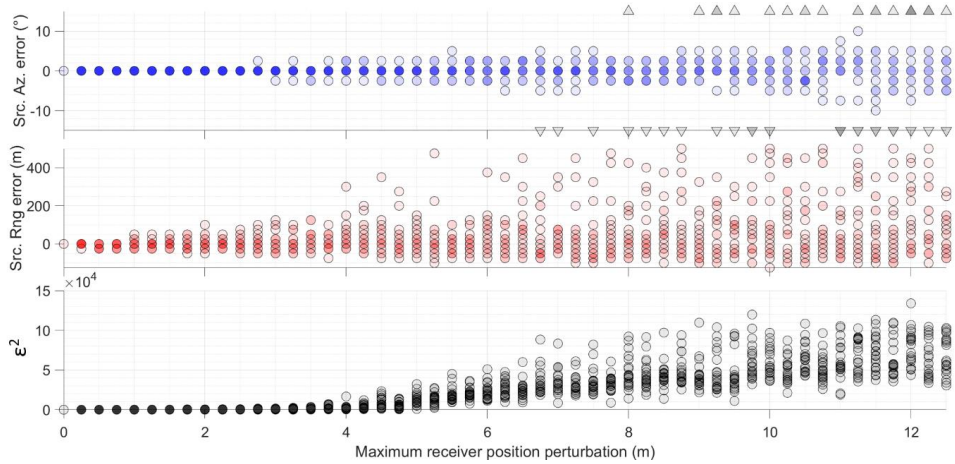


Figure 8: Summary of results of 1000 modelling iterations with random white noise perturbation to receiver positions. Grey triangles denote outliers, i.e., iterations that result in large azimuth errors outside the plotted range. Higher colour density denotes overlap, i.e. multiple iterations with the same result. ϵ^2 denotes dispersion spectrum error Eq. (5).

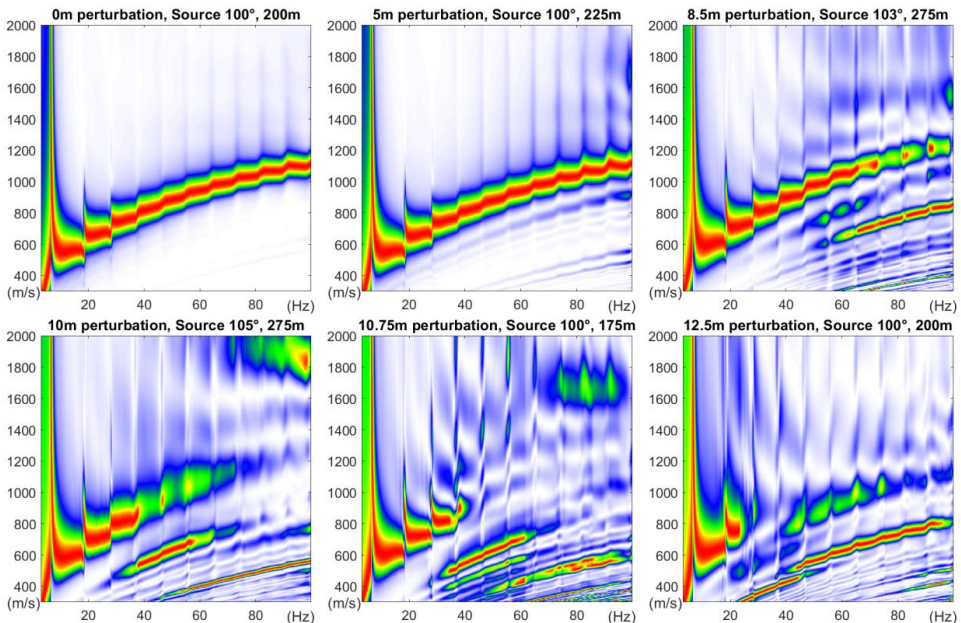


Figure 9: Dispersion spectra calculated from forward model with receiver positions perturbed by white random noise of known magnitude illustrating how the maximum frequency that is coherently imaged decreases with increasing uncertainty in receiver position. Colour scale is linear.

3.4 Theoretical dispersion curve modelling

The global matrix method was introduced by Knopoff (1964), further elaborated by Lowe (1995) and again by Ryden and Lowe (2004). It involves the assembly of a system matrix \mathbf{S} that describes the interaction of displacement and stress fields across interfaces between horizontal layers described by a series of interface matrices. The propagating wavemodes are characterised by combinations of frequency (ω) and wavenumber (k) that satisfy all boundary conditions such that the determinant vanishes:

$$f(\omega, k) = \det[\mathbf{S}] = 0 \quad (6)$$

We abstain from providing a full derivation, but give a specific case study that illustrates our implementation and may serve as a simple practical reference point for the reader interested in further exploration of the method. The layer models used in this study contain two discrete layers ($i = 2, 3$) bounded by an infinite vacuum half-space above ($i = 1$) and a solid half-space below ($i = 4$), giving the system matrix the following form:

$$\mathbf{S} = \begin{bmatrix} \mathbf{D}_{1b}^- & -\mathbf{D}_{2t} & & \\ & \mathbf{D}_{2b} & -\mathbf{D}_{3t} & \\ & & \mathbf{D}_{3b} & -\mathbf{D}_{4t}^+ \end{bmatrix}, \quad (7)$$

where the matrices describing the top interfaces \mathbf{D}_t and the bottom interfaces \mathbf{D}_b for each layer are given by the following expressions (noting that the minus superscript denotes taking only the upward travelling partial waves given by columns two and four, while the plus superscript denotes selecting only the downward travelling partial waves given by columns one and three):

$$[\mathbf{D}_{it}] = \begin{bmatrix} k & kg_\alpha & C_\beta & -C_\beta g_\beta \\ C_\alpha & -C_\alpha g_\alpha & -k & -kg_\beta \\ i\rho_i B & i\rho_i B g_\alpha & -2i\rho_i k B^2 C_\beta & 2i\rho_i k B^2 C_\beta g_\beta \\ 2i\rho_i k B^2 C_\alpha & -2i\rho_i k B^2 C_\alpha g_\alpha & i\rho_i B & i\rho_i B g_\beta \end{bmatrix}, \quad (8)$$

$$[\mathbf{D}_{ib}] = \begin{bmatrix} kg_\alpha & k & C_\beta g_\beta & -C_\beta \\ C_\alpha g_\alpha & -C_\alpha & -kg_\beta & -k \\ i\rho_i B g_\alpha & i\rho_i B & -2i\rho_i k B^2 C_\beta g_\beta & 2i\rho_i k B^2 C_\beta \\ 2i\rho_i k B^2 C_\alpha g_\alpha & -2i\rho_i k B^2 C_\alpha & i\rho_i B g_\beta & i\rho_i B \end{bmatrix}, \quad (9)$$

with:

$$g_\alpha = e^{iC_\alpha h_i}, \quad g_\beta = e^{iC_\beta h_i}, \quad (10)$$

$$C_\alpha = \left(\frac{\omega^2}{\alpha_i^2} - k^2\right)^{\frac{1}{2}}, \quad C_\beta = \left(\frac{\omega^2}{\beta_i^2} - k^2\right)^{\frac{1}{2}}, \quad (11)$$

$$B = \omega^2 - 2\beta_1^2 k^2, \quad (12)$$

and the physical properties of the system enter as:

h_i = thickness of layer i , zero for the half-spaces

ρ_i = density of layer i , set to zero for the upper vacuum half-space

α_i = bulk compressional velocity of layer i , arbitrary non-zero value for upper vacuum half-space

β_i = bulk shear velocity of layer i , arbitrary non-zero value for upper vacuum half-space.

We are also interested in the magnitude of displacement at the ground surface (top interface of layer $i=2$) for the different wave modes so that we may predict which are most likely to be excited and subsequently recorded in the field. To this end, we proceed by assuming the amplitudes of the incoming waves in the two half spaces, setting a unitary amplitude entering the system at the top ($\{A_1^+\} = 1$) and zero amplitude entering the system from below ($\{A_4^-\} = 0$), allowing us to specify the right-hand side of the following system and solve for the unknown interface amplitudes using a least squares approach:

$$\begin{bmatrix} \mathbf{D}_{1b}^- & -\mathbf{D}_{2t} & & \\ & \mathbf{D}_{2b} & -\mathbf{D}_{3t} & \\ & & \mathbf{D}_{3b} & -\mathbf{D}_{4t}^+ \end{bmatrix} \begin{Bmatrix} \{A_1^-\} \\ \{A_2\} \\ \{A_3\} \\ \{A_4^+\} \end{Bmatrix} = \begin{bmatrix} \mathbf{D}_{1b}^- & & & \\ & & & \\ & & & \\ & & & -\mathbf{D}_{4t}^+ \end{bmatrix} \begin{Bmatrix} \{A_1^+\} \\ 0 \\ 0 \\ \{A_4^-\} \end{Bmatrix}. \quad (13)$$

Here we substitute the system matrix \mathbf{S} for the combinations of frequency and wavenumber that correspond to the propagating wavemodes. The vectors of amplitudes are arranged in the following way:

$$\{A\} = \begin{Bmatrix} A_{(L+)} \\ A_{(L-)} \\ A_{(S+)} \\ A_{(S-)} \end{Bmatrix}, \quad \{A^+\} = \begin{Bmatrix} A_{(L+)} \\ A_{(S+)} \end{Bmatrix}, \quad \{A^-\} = \begin{Bmatrix} A_{(L-)} \\ A_{(S-)} \end{Bmatrix}, \quad (14)$$

where L and S denote longitudinal and shear waves respectively, while $-$ and $+$ symbols denote upward and downward travelling partial waves. Having solved for the unknown amplitudes in Eq. (13) we then calculate the displacements and stresses at the ground surface according to the following equation,

$$\begin{Bmatrix} u_x \\ u_z \\ \sigma_{zz} \\ \sigma_{xz} \end{Bmatrix}_{2t} = [\mathbf{D}_{2t}]\{A_2\}, \quad (15)$$

where u_x and u_z denote the complex valued in-plane and vertical displacements, while σ_{zz} and σ_{xz} denote the complex valued vertical and lateral stresses and the calculation is made at the top interface of layer 2.

In Figure 10, we show an example of the dispersion curves produced by this approach for the spring layer properties listed in Table 1. Since we measured the vertical component of ground motion in the field, we plot the magnitude of the vertical displacement (u_z) as an indicator of the relative likelihood of exciting and subsequently recording specific wave modes. We also highlight, for a given frequency, the wavemode giving the largest displacement at the surface that is considered most likely to dominate the ground response and contribute to the apparent dispersion curve produced by the superposition of multiple modes observed in experimental data.

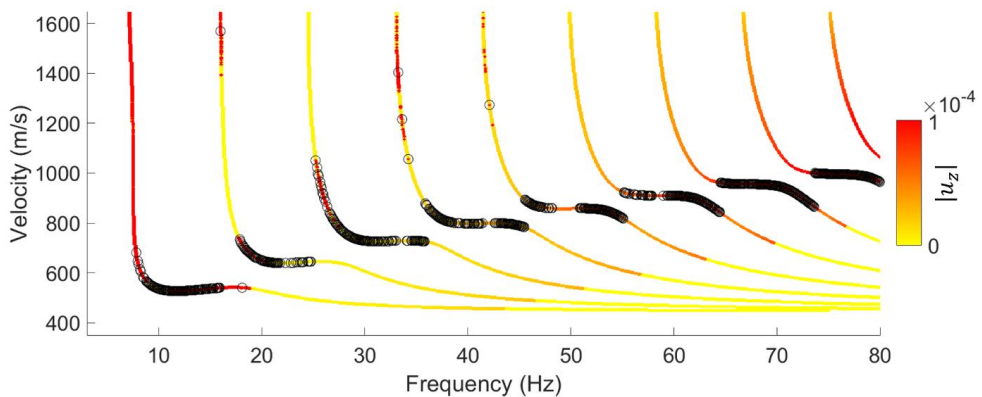


Figure 10: Example of theoretical dispersion curves coloured by magnitude of vertical displacement at the ground surface. Black circles denote the wavemode with largest displacement for a particular frequency.

3.4.1 Numerical root finding method

To recover the dispersion curves it is necessary to find the roots of the system matrix, Eq. (6). In this study, we assume a half-space with higher velocity than the overlying layers, which reflects the presence of compacted sediments and bedrock at depth in Adventdalen. The implication of this choice is that the propagating surface wave modes do not leak energy into the half-space and are much simpler to search for numerically. The permitted surface wave

modes are given by combinations of frequency and phase velocity (or wavenumber) that minimize the determinant of the system matrix. We localize these minima by conducting a simple 2D numerical search over a regular grid of frequency and real wavenumber (the imaginary part of the wavenumber is zeroed since we consider only non-leaky modes). The local minima in the matrix sampling the determinant of the system matrix are found by morphological image processing techniques, rather than the more traditional method of curve tracing using bisection algorithms favoured by, e.g., Lowe (1995). Specifically, we use the “*imregionalmax*” routine in Matlab on the negative of the determinant matrix, applying a series of linear connectivity kernels for detection of local maxima ridges. We then mask out non-dispersive body waves that appear as horizontal ridges in frequency-phase velocity space and use morphological closing operations to fill in the gaps that this creates. We further apply skeletonization to the binary image of dispersion curves. The non-zero elements of the binary matrix then define the combinations of frequency and velocity that represent the dispersive wave modes and that are subsequently used to calculate surface wave amplitudes with Eq. (13).

4 Results and discussion

4.1 Interpretation of cryoseisms

A series of transient seismic events were isolated from passive seismic recordings of 2D geophone arrays deployed at our study site in Adventdalen. The estimated source positions for these events are shown in Figure 11, while their temporal occurrence is illustrated in Figure 12. The events cluster primarily around frost polygons along the raised river-terrace. A small number of events fall just beyond the raised riverbank and plot within the Adventelva river valley. While these events may be correctly located, we also cannot rule out the possibility that they occurred on the raised terrace and the source range has been overestimated as discussed in sect. 3.3.3. Figure 12 shows that the transient events were all recorded during periods of rapidly changing air temperature as recorded at a nearby weather station. This observation together with the spatial clustering around frost polygons and on the raised river terrace, which is known to have high ground-ice content within the upper ~4 m (Gilbert et al., 2018), lead us to infer that these events are most likely cryoseisms, or frost quakes. The fact that these events consist dominantly of surface wave energy is also consistent with a shallow source and previous descriptions of cryoseisms (Barosh, 2000). Similarly, the fact that the source range for all of the recorded events was in the order of hundreds of meters is also consistent with the distance

over which previously observed cryoseisms have propagated (Leung et al., 2017; Nikonov, 2010) and we are unaware of any other likely seismic sources within this range. Other possible seismic sources such as an operational coal mine, Gruve 7, that conducts blasting operations lies ~5 km SE, road traffic along the road ~650-850 m S-SW or snowmobile traffic along the Adventelva river valley N-E of the study site do not explain the spatial distribution and character of the recorded events. Known examples of snowmobile and vehicle traffic contain strong air wave arrivals with non-dispersive velocity of ~320-330 m/s that was not observed for the class of events attributed to cryoseisms.

The temporal resolution of this study is limited due to the fact that data was recorded during specific intervals, rather than continuously (see Figure 12). This means that additional cryoseisms may have occurred under rapid cooling events that occurred during the field campaigns but for which no data was recorded. However, we can observe that the recording windows for which no cryoseisms were detected were associated with either temperatures that were too high or changing slowly in comparison to the periods when cryoseisms were detected. The frequency of cryoseisms was greater during the spring compared to the autumn, probably owing to the increased progression of ground freezing in the aftermath of cold winter air temperatures. It is interesting to note that the highest frequency of cryoseisms was recorded the 2nd of May, 2019 during a period when the air temperature was rapidly increasing and following a sharp cold snap down from above-freezing temperatures three days prior. It is unclear whether these events are a delayed effect of the preceding cold snap, where the subsurface stress continues to increase for some time after the drop in air temperature, or if the events are caused by the sharp temperature rise itself and associated with cracking driven by thermal expansion rather contraction. We also note that snow cover on the raised river terrace was thin or absent during the field campaigns, due to relatively low precipitation and strong prevailing winds. The lack of an insulating snow layer increases the plausibility of correlating air temperature at 5 m above ground with cryoseismic events in the shallow subsurface and has been recognised as a necessary condition facilitating sufficiently rapid ground cooling to generate cryoseisms in previous studies (Barosh, 2000; Battaglia et al., 2016; Matsuoka et al., 2018; Nikonov, 2010).

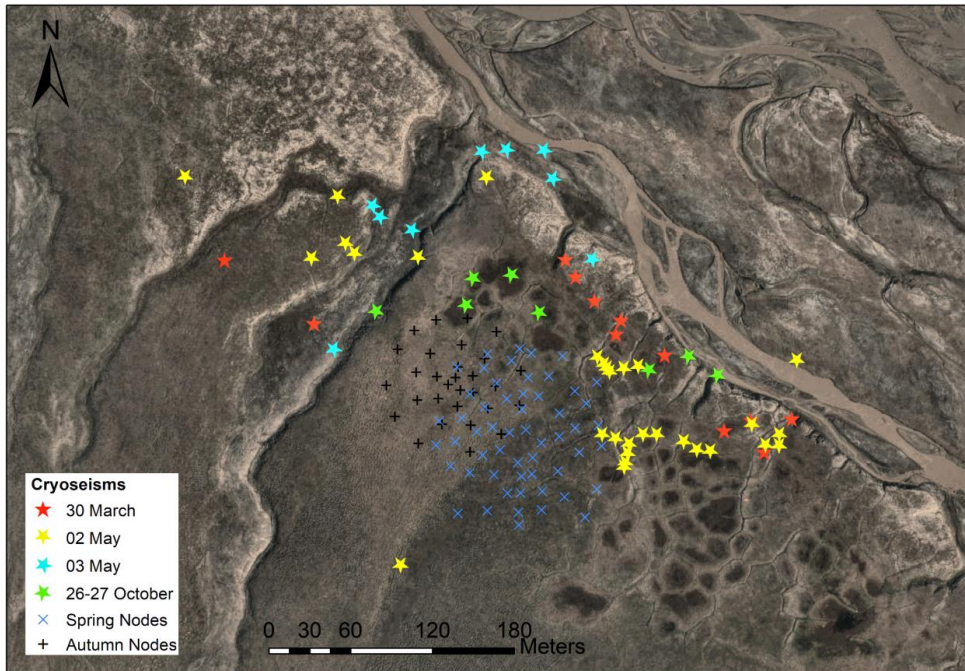


Figure 11: Localised source positions (coloured stars) and receiver positions for spring (cross symbols) and autumn (plus symbols) field campaigns, background is a contrast enhanced version of an orthophoto © Norwegian Polar Institute (npolar.no).

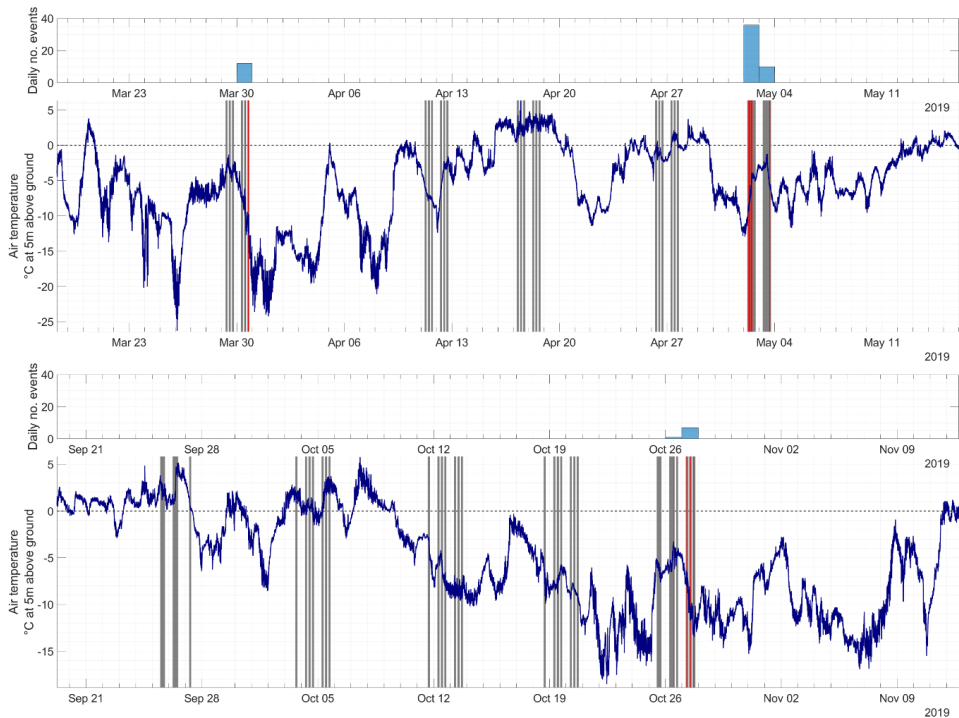


Figure 12 – Temperature at 5 m above ground at nearby weather station in Adventdalen. Grey bars denote periods when passive seismic data was recorded and red bars denote periods where transient seismic events producing high quality dispersion spectra were detected.

4.2 Dispersion images and temporal variation

Dispersion images from the isolated cryoseisms resemble the complex multimodal dispersion of Lamb-Rayleigh waves that is relatively well known from pavement studies (Ryden and Lowe, 2004; Ryden et al., 2004). This complexity emerges when a stiff high-velocity layer overlies a softer layer producing an inversion in the shear velocity profile and acting as a waveguide. Some examples of estimated dispersion spectra are shown in Figure 13 spanning both spring and autumn field campaigns. We observe that the number of wavemode branches imaged in the spring records was higher than in the autumn over the investigated range of frequencies. In Figure 14, we compare individual events from spring and autumn, and observe that the apparent dispersion curve is shifted towards lower velocities in the autumn and that transitions between successive modes are shifted to higher frequencies with larger spacing between modes. This trend is robust across the catalogue of cryoseisms giving well resolved dispersion images, as shown in Figure 15, displaying the time-frequency traced ridges of

dispersion images corresponding to multiple records from spring and autumn field campaigns. Matlab's built in routine "*tfridge*" was found to be effective for ridge tracing in this study.

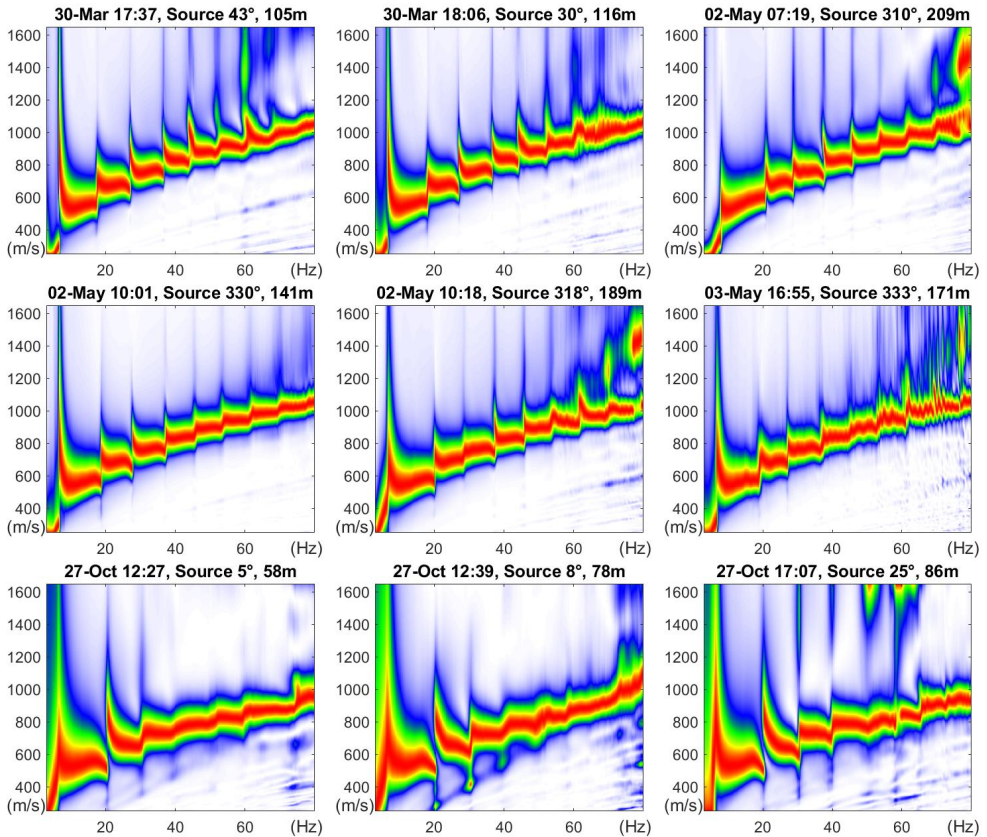


Figure 13: Examples of dispersion spectra for selected cryoseismic events from spring (upper two rows) and autumn (bottom row) field campaigns, source azimuths are given as compass bearings and colour scaling is linear.

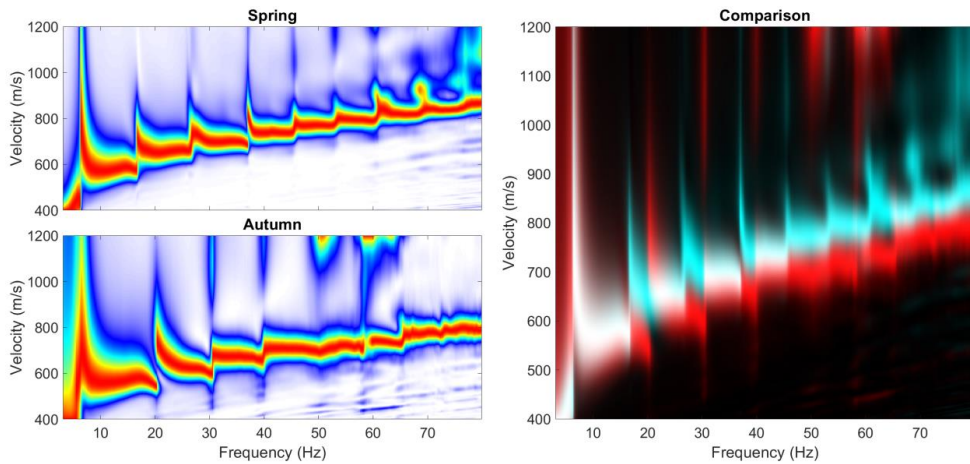


Figure 14: Comparison of records from spring and autumn, in right panel spring record is shown in cyan and autumn record is shown in red, and areas where the two spectra overlap appear white.

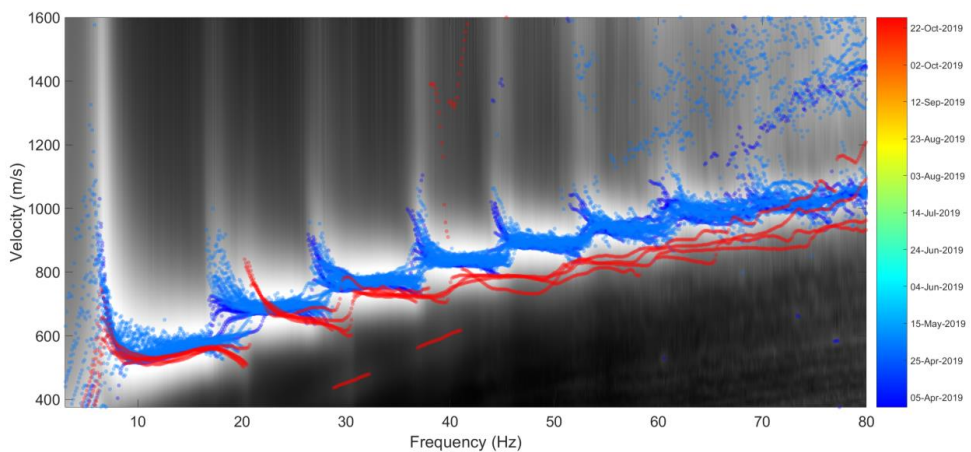


Figure 15: Illustration of temporal variation. Grayscale background image shows the mean dispersion spectrum for all displayed transient events. Coloured circles denote time frequency ridges picked from individual dispersion spectra and coloured according to date of recording.

4.3 Inferring subsurface structure from dispersion images

To further investigate what the structure of the dispersion images tells us about the subsurface permafrost structure and its variation between spring and autumn field campaigns, we ran a series of theoretical models using the global matrix approach discussed in sect. 3.4. These models were optimised manually by qualitatively fitting the resulting dispersion curves with experimental dispersion images and manually adjusting the physical parameters to achieve a

best possible fit. We focussed our attention on the simplest possible models that give a good approximation of the experimental data, which in this case meant two discrete layers with an inverse velocity profile sandwiched between infinite vacuum (above) and solid (below) half-spaces. The physical properties of the best estimate models corresponding to spring and autumn conditions are listed in Table 1.

Table 1: Physical properties of homogeneous, horizontally layered media used to calculate theoretical dispersion curves shown in Figure 16. The key feature of the model is a high velocity surface layer overlying a layer with lower velocity and high Poisson's ratio.

Layer	h (m)		V_s (m/s)		V_p (m/s)		Poisson's Ratio		ρ (kg/m ³)
	Spring	Autumn	Spring	Autumn	Spring	Autumn	Spring	Autumn	
1	4.5	3.5	1700	1520	3180	3164	0.30	0.35	2000
2	31	29	500	525	1837	1929	0.46	0.46	2000
halfspace	∞	∞	2000	2000	3742	3742	0.30	0.30	2000

The primary property of the models that allows us to fit the experimental data is the high velocity of the uppermost part of the ground, overlying relatively low velocity material beneath. We also see evidence that the Poisson's ratio in the low velocity layer is relatively high (0.46), consistent with a softer material that transmits shear stress less effectively. The physical manifestation of the high-velocity surface layer is likely to be the zone of elevated ground-ice content of ~4 m thickness observed in the Adventdalen boreholes of Gilbert et al. (2018). This zone is rich in void filling ice, lenticular and massive solid bodies of ice that macroscopically strengthen the dominantly loess sediments (Gilbert et al., 2018), leading to relatively high shear wave velocity and a relatively low Poisson's ratio.

The low velocity layer may simply reflect the absence of these stiffening ice bodies and subsequently decreased shear strength in the porous medium. However, the low velocity zone may also indicate the presence of unfrozen permafrost due to elevated salinity, recalling that permafrost is defined simply as ground that remains below 0°C over at least two consecutive years, but does not imply that the ground is in fact frozen. This interpretation is supported by the high Poisson's ratio of the lower layer, since according to Skvortsov et al. (2014) a Poisson's ratio of 0.45-0.46 represents a threshold between frozen and unfrozen states for water-saturated soils, irrespective of composition, temperature and salinity. Unfrozen saline permafrost has also been interpreted in Adventdalen below the Holocene marine limit based on nuclear magnetic

resonance and controlled source audio-magnetotelluric data (Keating et al., 2018), which includes the study site. On balance, we conclude that unfrozen saline permafrost is the most likely explanation for the observed low velocity zone.

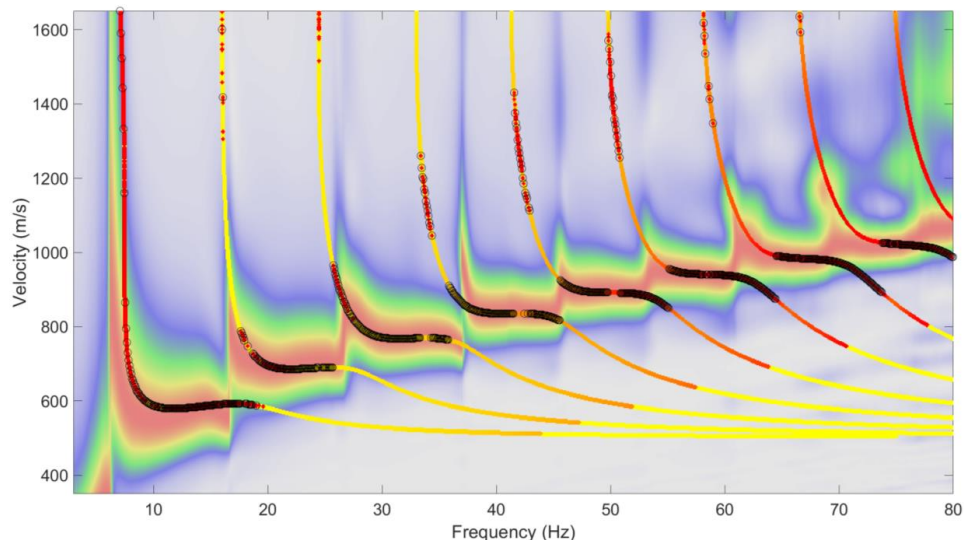


Figure 16: Spring field campaign best qualitative fit theoretical dispersion curves, based on a simple 3 layer horizontal model (see Table 1). Dispersion spectrum corresponds to event recorded 2-May 06:51, displayed with linear colour scaling.

In Figure 16 we see that the theoretical dispersion curves fit the experimental data recorded in spring remarkably well, given our very simplistic layer model. Figure 17 illustrate that the fit between model and experimental data is somewhat poorer for the autumn, although good overall fit was still achieved. Reasons for this contrast may include that the cryoseisms were stronger in spring due to colder temperatures and a more advanced state of freezing leading to a more broadband source signal. Alternately, the ground may have been more heterogeneous in the autumn, as indicated by interspersed ponds of unfrozen water and ice observed at the study site when deploying geophones in September compared with a relatively homogeneous frozen landscape with thin snow cover in March. This increased heterogeneity may affect the experimentally recorded events either via attenuation of the surface waves between source and receiver or by heterogeneities across the geophone array itself leading to decreased coherency.

It was difficult to fit the steep phase velocity gradients at the frequencies where the ground response transitions from one wave mode to another using our drastically simplified layer

model (particularly noticeable for modes 3-6 in Figure 16). We have not investigated this phenomenon in detail but hypothesise that some additional degree of freedom such as allowing for velocity gradients within layers may be required to improve this aspect of the fit.

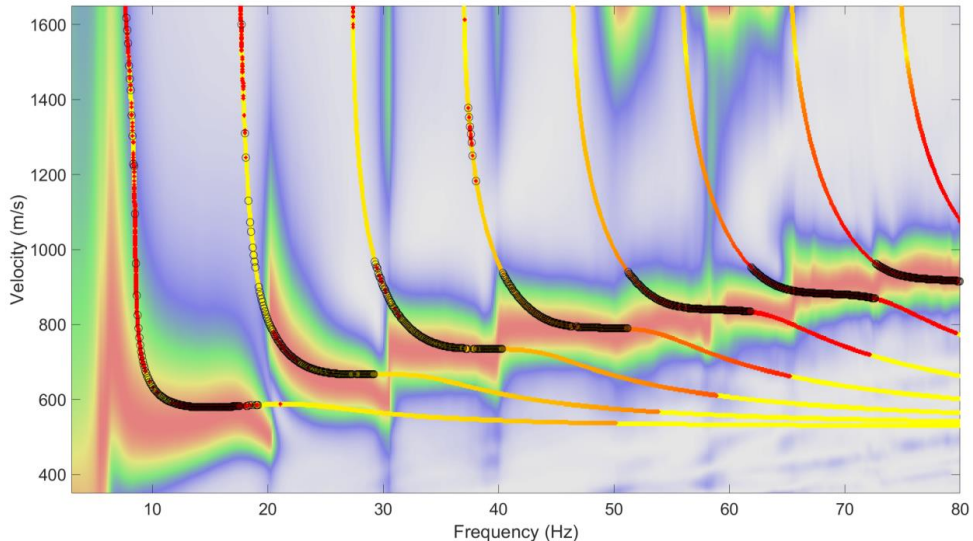


Figure 17: Autumn field campaign best qualitative fit theoretical dispersion curves, based on a simple 3 layer horizontal model (see Table 1). Dispersion spectrum corresponds to event recorded 27-Oct 12:27, displayed with linear colour scaling.

5 Conclusion

We present a methodology designed to isolate transient seismic events in passive records and thereby estimate their unknown source location and image their phase velocity dispersion. The spatial association of the source positions with a well-known frost polygon area along an elevated river-terrace in Adventdalen, together with temporal correlation with periods of rapidly changing air temperature, indicates that these events are likely cryoseisms. The phase velocity dispersion of these cryoseisms furthermore allows us to infer the subsurface structure of the permafrost and detect changes between seasons. A high-velocity solid-frozen surface layer overlying a slower and softer layer leads to a complex multimodal dispersion pattern that is familiar from previous studies of pavements. The uppermost part of the permafrost appears to be measurably softer during the autumn than the spring, implying that this methodology may also have the potential to detect changes in an inter-annual monitoring context. A future field

campaign recording continuously over an entire freeze season would, for example, give a more complete picture of the spatiotemporal occurrence of cryoseisms. Alternatively, our methodology could be applied for other locations with suitable seismic sources, such as on or adjacent to glaciers.

6 Acknowledgments

This research is funded by the University of Tromsø - The Arctic University of Norway, by the ARCEX partners and by the Research Council of Norway through grant number 228107.

7 References

- Bandt, C. and Pompe, B.: Permutation entropy: a natural complexity measure for time series, *Physical review letters*, 88, 174102, 2002.
- Barosh, P. J.: Frostquakes in New England, *Engineering geology*, 56, 389-394, 2000.
- Battaglia, S. M., Changnon, D., Changnon, D., and Hall, D.: Frost quake events and changing wintertime air mass frequencies in southeastern Canada, Working Paper, Northern Illinois University. doi: 10.13140/RG.2.2.22351.48803, 2016.
- Cable, S., Elberling, B., and Kroon, A.: Holocene permafrost history and cryostratigraphy in the High-Arctic Adventdalen Valley, central Svalbard, *Boreas*, 47, 423-442, 2018.
- Chillara, V. K. and Lissenden, C. J.: Review of nonlinear ultrasonic guided wave nondestructive evaluation: theory, numerics, and experiments, *Optical Engineering*, 55, 011002, 2015.
- Christiansen, H. H., Etzelmüller, B., Isaksen, K., Juliussen, H., Farbrot, H., Humlum, O., Johansson, M., Ingeman-Nielsen, T., Kristensen, L., and Hjort, J.: The thermal state of permafrost in the Nordic area during the International Polar Year 2007–2009, *Permafrost and Periglacial Processes*, 21, 156-181, 2010.
- Christiansen, H. H., Matsuoka, N., and Watanabe, T.: Progress in understanding the dynamics, internal structure and palaeoenvironmental potential of ice wedges and sand wedges, *Permafrost and Periglacial Processes*, 27, 365-376, 2016.
- Dou, S., Nakagawa, S., Dreger, D., and Ajo-Franklin, J.: An effective-medium model for P-wave velocities of saturated, unconsolidated saline permafrost, *Geophysics*, 82, EN33-EN50, 2017.
- El-Gohary, M. and McNames, J.: Establishing causality with whitened cross-correlation analysis, *IEEE transactions on biomedical engineering*, 54, 2214-2222, 2007.

- Foti, S., Hollender, F., Garofalo, F., Albarello, D., Asten, M., Bard, P.-Y., Comina, C., Cornou, C., Cox, B., and Di Giulio, G.: Guidelines for the good practice of surface wave analysis: A product of the InterPACIFIC project, *Bulletin of Earthquake Engineering*, 16, 2367-2420, 2018.
- French, H. M.: *The periglacial environment*, John Wiley & Sons, 2017.
- Gilbert, G. L., Kanevskiy, M., and Murton, J. B.: Recent advances (2008–2015) in the study of ground ice and cryostratigraphy, *Permafrost and Periglacial Processes*, 27, 377-389, 2016.
- Gilbert, G. L., O'Neill, H. B., Nemeč, W., Thiel, C., Christiansen, H. H., and Buylaert, J. P.: Late Quaternary sedimentation and permafrost development in a Svalbard fjord-valley, Norwegian high Arctic, *Sedimentology*, 65, 2531-2558, 2018.
- Humlum, O., Instanes, A., and Sollid, J. L.: Permafrost in Svalbard: a review of research history, climatic background and engineering challenges, *Polar research*, 22, 191-215, 2003.
- Johansen, T. A., Digranes, P., van Schaack, M., and Lønne, I.: Seismic mapping and modeling of near-surface sediments in polar areas, *Geophysics*, 68, 566-573, 2003.
- Kanevskiy, M., Shur, Y., Fortier, D., Jorgenson, M., and Stephani, E.: Cryostratigraphy of late Pleistocene syngenetic permafrost (yedoma) in northern Alaska, Itkillik River exposure, *Quaternary research*, 75, 584-596, 2011.
- Keating, K., Binley, A., Bense, V., Van Dam, R. L., and Christiansen, H. H.: Combined geophysical measurements provide evidence for unfrozen water in permafrost in the adventdalen valley in Svalbard, *Geophysical Research Letters*, 45, 7606-7614, 2018.
- Knopoff, L.: A matrix method for elastic wave problems, *Bulletin of the Seismological Society of America*, 54, 431-438, 1964.
- Lachenbruch, A. H.: *Mechanics of thermal contraction cracks and ice-wedge polygons in permafrost*, Geological Society of America, 1962.
- Le Feuvre, M., Joubert, A., Leparoux, D., and Cote, P.: Passive multi-channel analysis of surface waves with cross-correlations and beamforming. Application to a sea dike, *J Appl Geophys*, 114, 36-51, 2015.
- Leung, A. C., Gough, W. A., and Shi, Y.: Identifying frostquakes in Central Canada and neighbouring regions in the United States with social media. In: *Citizen Empowered Mapping*, Springer, 2017.
- Lowe, M. J.: Matrix techniques for modeling ultrasonic waves in multilayered media, *IEEE transactions on ultrasonics, ferroelectrics, and frequency control*, 42, 525-542, 1995.
- Lønne, I.: Faint traces of high Arctic glaciations: an early Holocene ice-front fluctuation in Bolterdalen, Svalbard, *Boreas*, 34, 308-323, 2005.

-
- Mackay, J. R.: The direction of ice-wedge cracking in permafrost: downward or upward?, *Canadian Journal of Earth Sciences*, 21, 516-524, 1984.
- Matsuoka, N., Christiansen, H. H., and Watanabe, T.: Ice-wedge polygon dynamics in Svalbard: Lessons from a decade of automated multi-sensor monitoring, *Permafrost and Periglacial Processes*, 29, 210-227, 2018.
- Nikonov, A.: Frost quakes as a particular class of seismic events: Observations within the East-European platform, *Izvestiya, Physics of the Solid Earth*, 46, 257-273, 2010.
- O'Neill, H. B. and Christiansen, H. H.: Detection of ice wedge cracking in permafrost using miniature accelerometers, *Journal of Geophysical Research: Earth Surface*, 123, 642-657, 2018.
- O'Neill, H. B. and Burn, C. R.: Physical and temporal factors controlling the development of near-surface ground ice at Illisarvik, western Arctic coast, Canada, *Canadian Journal of Earth Sciences*, 49, 1096-1110, 2012.
- Park, C., Miller, R., Laflen, D., Neb, C., Ivanov, J., Bennett, B., and Huggins, R.: Imaging dispersion curves of passive surface waves. In: *SEG technical program expanded abstracts 2004*, Society of Exploration Geophysicists, 2004.
- Park, C. B., Miller, R. D., and Xia, J.: Imaging dispersion curves of surface waves on multi-channel record. In: *SEG Technical Program Expanded Abstracts 1998*, Society of Exploration Geophysicists, 1998.
- Park, C. B., Miller, R. D., and Xia, J.: Multichannel analysis of surface waves, *Geophysics*, 64, 800-808, 1999.
- Park, C. B., Miller, R. D., Xia, J., and Ivanov, J.: Multichannel analysis of surface waves (MASW)—active and passive methods, *The Leading Edge*, 26, 60-64, 2007.
- Rose, J. L.: Ultrasonic guided waves in structural health monitoring, 2004, 14-21.
- Ryden, N. and Lowe, M. J.: Guided wave propagation in three-layer pavement structures, *The Journal of the Acoustical Society of America*, 116, 2902-2913, 2004.
- Ryden, N., Park, C. B., Ulriksen, P., and Miller, R. D.: Multimodal approach to seismic pavement testing, *Journal of geotechnical and geoenvironmental engineering*, 130, 636-645, 2004.
- Schmidt, H. and Jensen, F. B.: A full wave solution for propagation in multilayered viscoelastic media with application to Gaussian beam reflection at fluid–solid interfaces, *The Journal of the Acoustical Society of America*, 77, 813-825, 1985.
- Sergeant, A., Chmiel, M., Lindner, F., Walter, F., Roux, P., Chaput, J., Gimbert, F., and Mordret, A.: On the Green's function emergence from interferometry of seismic wave fields

generated in high-melt glaciers: implications for passive imaging and monitoring, *The Cryosphere*, 14, 1139-1171, 2020.

Skvortsov, A., Sadurtdinov, M., and Tsarev, A.: Seismic criteria for indentifying frozen soil, *Methods*, 18, 75-80, 2014.

Unakafova, V. and Keller, K.: Efficiently measuring complexity on the basis of real-world data, *Entropy*, 15, 4392-4415, 2013.

3. Synthesis

This study has evaluated several aspects related to the use of seismic to map and monitor the Arctic. In this synthesis chapter, the main findings of each paper are first summarized and put into a common context related to the objectives. Finally, some interesting future research directions are discussed.

3.1. Main findings

The main outcomes from each paper can be summarized as follows:

- In Paper 1, we computed the sound pressure levels and sound exposure levels at hydrophones in shallow water during seismic experiments with detonating cords on top of sea ice and air guns below the ice. We then reviewed the sound levels for possible impacts on the hearing of seals. We found that a seismic survey of this size is most likely not physically injurious due to the low hearing sensitivity of seals to the seismic frequencies, in addition to the rapid decrease in sound level with increasing distance from the source. We found the highest sound levels for both types of sources at frequencies that seals cannot hear well (<700 Hz). Temporary behavior change may occur, but no indication of permanent disruption to the population of seals was observed.
- In Paper 2, we combined heat flux, rock physics, and seismic modeling to estimate the change in effective elastic properties of permafrost related to various future climate scenarios in the Arctic. We found that elastic and seismic properties of (partly) frozen unconsolidated near-surface saline sediments strongly depend on heat flux into the subsurface, and vary both seasonally and between different climate scenarios. Seismic data obtained by full waveform modeling and real experiments in Adventdalen showed time-lapse effects that can be related to varying surface temperatures.
- In Paper 3, we presented synthetic and real seismic time-lapse data acquired at the same study site, but at different times of the year. Comparison of the seismic records and dispersion images revealed time-lapse effects that were related to thawing. In particular, the surface wave dispersion appeared to be sensitive to the

degree of freezing in unconsolidated sediments. Analyses of dispersion images basically provide trends in the stiffness gradient. This further demonstrated the potential of using surface seismic for Arctic climate monitoring.

- In Paper 4, we analyzed passive seismic data acquired in Adventdalen during spring and early autumn. We observed a series of transient seismic events that contained a high proportion of surface wave energy, and that could produce high-quality dispersion images through an innovative source localization approach followed by cross-correlation beamforming. We found that the timing of these events correlated with periods of rapidly changing air temperature, and therefore identified them as frost quakes. The dispersion patterns resembled those observed in pavement studies, and also varied between spring and autumn, indicating that seasonal permafrost thawing can be resolved from passive seismic data.

The results of Paper 1 are of value particularly when it comes to the practical aspects of planning seismic experiments in the Arctic, while the remaining papers focus more on the scientific value of using seismic to map and monitor Arctic near-surface sediments. Hence, this study addresses both logistical and scientific challenges related to using seismic in the Arctic.

The motivation behind carrying out this project was that geophysical mapping and monitoring of the Arctic subsurface is interesting for environmental and economic reasons, but we lack knowledge about several aspects related to this. We here mainly focus on the environmental aspects related to the near-surface sediments, although the results of Paper 1 are independent of the actual aim of the experiment. The first objective was defined to address the lack of knowledge about the impact of seismic experiments on animal life. This is one of the concerns that have been raised by authorities when evaluating applications for seismic experiments on Svalbard. Since we conclude in Paper 1 that seismic experiments of this size do not cause hearing damage in seals, the study motivates continued studies on the use of seismic in the Arctic. The second objective was defined to address the lack of knowledge about monitoring of permafrost degradation. Several geophysical methods have previously been used for mapping of permafrost (Kneisel et al., 2008; Briggs et al., 2016; Keating et al., 2018), but no non-intrusive method has by itself been able to accurately determine the ice saturation in

saline near-surface sediments. Since seismic surface wave methods have been successful in near-surface characterization at sub-Arctic locations, we wanted to investigate whether these can be useful in permafrost areas as well. To address this topic, we first theoretically investigated the impact of heat flux on effective rock physics properties in Paper 2, and then studied the actual time-lapse effect in seismic data in Paper 3 and Paper 4. Although our real seismic data cannot be used to directly study the effects of long-term climate change, the observed seasonal time-lapse effects indicate that seismic data will also resolve longer-term alterations in surface temperature.

To summarize: Paper 1 considers whether using seismic in the Arctic is **safe**. Paper 2 considers whether using seismic for near-surface climate monitoring in the Arctic has any **theoretical scientific basis**. Finally, Papers 3 and 4 consider whether it is actually possible to use seismic data to detect variations in seismic properties due to surface temperature variation, i.e., does it **work in practice**.

3.2. Outlook

Based on the results of this study, several interesting future research directions have been identified. Three of these are discussed in more detail here:

1. *Further studies on ideal experiment design for obtaining high resolution data with minor impact on Arctic environment and fauna*

As repeatedly pointed out throughout this thesis, acquisition of seismic data in Arctic environments needs to fulfill two requirements: it has to be environmentally friendly in the sense of having minor impact on the surroundings, while at the same time providing useful, high-quality seismic data. Optimizing the balance between these two aspects deserves attention in future research.

First, further studies on the impact of seismic experiments on animals are of interest. Although Paper 1 concluded that seismic studies of the size considered here do not damage the hearing of seals, these results do not necessarily apply to other Arctic animals. For studies on the impact of seismic on marine mammals, we should be able to follow a similar approach to the one applied in Paper 1. Since Paper 1 was published, the weighting functions that were applied in Paper 1 (Southall et al., 2007) have been

updated (Southall et al., 2019) to be more precise and better distinguish between animal species, but this does not affect the conclusions of Paper 1. For considering the effect on terrestrial animals (which might be more relevant in the context of using seismic for climate monitoring), the approach would have to be modified to account for the fact that geophones measure particle velocity rather than pressure, for example by also utilizing microphones during the experiments.

Second, further studies on ideal acquisition design for obtaining high-quality data are of interest. As demonstrated in both this and other studies, the presence of frozen ground, glaciers, or floating ice leads to strong and highly dispersive surface waves. Depending on the purpose of the experiment, we might want to remove or enhance these, and studies on both aspects are of interest. During reflection seismic surveys, we prefer to acquire data without surface waves (Kearey et al., 2002). Although the topic of removing these either through acquisition design (Rendleman and Levin, 1990; Johansen et al., 2019) or through processing (Henley, 2007) has been the focus of several studies over many decades, obtaining reflection and refraction seismic data with a high signal-to-noise ratio remains a challenge in Arctic environments. In surface wave studies on the other hand, we would rather enhance the surface waves. Arctic surface wave studies is an appealing future research topic due to the dominating surface waves in such data. Although many studies on optimal surface wave survey design are already available (see the review by Socco et al., 2010), studies on ideal choice of source type and offset are of interest because sources may generate different interfering waves, and frequencies may be dampened differently with distance. Also, we usually use vertical component geophones to acquire Rayleigh waves in surface wave studies, but by including horizontal component receivers as well, we can acquire Love waves or horizontally polarized S-waves (SH-waves) that can be simultaneously analyzed.

By also including the environmental impact of the various sources and receivers as a factor when evaluating different acquisition designs, we obtain valuable knowledge of how we should conduct future Arctic seismic surveys in the best possible manner. Nevertheless, the success of surface wave methods for near-surface characterization does not only depend on the acquisition, but also on the data processing and inversion

(Socco et al., 2010). Provided that high-quality surface wave data can be acquired as described here, careful analysis of the data is still necessary for extracting accurate soil parameters. This takes us to the next interesting future research topic:

2. Improving the processing and inversion schemes for obtaining elastic and physical parameters from surface seismic data

In this study, we have demonstrated the potential of using seismic data to detect temporal changes in the seismic wavefield caused by surface temperature variations (Papers 2, 3, and 4). To use seismic data for climate monitoring of near-surface sediments, the natural next step involves quantification of how much the elastic and physical properties have changed between the seismic experiments. To accomplish this, we first need to invert the seismic observables to elastic properties. Next, we need to invert the elastic properties to physical parameters. Several aspects related to these topics can be investigated in future studies; some are described in the following paragraphs.

Before the seismic inversion can be carried out, the data have to be properly processed to be able to extract correct dispersion curves and identify which modes are dominant over the frequency range. Future research related to processing of surface wave data can for example focus on air wave removal that does not affect the dispersion curve. Additionally, most surface wave studies (including Papers 3 and 4) focus on the velocity dispersion, but additional analysis of the attenuation dispersion can provide more information.

The classical seismic surface wave inversion consists of two parts. The first is a forward modeling part where modal curves are computed for a given subsurface model. During forward modeling, we represent the subsurface by a stack of elastic or viscoelastic layers, and based on this we form an eigenvalue problem. The solution is a multivalued function of frequency, which represents the modal curves (Socco et al., 2010). The most commonly used method for solving this eigenvalue problem, the transfer matrix method, provides no information about how energy is distributed along modes. This is a problem when higher modes are dominant, which is typically the case in Arctic environments. Hence, solving the eigenvalue problem including higher modes is an interesting topic that has been the focus of several studies (Maraschini et al., 2010; Pan et al., 2013). This

is to some extent implemented in Paper 4, where we use the global matrix method (Ryden and Lowe, 2004) and compute the magnitude of displacement at the top ground interface for the different wave modes for simple three-layer models.

The second part of the classical inversion involves the use of an algorithm for iteratively minimizing the misfit between picked dispersion curves and computed modal curves. The inversion algorithms are typically divided into two groups: local search methods (LSM's) which search for a solution in the vicinity of the initial model, and global search methods (GSM's) which systematically compute a large amount of solutions and afterwards look for a proper solution among these models. While LSM's are fast and produce a unique solution, GSM's are computationally expensive and represent a non-unique problem. However, the solution of LSM's strongly depends on our choice of initial model parameters, while for GSM's there is no linearity between the initial model and the solution (Socco et al., 2010). If surface wave methods are going to be a helpful tool in Arctic climate monitoring, the inversion methods have to be both accurate and efficient. The usefulness of the method is reduced if the inversion process requires massive computing resources. Improving the efficiency of inversion algorithms is an appealing research direction that has been a focus of recent studies (Lei et al., 2019), while an equally appealing and less frequently studied topic is on improving the picking of good initial models by developing statistical or empirical models for Arctic environments.

Yet another issue is related to lateral site variations. These may introduce artefacts in the dispersion curve, and several recent studies are investigating how to account for lateral heterogeneities in the inversion process. In particular there are promising studies on replacing the classical seismic surface wave inversion with full waveform inversion (Dou and Ajo-Franklin, 2014; Solano et al., 2014; Groos et al., 2017) or 2D/3D wave equation dispersion inversion (Liu et al., 2018; Zhang and Alkhalifah, 2019).

The last step of obtaining soil parameters from seismic data involves inversion of elastic properties to physical properties. This represents an underdetermined problem because several combinations of physical properties can produce a similar response (Johansen et al., 2013; Bredesen et al., 2015). For example, in Paper 2, we demonstrated that elastic

and seismic properties vary with time when surface temperature varies, but we also demonstrated that these properties are sensitive to salinity and saturation of the sediments. Thus, it follows that knowledge about the local pore fluid conditions is essential for quantifying how much thawing has occurred in a given time period. Hence, even though surface seismic data can detect even small changes in ice saturation, it may be challenging to use seismic data by itself for Arctic climate monitoring. This leads us to the last research direction discussed here:

3. *Integrating surface seismic methods with other geophysical methods for enhanced climate monitoring of permafrost areas*

Future research on climate monitoring of Arctic sediments should focus on integrating the surface seismic method presented here with other geophysical methods, such as geo-electrical, electromagnetic, or other seismic methods (Kneisel et al., 2008; Wu et al., 2017). In their review of surface wave methods, Socco et al. (2010) highlight that joint inversion with other geophysical methods increases the chance of obtaining an accurate and reliable soil model when using surface wave methods. Keating et al. (2018) successfully used surface nuclear magnetic resonance to detect unfrozen saline water in Adventdalen, which is a challenge with many other geophysical methods. Further, by combining active and passive seismic data, we can expand the frequency range with useful energy, for example by simultaneous analysis of the data used in Papers 2 and 4. Dispersion curves have higher resolution at low frequencies (<50 Hz) in passive data, while they can be followed to higher frequencies and analyzed for dampening effects in active data. Analysis of Love or SH waves following a similar approach as for Rayleigh waves can also be useful (Li et al., 2019). Distributed acoustic sensors are sensitive to surface waves, and could be useful for detecting small changes in the surface waves due to thawing (Ajo-Franklin et al., 2017). Further, geological information from boreholes can help constrain the model and build the initial model for inversion.

References used in the introduction and synthesis

- Ajo-Franklin, J., Dou, S., Daley, T., Freifeld, B., Robertson, M., Ulrich, C., ... & Wagner, A. (2017). Time-lapse surface wave monitoring of permafrost thaw using distributed acoustic sensing and a permanent automated seismic source. In *SEG Technical Program Expanded Abstracts 2017* (pp. 5223-5227). Society of Exploration Geophysicists.
- Arendt, A., Bolch, T., Cogley, J. G., Gardner, A., Hagen, J. O., Hock, R., ... & Radic, V. (2012). Randolph Glacier Inventory [v1. 0]: A Dataset of Global Glacier Outlines. Global Land Ice Measurements from Space, Boulder Colorado, USA [Dataset].
- Bergmann, L. (1948). *Ultrasonics and their Scientific and Technical Applications*. Hoboken, New Jersey: John Wiley & Sons.
- Berryman, J. G. (1980a). Long-wavelength approximation in composite elastic media I. Spherical inclusions. *The Journal of the Acoustical Society of America*, 68(6), 1809–1819.
- Berryman, J. G. (1980b). Long-wavelength propagation in composite elastic media II. Ellipsoidal inclusions. *The Journal of the Acoustical Society of America*, 68(6), 1820–1831.
- Biot, M. A. (1956). Theory of propagation of elastic waves in a fluid-saturated porous solid. II. Higher frequency range. *The Journal of the Acoustical Society of America*, 28(2), 179-191.
- Bredesen, K., Jensen, E. H., Johansen, T. A., & Avseth, P. (2015). Quantitative seismic interpretation using inverse rock physics modelling. *Petroleum Geoscience*, 21(4), 271-284.
- Briggs, M. A., Campbell, S., Nolan, J., Walvoord, M. A., Ntarlagiannis, D., Day-Lewis, F. D., & Lane, J. W. (2017). Surface geophysical methods for characterising frozen ground in transitional permafrost landscapes. *Permafrost and Periglacial Processes*, 28(1), 52-65.
- Christiansen, H. H., Etzelmüller, B., Isaksen, K., Juliussen, H., Farbro, H., Humlum, O., ... & Holmlund, P. (2010). The thermal state of permafrost in the nordic area during the international polar year 2007–2009. *Permafrost and Periglacial Processes*, 21(2), 156-181.
- Comyn-Platt, E., Hayman, G., Huntingford, C., Chadburn, S. E., Burke, E. J., Harper, A. B., ... & Gedney, N. (2018). Carbon budgets for 1.5 and 2 C targets lowered by natural wetland and permafrost feedbacks. *Nature Geoscience*, 11(8), 568-573.
- Cooke, D., & Cant, J. (2010). Model-based Seismic Inversion: Comparing deterministic and probabilistic approaches. *CSEG Recorder*, 35(4), 29-39.
- Cormier, Z. (2019, August 27). Why the Arctic is smouldering. *BBC Future*. <https://www.bbc.com/future/article/20190822-why-is-the-arctic-on-fire>

- Dou, S., & Ajo-Franklin, J. B. (2014). Full-wavefield inversion of surface waves for mapping embedded low-velocity zones in permafrost. *Geophysics*, 79(6), EN107-EN124.
- Dou, S., Nakagawa, S., Dreger, D., & Ajo-Franklin, J. (2016). A rock-physics investigation of unconsolidated saline permafrost: P-wave properties from laboratory ultrasonic measurements. *Geophysics*, 81(1), WA233-WA245.
- Dou, S., Nakagawa, S., Dreger, D., & Ajo-Franklin, J. (2017). An effective-medium model for P-wave velocities of saturated, unconsolidated saline permafrost. *Geophysics*, 82(3), EN33-EN50.
- Dvorkin, J., Berryman, J., & Nur, A. (1999). Elastic moduli of cemented sphere packs. *Mechanics of Materials*, 31(7), 461-469.
- Dvorkin, J., Nur, A., & Yin, H. (1994). Effective properties of cemented granular materials. *Mechanics of Materials*, 18(4), 351-366.
- Dvorkin, J., & Nur, A. (1996). Elasticity of high-porosity sandstones: Theory for two North Sea data sets. *Geophysics*, 61(5), 1363-1370.
- Fraser, A. (2019, September 03). On the front lines of climate change in the world's northernmost town. *Reuters*. <https://www.reuters.com/article/us-climate-change-svalbard-widerimage/on-the-front-lines-of-climate-change-in-the-worlds-northernmost-town-idUSKCN1VO19M>
- French, H. M. (2017). *The periglacial environment*. Hoboken, New Jersey: John Wiley & Sons.
- Gassmann, F. (1951). Elastic waves through a packing of spheres. *Geophysics*, 16(4), 673-685.
- Gausland, I. (2000). Impact of seismic surveys on marine life. *The Leading Edge*, 19(8), 903-905.
- Gautier, D. L., Bird, K. J., Charpentier, R. R., Grantz, A., Houseknecht, D. W., Klett, T. R., ... & Sørensen, K. (2009). Assessment of undiscovered oil and gas in the Arctic. *Science*, 324(5931), 1175-1179.
- Gordon, J., Gillespie, D., Potter, J., Frantzis, A., Simmonds, M. P., Swift, R., & Thompson, D. (2003). A review of the effects of seismic surveys on marine mammals. *Marine Technology Society Journal*, 37(4), 16-34.
- Groos, L., Schäfer, M., Forbriger, T., & Bohlen, T. (2017). Application of a complete workflow for 2D elastic full-waveform inversion to recorded shallow-seismic Rayleigh waves. *Geophysics*, 82(2), R109-R117.
- Hauck, C., & Kneisel, C. (2008). *Applied geophysics in periglacial environments*. Cambridge, UK: Cambridge University Press.

Hashin, Z., & Shtrikman, S. (1963). A variational approach to the theory of the elastic behaviour of multiphase materials. *Journal of the Mechanics and Physics of Solids*, 11(2), 127-140.

Heleniak, T. and Bogoyavlenskiy, D. (2014). Arctic populations and migration. In J. N. Larsen & G. Fondahl (Eds.), *Arctic human development report: Regional processes and global linkages*. Copenhagen, Denmark: Nordic council of ministers.

Henley, D. C. (2007). Attenuating the ice flexural wave on arctic seismic data. In *69th EAGE Conference and Exhibition-Workshop Package*, (pp. cp-29). European Association of Geoscientists & Engineers.

Hilbich, C. (2010). Time-lapse refraction seismic tomography for the detection of ground ice degradation. *The Cryosphere*, 4(3), 243-259.

Hjort, J., Karjalainen, O., Aalto, J., Westermann, S., Romanovsky, V. E., Nelson, F. E., ... & Luoto, M. (2018). Degrading permafrost puts Arctic infrastructure at risk by mid-century. *Nature Communications*, 9(1), 1-9.

Hogenboom, M. (2017, February 24). In Siberia there is a huge crater and it is getting bigger. *BBC Earth*. <http://www.bbc.com/earth/story/20170223-in-siberia-there-is-a-huge-crater-and-it-is-getting-bigger>

Humpert, M. (2019, December 05). *High North News*. <https://www.highnorthnews.com/en/greenlands-kangerlussuaq-airport-close-major-commercial-traffic-2024-due-climate-change>

IEA (2019). World Energy Outlook 2019, *International Energy Association*, Paris, France.

IPCC (2013). Climate Change 2013: The Physical Science Basis. Contribution of Working Group I to the Fifth Assessment Report of the Intergovernmental Panel on Climate Change [Stocker, T.F., D. Qin, G.-K. Plattner, M. Tignor, S.K. Allen, J. Boschung, A. Nauels, Y. Xia, V. Bex and P.M. Midgley (Eds.)]. *Cambridge University Press*, Cambridge, United Kingdom and New York, NY, USA, 1535 pp.

IPCC (2014). Climate Change 2014: Synthesis Report. Contribution of Working Groups I, II and III to the Fifth Assessment Report of the Intergovernmental Panel on Climate Change [Core Writing Team, R.K. Pachauri and L.A. Meyer (Eds.)]. *IPCC*, Geneva, Switzerland, 151 pp.

Johansen, T. A., Digranes, P., van Schaack, M., & Lønne, I. (2003). Seismic mapping and modeling of near-surface sediments in polar areas. *Geophysics*, 68(2), 566-573.

Johansen, T. A., Jensen, E. H., Mavko, G., & Dvorkin, J. (2013). Inverse rock physics modeling for reservoir quality prediction. *Geophysics*, 78(2), M1-M18.

Johansen, T. A., Ruud, B. E., Bakke, N. E., Riste, P., Johannessen, E. P., & Henningsen, T. (2011). Seismic profiling on Arctic glaciers. *First Break*, 29(2), 65-71.

- Johansen, T. A., Ruud, B. O., Tømmerbakke, R., & Jensen, K. (2019). Seismic on floating ice: data acquisition versus flexural wave noise. *Geophysical Prospecting*, *67*(3), 532-549.
- Johansen, T. A., & Ruud, B. O. (2020). Characterization of seabed properties from Scholte waves acquired on floating ice on shallow water. *Near Surface Geophysics*, *18*(1), 49-59.
- Kearey, P., Brooks, M., & Hill, I. (2002). *An Introduction to Geophysical Exploration*. Malden, MA: Blackwell Publishing.
- Keating, K., Binley, A., Bense, V., Van Dam, R. L., & Christiansen, H. H. (2018). Combined geophysical measurements provide evidence for unfrozen water in permafrost in the Adventdalen valley in Svalbard. *Geophysical Research Letters*, *45*(15), 7606-7614.
- Kneisel, C., Hauck, C., Fortier, R., & Moorman, B. (2008). Advances in geophysical methods for permafrost investigations. *Permafrost and Periglacial Processes*, *19*(2), 157-178.
- Kottke, M., Grieser, J., Beck, C., Rudolf, B., & Rubel, F. (2006). World map of the Köppen-Geiger climate classification updated. *Meteorologische Zeitschrift*, *15*(3), 259-263.
- Krebes, E. S. (2004). Seismic forward modeling. *CSEG Recorder*, *30*, 28-39.
- Landau, L. D., Kosevich, A., Pitaevskii, L. P., & Lifshitz, E. M. (2012). *Theory of elasticity*. Oxford, UK: Butterworth-Heinemann.
- Lavelle, M. (2010, April 07). Offshore Energy Clash Over Undersea Sound. *National Geographic*. <https://www.nationalgeographic.com/news/2010/4/100407-energy-undersea-sound/>
- Lei, Y., Shen, H., Li, X., Wang, X., & Li, Q. (2019). Inversion of Rayleigh wave dispersion curves via adaptive GA and nested DLS. *Geophysical Journal International*, *218*(1), 547-559.
- Lewkowicz, A. G., & Way, R. G. (2019). Extremes of summer climate trigger thousands of thermokarst landslides in a High Arctic environment. *Nature Communications*, *10*(1), 1-11.
- Li, J., Hanafy, S., Liu, Z., & Schuster, G. T. (2019). Wave-equation dispersion inversion of Love waves. *Geophysics*, *84*(5), R693-R705.
- Liu, H. P., Anderson, D. L., & Kanamori, H. (1976). Velocity dispersion due to anelasticity; implications for seismology and mantle composition. *Geophysical Journal International*, *47*(1), 41-58.
- Liu, Z., Li, J., Hanafy, S. M., & Schuster, G. (2018). 3D wave-equation dispersion inversion of surface waves. In *SEG Technical Program Expanded Abstracts 2018* (pp. 4733-4737). Society of Exploration Geophysicists.

-
- Malakoff, D. (2002, October 25). Suit ties whale deaths to research cruise. *Science News*. <https://science.sciencemag.org/content/298/5594/722/tab-pdf>
- Malischewsky, P. G. (2005). Comparison of approximated solutions for the phase velocity of Rayleigh waves (Comment on ‘Characterization of surface damage via surface acoustic waves’). *Nanotechnology*, 16(6), 995.
- Maraschini, M., Ernst, F., Foti, S., & Socco, L. V. (2010). A new misfit function for multimodal inversion of surface waves. *Geophysics*, 75(4), G31-G43.
- Matsushima, J., Suzuki, M., Kato, Y., & Rokugawa, S. (2016). Ultrasonic measurements of attenuation and velocity of compressional and shear waves in partially frozen unconsolidated sediment and synthetic porous rock. *Geophysics*, 81(2), D141-D153.
- Mavko, G., Mukerji, T., & Dvorkin, J. (2009). *The rock physics handbook*. Cambridge, UK: Cambridge University Press.
- Mindlin, R. D. (1949). Compliance of elastic bodies in contact. *Journal of Applied Mechanics*, 16, 259-268.
- The Moscow Times (2020, May 29). ‘Zombie’ Wildfires Threaten Arctic Russia, Scientists Warn. *The Moscow Times*. <https://www.themoscowtimes.com/2020/05/29/zombie-wildfires-threaten-arctic-russia-scientists-warn-a70416>
- Murton, J. B., Edwards, M. E., Lozhkin, A. V., Anderson, P. M., Savvinov, G. N., Bakulina, N., ... & Goslar, T. (2017). Preliminary paleoenvironmental analysis of permafrost deposits at Batagaika megaslump, Yana Uplands, northeast Siberia. *Quaternary Research*, 87(2), 314-330.
- NCCS (2019). Climate in Svalbard 2100 – a knowledge base for climate adaptation, [I. Hanssen-Bauer, E. J. Førland, H. Hisdal, S. Mayer, A. B. Sandø, A. Sorteberg, (Eds.)]: *The Norwegian Centre for Climate Services*, report no. M-1242, 1/2019, 1055 pp.
- NMFS (2016). Technical Guidance for Assessing the Effects of Anthropogenic Sound on Marine Mammal Hearing: Underwater Acoustic Thresholds for Onset of Permanent and Temporary Threshold Shifts. *National Marine Fisheries Services, U.S. Department of Commerce, NOAA*. NOAA Technical Memorandum NMFS-OPR-55, 178 pp.
- Overland, J. E., Wang, M., Walsh, J. E., & Stroeve, J. C. (2014). Future Arctic climate changes: Adaptation and mitigation time scales. *Earth's Future*, 2(2), 68-74.
- Pan, Y., Xia, J., Gao, L., Shen, C., & Zeng, C. (2013). Calculation of Rayleigh-wave phase velocities due to models with a high-velocity surface layer. *Journal of Applied Geophysics*, 96, 1-6.

- Pérez Solano, C. A., Donno, D., & Chauris, H. (2014). Alternative waveform inversion for surface wave analysis in 2-D media. *Geophysical Journal International*, 198(3), 1359-1372.
- Potter, R. W., Clynne, M. A., & Brown, D. L. (1978). Freezing point depression of aqueous sodium chloride solutions. *Economic Geology*, 73(2), 284-285.
- Potter, C. (2018). Ecosystem carbon emissions from 2015 forest fires in interior Alaska. *Carbon Balance and Management*, 13(1), 2.
- Raynolds, M. K., Walker, D. A., Ambrosius, K. J., Brown, J., Everett, K. R., Kanevskiy, M., ... & Webber, P. J. (2014). Cumulative geocological effects of 62 years of infrastructure and climate change in ice-rich permafrost landscapes, Prudhoe Bay Oilfield, Alaska. *Global Change Biology*, 20(4), 1211-1224.
- Rendleman, C. A., & Levin, F. K. (1990). Seismic exploration on a floating ice sheet. *Geophysics*, 55(4), 402-409.
- Reuss, A. (1929). Berechnung der fließgrenze von mischkristallen auf grund der plastizitätsbedingung für einkristalle. *ZAMM-Journal of Applied Mathematics and Mechanics/Zeitschrift für Angewandte Mathematik und Mechanik*, 9(1), 49-58.
- Ross, N., Brabham, P. J., Harris, C., & Christiansen, H. H. (2007). Internal structure of open system pingos, Adventdalen, Svalbard: the use of resistivity tomography to assess ground-ice conditions. *Journal of Environmental & Engineering Geophysics*, 12(1), 113-126.
- Ryden, N., & Lowe, M. J. (2004). Guided wave propagation in three-layer pavement structures. *The Journal of the Acoustical Society of America*, 116(5), 2902-2913.
- Schuur, E. A., McGuire, A. D., Schädel, C., Grosse, G., Harden, J. W., Hayes, D. J., ... & Natali, S. M. (2015). Climate change and the permafrost carbon feedback. *Nature*, 520(7546), 171-179.
- Schwerdtfeger, P. (1963). The thermal properties of sea ice. *Journal of Glaciology*, 4(36), 789-807.
- Serreze, M. C., & Francis, J. A. (2006). The Arctic amplification debate. *Climatic Change*, 76(3-4), 241-264.
- Sharples, J. D. (2016). The shifting geopolitics of Russia's natural gas exports and their impact on EU-Russia gas relations. *Geopolitics*, 21(4), 880-912.
- Socco, L. V., & Strobbia, C. (2004). Surface-wave method for near-surface characterization: a tutorial. *Near Surface Geophysics*, 2(4), 165-185.
- Socco, L. V., Foti, S., & Boiero, D. (2010). Surface-wave analysis for building near-surface velocity models—Established approaches and new perspectives. *Geophysics*, 75(5), 75A83-75A102.

- Southall, B. L., Bowles, A. E., Ellison, W. T., Finneran, J. J., Gentry, R. L., Greene, C. R., Jr., ... & Tyack, P. L. (2007). Marine mammal noise exposure criteria. *Aquatic Mammals*, 33(4).
- Southall, B. L., Finneran, J. J., Reichmuth, C., Nachtigall, P. E., Ketten, D. R., Bowles, A. E., ... & Tyack, P. L. (2019). Marine mammal noise exposure criteria: Updated scientific recommendations for residual hearing effects. *Aquatic Mammals*, 45(2), 125-232.
- Streletskiy, D., Anisimov, O., & Vasiliev, A. (2014). Permafrost Degradation. In W. Haerberli, W. & C. Whiteman (Eds.), *Snow and Ice-Related Hazards, Risks, and Disasters*. Amsterdam: Elsevier.
- Tchebakova, N. M., Parfenova, E., & Soja, A. J. (2009). The effects of climate, permafrost and fire on vegetation change in Siberia in a changing climate. *Environmental Research Letters*, 4(4), 045013.
- Timur, A. (1968). Velocity of compressional waves in porous media at permafrost temperatures. *Geophysics*, 33(4), 584-595.
- Tougaard, J., & Beedholm, K. (2019). Practical implementation of auditory time and frequency weighting in marine bioacoustics. *Applied Acoustics*, 145, 137-143.
- Trupp, R., Hastings, J., Cheadle, S., & Vesely, R. (2009). Seismic in arctic environs: Meeting the challenge. *The Leading Edge*, 28(8), 936-942.
- Tsuji, T., Johansen, T. A., Ruud, B. O., Ikeda, T., & Matsuoka, T. (2012). Surface-wave analysis for identifying unfrozen zones in subglacial sediments. *Geophysics*, 77(3), EN17-EN27.
- Voigt, W. (1928). *Lehrbuch der Kristallphysik (mit Ausschluss der Kristalloptik)*. Leipzig Berlin, Germany: B.G. Teubner & Ann Arbor, MI: J.W. Edwards.
- Worsley, D. (2008). The post-Caledonian development of Svalbard and the western Barents Sea. *Polar Research*, 27(3), 298-317.
- Wu, Y., Nakagawa, S., Kneafsey, T. J., Dafflon, B., & Hubbard, S. (2017). Electrical and seismic response of saline permafrost soil during freeze-thaw transition. *Journal of Applied Geophysics*, 146, 16-26.
- Yilmaz, Ö. (2001). *Seismic data analysis: Processing, inversion, and interpretation of seismic data*. Tulsa, OK: Society of Exploration Geophysicists.
- Zhang, Z. D., & Alkhalifah, T. (2019). Wave-equation Rayleigh-wave dispersion inversion using fundamental and higher modes. *Geophysics*, 84(4), EN57-EN65.
- Zhang, Y., Carey, S. K., & Quinton, W. L. (2008). Evaluation of the algorithms and parameterizations for ground thawing and freezing simulation in permafrost regions. *Journal of Geophysical Research: Atmospheres*, 113(D17), 1-17.

Zimmerman, R. W., & King, M. S. (1986). The effect of the extent of freezing on seismic velocities in unconsolidated permafrost. *Geophysics*, 51(6), 1285-1290.

**Errata for
Seismic acquisition and analysis in a changing Arctic**

Helene Meling Stemland



Thesis for the degree philosophiae doctor (PhD)
at the University of Bergen

27.10.20 Helene Meling Stemland

(date and sign. of candidate)

Birthe Godal

(date and sign. of faculty)

Errata

- Page 5: Added commas before and after the names of the supervisors. “Thank you Tor Arne for (...)” – Corrected to “Thank you, Tor Arne, for (...)”. “Thank you Bent Ole for (...)” – Corrected to “Thank you, Bent Ole, for (...)”.
- Page 7: Replaced comma with “and”: “Due to this, seismic records from arctic environments often show dominating, highly dispersive surface waves” – Corrected to “Due to this, seismic records from arctic environments often show dominating and highly dispersive surface waves”
- Page 9: Changed case in paper title: from “arctic” to “Arctic” in the title of Paper 2.
- Page 14: Replaced “in” with “into”, and “future potential” with “potential future”: “(...) and finally a chapter that summarizes the main findings, puts them in a common context, and discusses some future potential research directions (Chapter 3).” – Corrected to “(...) and finally a chapter that summarizes the main findings, puts them into a common context, and discusses some potential future research directions (Chapter 3).”
- Page 19: Missing words: “(...) release of latent heat during phase change” – Corrected to “(...) release or uptake of latent heat during phase change”.
- Page 20: Replaced “reviews” with “overviews”: “see the reviews by Socco and Strobbia, 2004; Socco et al., 2010” – Corrected to “see the overviews by Socco and Strobbia, 2004; Socco et al., 2010”
- Page 21: Replaced “average” with “overall”: “Thus, the wave travels with velocities that depend on the average elastic properties of the composite, referred to as the **effective elastic properties**.” – Corrected to “Thus, the wave travels with velocities that depend on the overall elastic properties of the composite, referred to as the **effective elastic properties**.”
- After page 30: Add two blank pages (and update page numbers in the list of contents accordingly)
- Page 43: Changed case in paper title: from “arctic” to “Arctic” in the title of Paper 2.
- After page 108: Add two blank pages (and update page numbers in the list of contents accordingly)
- After page 126: Add two blank pages (and update page numbers in the list of contents accordingly)
- Page 144: Moved comma after equation 8 to appear right after the equation.
- Page 144: Moved comma after equation 9 to appear right after the equation.
- Page 144: Moved comma after equation 10 to appear right after the equation.
- Page 144: Moved comma after equation 11 to appear right after the equation.

Page 145: Moved comma after equation 14 to appear right after the equation.

Page 146: Moved comma after equation 15 to appear right after the equation.

Page 161: Replaced “conclusions” with “outcomes”: “The main conclusions from each paper can be summarized as follows:” – Corrected to “The main outcomes from each paper can be summarized as follows:”.

Page 163: Replaced “requires” with “deserves” and removed “further”: “Optimizing the balance between these two aspects requires further attention in future research.” – Corrected to “Optimizing the balance between these two aspects deserves attention in future research.”

Page 165: Replaced “quantifying” with “quantification of”: “(...) the natural next step involves quantifying how much (...)” – Corrected to “(...) the natural next step involves quantification of how much (...)”.

Throughout Chapter 1 and Chapter 3: Changed from lowercase to uppercase capital letter in the word “Arctic” to be consistent. (pages 7, 8, 11, 13, 14, 17-20, 26-29, 162-167).



Graphic design: Communication Division, UIB / Print: Skjipes Kommunikasjon AS



uib.no

ISBN: 9788230867419 (print)
9788230854631 (PDF)